Streamer Discharges

Citation for published version (APA):
Francisco, H. L. (Accepted/In press). *Streamer Discharges: steady propagation and interaction with trace gases*. [Phd Thesis 1 (Research TU/e / Graduation TU/e), Applied Physics and Science Education]. Eindhoven University of Technology.

Document status and date:
Accepted/In press: 21/06/2023

Document Version:
Publisher’s PDF, also known as Version of Record (includes final page, issue and volume numbers)

Please check the document version of this publication:

• A submitted manuscript is the version of the article upon submission and before peer-review. There can be important differences between the submitted version and the official published version of record. People interested in the research are advised to contact the author for the final version of the publication, or visit the DOI to the publisher's website.
• The final author version and the galley proof are versions of the publication after peer review.
• The final published version features the final layout of the paper including the volume, issue and page numbers.

Link to publication

General rights
Copyright and moral rights for the publications made accessible in the public portal are retained by the authors and/or other copyright owners and it is a condition of accessing publications that users recognise and abide by the legal requirements associated with these rights.

- Users may download and print one copy of any publication from the public portal for the purpose of private study or research.
- You may not further distribute the material or use it for any profit-making activity or commercial gain
- You may freely distribute the URL identifying the publication in the public portal.

If the publication is distributed under the terms of Article 25fa of the Dutch Copyright Act, indicated by the “Taverne” license above, please follow below link for the End User Agreement:

www.tue.nl/taverne

Take down policy
If you believe that this document breaches copyright please contact us at:

openaccess@tue.nl

providing details and we will investigate your claim.

Download date: 12. Jun. 2023

Technische Universiteit
Eindhoven
University of Technology

Department of Applied Physics and Science Education

Streamer Discharges

steady propagation and interaction with trace gases

Hani Louie Francisco

Streamer Discharges

steady propagation and interaction with trace gases

PROEFSCHRIFT

ter verkrijging van de graad van doctor aan de Technische Universiteit
Eindhoven, op gezag van de rector magnificus prof.dr. S.K. Lenaerts, voor
een commissie aangewezen door het College voor Promoties, in het
openbaar te verdedigen op woensdag 21 juni 2023 om 16.00 uur

door

Hani Louie Francisco

geboren te Cabanatuan, Filipijnen

Dit proefschrift is goedgekeurd door de promotoren en de samenstelling van de promotiecommissie is als volgt:

Voorzitter	prof.dr. C. Storm	
Promotor	prof.dr. U.M. Ebert	
Copromotoren	dr. B. Bagheri	
	dr. H.J. Teunissen	Centrum Wiskunde & Informatica
Leden	prof.dr. O. Scholten	Rijksuniversiteit Groningen
	dr.ir. S. Nijdam	
	prof.dr. C.M. Franck	Eidgenössische Technische Hochschule Zürich

Het onderzoek of ontwerp dat in dit proefschrift wordt beschreven is uitgevoerd in overeenstemming met de TU/e Gedragscode Wetenschapsbeoefening.

CWI
Centrum Wiskunde & Informatica

SAINT
Science and Innovation
With Thunderstorms
H2020 Marie Skłodowska-Curie Innovative Training Networks

The research in this thesis was funded by the European Union's Horizon 2020 research and innovation programme under the Marie Skłodowska-Curie grant agreement SAINT 72233.

Cover Design: Aaron Corpuz and Jojee Dumayaca; inspired by the cover of Pretty Guardian Sailor Moon, Vol. 5 (Naoko Takeuchi Collection).

Printing: Ipskamp Printing B.V.

A catalogue record is available from the Eindhoven University of Technology Library.

ISBN: 978-90-386-5769-1

Lightning and thunder require time; the light of the stars requires time; deeds, though done, still require time to be seen or heard.

Friedrich Nietzsche, *The Gay Science*
(trans. Walter Kaufmann)

Until I saw you in my thunderstorm, I didn't see you.

Carly Rae Jepsen, *Never Get to Hold You*

Contents

Part I

Introduction

Chapter 1

Streamer Discharges - Phenomena and Questions

In the first chapter of this thesis, we introduce what streamer discharges are, how they initiate and propagate, and where they are found in nature. We also mention some of their applications. The chapter ends with the research questions that we tackle and how the rest of the thesis is structured.

1.1 Electric discharges and streamer discharges

The phenomenon wherein electric charge flows through a non-conducting medium with an applied electric field is called an electric discharge. To allow charge flow, electric discharges need an ionization mechanism. There are many types of electric discharges, and the subject of this thesis is one: streamer discharges.

A streamer discharge, or more colloquially - a streamer, is a type of electric discharge that has a finger-like shape, ahead of which the electric field is enhanced and inside of which the electric field is screened. Figure 1.1 shows a streamer tip. The electric field enhancement in front of streamers provides a localized region where the electric field is above the breakdown value even when the background field is below breakdown, and thus it allows streamers to grow through electron-impact ionization. This area where the electric field is enhanced above breakdown is called the active zone.

The inside of a streamer, the streamer channel, is ionized with equal numbers of positive and negative charges - it is a conducting plasma region that is quasi-neutral. It is only in the layer surrounding the streamer that we observe a non-zero net charge, and we call that the charge layer. It is due to being surrounded by the charge layer that the electric field in the streamer interior is screened.

The charge layer at the streamer tip is curved due to the nonlinear dynamics of the space charge, electron drift, and ionization reactions. This curvature enhances the field ahead of it. There is a high impact ionization rate where the electric field is enhanced, and because of this, the streamer tip is at times also referred to as the ionization front.

Streamers are an example of low-temperature plasma - gases with low ionization degrees that occur at low gas temperatures [45]. In the case of streamers, the ionization degree is typically only between 10^{-6} to 10^{-5} in atmospheric air.

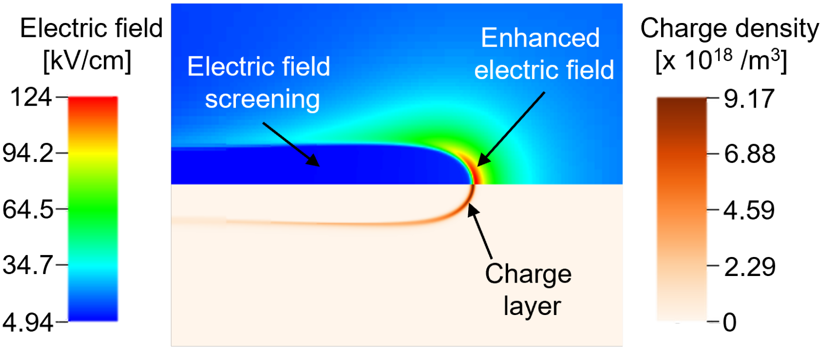

Figure 1.1: A streamer propagating to the right. The top panel presents an electric field plot while the bottom panel has a charge density plot.

1.2 Streamer initiation

Streamer initiation has long been investigated [85, 87, 97, 142], and the basic processes involved are well-known.

Given that an electron has enough energy, an electron colliding with a gas particle could result in the release of another electron in a process called electron-impact ionization. The threshold energy for ionization processes to occur varies per collision partner. For example, to ionize N_2 and O_2, an electron needs at least 15.58 eV [58] and 12.07 eV [59] respectively. One way electrons could gain such energies is by being subjected to an electric field above breakdown.

Suppose there are electrons in a region above electric breakdown, and in the same region, there are also particles that could be ionized. When electron-impact ionization occurs here, the electron that was released as a result also can gain the energy to cause another electron-impact reaction. We expect then a chain of electron-impact reactions that is collectively causing the liberation of more and more electrons. This phenomenon is called an electron avalanche.

With electrons and positive ions increasingly being created by the ionization reactions, a plasma region is created. At some point, the size of the electron avalanches gets big enough that there is significant charge separation between the electrons and the positive ions they have detached from.

The charged particles form a space charge layer, and this alters the background electric field, characteristic of streamer discharges. This happens in air when the number of electrons has reached about 10^8 to 10^9.

1.3 Streamer polarity and propagation

There are two types of streamer discharges based on the polarity of its space charge layer: positive streamers and negative streamers. A streamer is a positive streamer if the charge layer in its head is made up of positive charges, and it is negative if the charge layer is made up of negative charges. Following the polarity of its head, a streamer could then propagate along the same direction of the electric field (for positive streamers) or opposite to it (negative streamers).

Positive streamers additionally require the availability of electrons ahead of the streamer for their continued propagation. Streamer propagation happens much faster than ion drift, and thus, the positive ions that make up the charge layer of a positive streamer cannot, by themselves, advance the streamer head. Instead, electrons are needed to ionize the region the streamer is propagating to, effectively extending the streamer. In air, this happens through the photoionization of oxygen molecules [149]. Photoionization is the process wherein high energy photons ionize neutral molecules, causing them to release an electron.

The charge layer of negative streamers is dominated by electrons which by themselves flow opposite the direction of the electric field. Thus, the streamer does not require an additional electron source ahead of it. Negative streamers in air have been reported to require a higher voltage to initiate and often propagate slower than their positive counterparts [22, 76].

1.4 Streamers in nature and streamer applications

Electron avalanches for streamer inception need but one electron in a region above electric breakdown to start. In the atmosphere, electrons could come from energetic cosmic showers and be subjected to an electric field above breakdown at the tips of ice hydrometeors in thunderstorms [49, 111, 125].

There are multiple manifestations of streamers in the atmosphere. For one, they could come in the form of streamer coronas that precede lightning leaders in thunderclouds [121]. Leaders are another type of electric discharge, and they feature significant gas heating in their channels - unlike streamers where the energy goes mainly into electrons and molecular excitations, and little into general heating. Above thunderclouds, streamers exist in the form of sprites and the tips of blue jets [38, 109]. These atmospheric streamers are known to change the gas composition of the atmosphere, through, for example, the production of NOx and oxidants such as ozone, OH, and HO_2 [26, 89].

It is this capacity to induce plasma-chemical reactions without major energy loss through heating combined with the ability to deliver energized electrons at room temperature that makes it favorable to use streamers in a myriad of ways. We see streamers used in ozone generation [140], plasma medicine [42, 57, 145], plasma-assisted combustion [129], and cleaning technologies for gases, liquids, and surfaces [31, 47, 60]. Streamers are also used for flow control and propulsion [72, 86].

1.5 Research topics and structure of the thesis

This thesis looks at positive streamer discharges in air. We consider single streamers in homogeneous background electric fields with cylindrical geometry.

We start with parameter studies on positive streamers, which allowed us to observe how the streamer dynamics change with different background conditions and to identify different streamer behaviours. This analysis paved way to the development of approximations for relations between streamer properties. Finally, we look at how the different streamers we observed affect trace elements in their environment. In more detail, the thesis is structured as follows.

In chapter 3, we look at how varying the attachment rate below electric breakdown affects streamers. This modification mainly involves the streamer channel as that is where the attachment reactions dominate. The increase of attachment in this region means a reduction of the channel conductivity. This study gives us an insight into how streamers would behave in highly attaching gases, and what happens to streamers propagating on timescales longer than attachment times in air.

Chapter 4 discusses streamers in different background electric fields in air. From our efforts, we identified different regimes of streamer propagation behavior, and noted underlying patterns and relations. This is one of the first numerical studies to look at streamers in very low background electric fields.

A semi-analytical model for streamers that allows for the estimation of streamer properties from observational parameters is presented in chapter 5. Results from this reduced model for streamers are then compared with simulation results for verification.

In chapter 6, we look at how streamers in lightning processes contribute to the destruction of minor gas components in the atmosphere - specifically sulfur hexafluoride SF_6. We investigate which streamer-induced process contributes most to SF_6 destruction, what kind of streamer could destroy the most SF_6 molecules, and which altitude in the atmosphere is best for SF_6 destruction by streamers.

We conclude in chapter 7 where we give a summary of our main results and insights on what could be done to advance the research in the future.

By time of publication of this manuscript, chapters 3 and 4 of the thesis have been published, chapter 5 is available as an electronic publication ahead of publishing, and chapter 6 is close to submission.

Chapter 2

General Computational Set-up

We give details on the numerical model that we used for our simulations in this chapter. To simulate positive streamer discharges in air, we use a fluid model. Our domains have homogeneous background fields and are cylindrically symmetric. We only look at single streamers assuming cylindrical symmetry.

2.1 Fluid model

We simulate our streamers with a fluid model, which follows streamer development by describing the time evolution of the densities of electrons and other relevant species.

To be more specific, we use a drift-diffusion-reaction type fluid model with a local field approximation. This means that in our simulations we incorporate (1) drift, the movement of charged particles as a response to an applied electric field, (2) diffusion, the movement of charged particles from a region of higher concentration to a region of lower concentration, and (3) plasma-chemical reactions that may be consuming or producing charged particles. As our simulations are in air, we also include photoionization, which has an important nonlocal contribution.

The local field approximation assumes that the electrons are only influenced by the local electric field. This is a valid assumption for structures with spatial or temporal gradients occurring on larger spatial or temporal scales than the equilibriation length or time, which holds true for most parts of the streamer. We only observe high gradients in the streamer ionization front, but studies [69, 76, 91] have shown that foregoing the local field approximation in this region only leads to minor corrections if the fields are not too high [73].

2.2 Model equations

The electron density and ion densities are tracked using a continuity equation. For the electron density n_e, we have

$$\frac{\partial n_e}{\partial t} = \nabla \cdot (n_e \mu_e \mathbf{E} + D_e \nabla n_e) + S_i - S_\eta + S_{ph} + S_{ion}, \tag{2.1}$$

where μ_e is the electron mobility, $\mathbf{E}$ is the electric field, D_e is the diffusion coefficient, S_i is the ionization source term, S_η is the attachment source term, S_{ph} is the photoionization source term, and S_{ion} is the electron-ion-reactions source term. Electron-ion reactions include electron detachment and electron recombination.

The continuity equations for the other charged species, the ions, depend on which chemical reactions are included in the model. Generally, they take the form

$$\frac{\partial [Z_i]}{\partial t} = -s_i \nabla \cdot \left([Z_i] \, \mu_i \mathbf{E} \right) + S_{Z_i}, \tag{2.2}$$

where $[Z_i]$ is the density of ion Z_i, $s_i = \pm 1$ is the sign of the electric charge of species Z_i, μ_i is the ion mobility, and S_{Z_i} is the reaction source term.

Aside from the densities of species, we also need to follow the evolution of the electric field. We calculate the field with the electrostatic approximation, which assumes that the magnetic field in our system is not changing and allows us to neglect field coupling. Since we did not include any external magnetic fields in our simulations and simulated streamers create negligible magnetic fields [38, 97], this approximation is valid for our simulations.

With the electrostatic assumption, the only source of the electric field is the charge density ρ and the boundary conditions. The electric potential ϕ is acquired by solving the Poisson's equation for electrostatics

$$\nabla^2 \phi = -\rho / \epsilon_0 \tag{2.3}$$

where ϵ_0 is the permittivity in free space.

From the electric potential, the electric field $\mathbf{E}$ is computed as

$$\mathbf{E} = -\nabla \phi \tag{2.4}$$

2.3 Reaction source terms and reaction rates

The source term S_{Z_i} corresponds to the contribution of all reactions that affect the density of molecule Z_i, which could be neutral or charged. It is comprised of the reactions rates of all the reactions that involve Z_i. The reaction rates are calculated by multiplying the reaction rate coefficient with the densities of the reactants.

Reaction rate coefficients are found in literature [46, 65, 100] and are often a function of the electric field, electron energy, or gas temperature. For reactions that involve electrons as reactants, their reaction rate coefficients can be acquired by solving the Boltzmann equation, which will be discussed in the next section.

It is generally unnecessary to include all reactions that might occur, as only a handful might be dominating, and they might not all be known.

2.4 Cross sections, transport parameters, and electron reaction rate coefficients

Parameters such as electron mobility and the diffusion coefficient are called transport parameters as they quantify the transport behavior of a particle in a certain medium. To get transport parameters, the electron velocity distribution function and energy distribution function are needed. One way to do this is by solving the electron Boltzmann equation [43], a kinetic equation that describes the evolution of the electron distribution function. We use Bolsig+ [54], a two-term approximation Boltzmann equation solver for electrons in weakly ionized gases, to solve the Boltzmann equation for our purposes. Bolsig+ was chosen as it is fast, robust, and commonly-used. As input for Bolsig+, we need to define the gas in our domain and provide the necessary cross sections.

Cross sections give the probability that a certain collision or reaction will occur. They are dependent on the relative velocity between the colliding particles involved in the reaction. They can be acquired experimentally [64, 95], and in certain cases, they can be approximated analytically [7, 23, 112, 150], although often this is not possible. We get our cross section data from LXCat, mostly from the Phelps database [1], which is widely used.

Aside from transport parameters, Bolsig+ also give us the reaction rate coefficients for reactions that involve electrons if we supply the cross sections for these reactions as well. However, not all reactions have available cross sections because of difficulties in measurements.

In solving the Boltzmann equation using Bolsig+, one is asked to provide an assumption on how the electron density is expected to grow if the collision processes do not conserve the total number of electrons - whether there would be a temporally-dependent growth or a spatially-dependent one. Exponential temporal growth of the electron density without space dependence gives us coefficients similar to what would be measured in pulsed Townsend experiments while exponential spatial growth without temporal dependence corresponds to quantities from steady state Townsend experiments [134]. The temporal growth model is more commonly used but the spatial growth model is suggested to be more realistic in most cases by [54]. In [147], it was reported that the temporal growth model leads to better agreement between fluid models and particle models for the simulation of streamer discharges. Particle models simulate plasma discharges by following the position and velocities of particles over time instead of the particle densities as in fluid models.

The gas we looked at in our investigations is dry synthetic air, which is 80% nitrogen and 20% oxygen. The gas temperature is assumed to be constant at 300 K.

2.5 Photoionization

The photoionization source term S_{ph} is calculated using

$$S_{ph}(\mathbf{r}) = \int d^3r' \, \frac{I(\mathbf{r}')f(|\mathbf{r}-\mathbf{r}'|)}{4\pi|\mathbf{r}-\mathbf{r}'|^2} \tag{2.5}$$

where $I\left(\mathbf{r}\right)$ is the source of ionizing photons, $f(r)$ is the absorption function, and $4\pi|\mathbf{r}-\mathbf{r}'|^2$ is a geometric factor. Using Zheleznyak's model [149], we compute the photon source term $I\left(\mathbf{r}\right)$ with

$$I\left(\mathbf{r}\right) = \frac{p_q}{p+p_q}\xi S_i\left(\mathbf{r}\right) \tag{2.6}$$

where p is the actual gas pressure, p_q is a gas-specific quenching pressure, and ξ is a proportionality factor. We set the proportionality factor $\xi = 0.075$ and employ a quenching pressure $p_q = 40$ mbar.

The absorption function $f(r)$ is given by

$$f(r) = \frac{\exp(-\chi_{\min}p_{O_2}r) - \exp(-\chi_{\max}p_{O_2}r)}{r\ln(\chi_{\max}/\chi_{\min})} \tag{2.7}$$

where $\chi_{\max} \approx 1.5 \times 10^2/(\text{mm bar})$, $\chi_{\min} \approx 2.6/(\text{mm bar})$, and p_{O_2} is the partial pressure of oxygen. It is an effective funtion for photon absorption in the 98 to 105 nm wavelength range [149].

A set of Helmholtz differential equations [19, 84] with Bourdon's three-term parameters [19] were utilized to solve the photoionization integral.

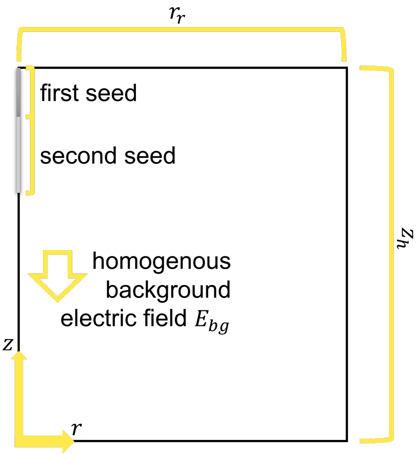

Figure 2.1: The computational domain.

2.6 Computational domain and boundary conditions

Our streamer simulations were done in a cylindrically symmetric domain, a design apt for the study of single streamers. We illustrate the domain in figure 2.1. In such a set-up, we have the r-axis as the horizontal axis and the z-axis as the vertical axis. The simulation was configured to have a streamer propagating along $r = 0$ from the upper boundary to $z = 0$.

We study positive streamers, and since these streamers propagate along the electric field direction, we need to have an electric field pointed in the $-z$ direction to get positive streamers that propagate downwards. We fixed the potential at $z = z_h$ to be equal to $E_{bg} \cdot z_h$, where E_{bg} is our desired background field and z_h is the height of our domain. At $z = 0$, the potential is fixed at zero. Such boundary conditions, where we fix the value of a quantity at the boundary, are called Dirichlet boundary conditions.

Neumann zero boundary conditions, where we assign the normal derivative of a quantity at the boundary to zero, were used for the electron density and electric potential on the rest of boundaries. We use this condition for the electron density at $z = 0, z_h$ and $r = 0, r_r$, where r_r is the radius of the domain. We use the same boundary condition also for the electric potential at $r = 0, r_r$. This allows charged particle flow out of the domain, but the effect of this is negligible as the simulations stop before the streamers connect the two boundaries [136].

2.7 Initial conditions

Streamer inception requires an electric field above electric breakdown. However, studying a variety of streamers requires investigating them in a wide range of background fields, including fields below breakdown. To be able to initiate streamers in these background fields, we placed a neutral seed at the top of our domain. The seed is a local ionized region which acts like a needle electrode and dynamically starts field enhancement at its tip. With the appropriate applied electric field and seed size and density, the field enhancement locally enhances the electric field above breakdown.

A thinner and less dense neutral cylindrical seed is placed directly below the first seed to provide the initial electrons to start the electron avalanches.

The inclusion of these two seeds is often enough to initiate a streamer in fields below breakdown. However, for about less than half the breakdown value and below, streamers become harder and harder to initiate, and on top of that, it becomes more difficult to avoid streamer branching [40, 75]. Streamer branching breaks cylindrical symmetry and is thus not valid for our cylindrically symmetric simulations [80]. Our streamer initiation techniques for the low background field cases will be discussed in the specific chapters that involve them.

2.8 Implementation

The streamer simulations were run using the code Afivo-streamer, an open-source plasma fluid code for simulations of streamer discharges [136, 137]. It uses adaptive mesh refinement with criteria based on the electric field and OpenMP parrallelism. For solving Poisson's equation, multrigid methods are used, specifically a full multigrid cycle for the initial electric potential, and then a number of V-cycles for the subsequent updates.

Part II

Streamer Modeling and Analysis

Chapter 3

Electrically-isolated propagating streamer heads formed by strong electron attachment

Streamer discharges occur in the early stages of electric breakdown of gases in lightning, as well as in plasma and high voltage technology. They are growing filaments characterized by a curved charge layer at their tip that enhances the electric field ahead of them. In this study, we analyze the effect of strong electron attachment on the propagation of positive streamers. Strong attachment occurs in insulating gases like SF_6 or in air at increased density. We use the classical fluid approximation with photo-ionization for streamers in ambient air, and we artificially increase the electron attachment rate where the field is below the breakdown value. This modification approximates air pressures above 1 bar at room temperature. We find that the streamer head can keep propagating even though the ionized channel loses its conductivity closely behind the head; hence, even if it is electrically isolated. We describe how, depending on the attachment rate, the streamer propagation in a constant electric field can be accelerating, uniformly translating, or stagnating.

This chapter is published as:
Hani Francisco, Behnaz Bagheri, and Ute Ebert. Electrically isolated propagating streamer heads formed by strong electron attachment. *Plasma Sources Science and Technology*, 30(2):025006, February 2021

In this paper, we found that positive streamers can keep propagating after they lost conductivity in the back part of the channel - when they are electrically detached from the electrode. We also found that they can accelerate, decelerate, or propagate uniformly, depending on the attachment rate in a given background electric field. Within a propagation length of 40 mm, the uniform or steady propagation appears to be stable, while in general one would expect the streamers to accelerate or decelerate eventually if conditions for steady propagation are not perfectly met. This was stated in later papers [51, 75].

3.1 Introduction

Streamers [97, 143, 148] are fast-growing ionized filaments whose development is governed by the creation of a curved space charge layer around them and the self-enhancement of the electric field ahead of them. Streamers can be formed in gases [96] and in liquids [8] when the electric field locally exceeds the breakdown threshold even though the background electric field is below breakdown.

In nature, streamers occur as precursors of sparks and lightning leaders, and they are visible as sprites above thunderclouds. In plasma technology, streamers are used in various applications [2, 18, 24, 25, 41], for example, in plasma medicine [42, 48, 70], plasma-assisted combustion [115, 128], surface treatment, and thin film deposition [17].

Streamers occur with positive or negative polarity. Positive streamers have a positive net charge (i.e. positive space charge) at their tips, and they propagate in the same direction as the background electric field, which is against the direction of the electron drift. Negative streamers have a negative net charge (i.e. negative space charge) at their tips, and they propagate along the direction opposite of the background electric field - in the direction of the electron drift. In this paper, we focus on positive streamers, which form more easily than negative ones in air [22]. Since positive streamers propagate opposite the direction of the electron drift, they require a source of free electrons at their heads for propagation. In air, photoionization is the most important source of these electrons [96, 101].

As electrons enter the region where the electric field is above the breakdown value, referred to as the ionization zone, they multiply due to the electron-impact ionization reactions dominant in this region. However, in the interior region of the streamer where the electric field is below breakdown, electrons are lost due to attachment to electronegative molecules.

Attachment reactions are prevalent, in particular, in gases such as sulfur hexafluoride (SF_6), which are used in high voltage equipment such as circuit breakers [27, 30]. In air, the attachment processes involve dissociative and three-body reactions with oxygen molecules. Like impact ionization and many other rates in streamers, the dissociative attachment reaction rate increases linearly with the gas density. However, the three-body attachment reaction rate increases quadratically with gas density, and thus, its importance increases when the density increases.

In this paper, our goal is to understand the effect of the electron attachment rate on the dynamics of positive streamers. In particular, we look at whether streamers can continue to propagate if the electrons in the channel get rapidly attached. To investigate this, we perform axisymmetric simulations of positive streamers in air at standard temperature and pressure with the normal and modified attachment rates. In the latter cases, we systematically enhance the attachment rate in regions where the electric field is below the breakdown value, and we keep it unchanged in the high-field regions. This way, we focus only on the effect of the attachment rate on the streamer dynamics while we keep other parameters such as gas composition, impact ionization rate, and photoionization fixed. The details of this modification are given in section 3.2.2.

The structure of the paper is as follows. The discharge model and simulation conditions are presented in section 3.2, where the model equations along with the transport parameters and reaction rates are described in section 3.2.1, the computational domain and boundary conditions in section 3.2.3, and the initial conditions are given in section 3.2.4. The results are presented in section 3.3, where in section 3.3.1, we show that a streamer can keep propagating while the streamer head is electrically isolated from streamer body and electrode due to significant electron attachment behind the streamer head. In section 3.3.2, we discuss three modes of streamer propagation: accelerating, uniformly translating, and stagnating. Finally, in the concluding section 3.4, we summarize our results in section 3.4.1, and we relate our results on electrically-isolated propagating streamer heads to concepts by other authors in section 3.4.2.

3.2 Discharge model

3.2.1 Model equations, transport parameters, and reaction rates

We used a drift-diffusion-reaction type fluid model to simulate positive streamers in artificial air, composed of 80% nitrogen and 20% oxygen, at standard temperature and pressure. Twelve reactions, listed in table 3.1, were considered: electron impact ionization (k_1, k_2), electron attachment (k_3, k_4), electron detachment (k_5, k_6), ion conversion ($k_7 - k_{11}$),

Reaction No.	Reaction	Reaction rate coefficient	Reference
1	$e + \mathrm{N_2} \rightarrow 2e + \mathrm{N_2^+}$	$k_1\,(E/N)$	[1]
2	$e + \mathrm{O_2} \rightarrow 2e + \mathrm{O_2^+}$	$k_2\,(E/N)$	[1]
3	$e + \mathrm{O_2} + \mathrm{O_2} \rightarrow \mathrm{O_2^-} + \mathrm{O_2}$	$k_3\,(E/N)$	[1]
4	$e + \mathrm{O_2} \rightarrow \mathrm{O} + \mathrm{O^-}$	$k_4\,(E/N)$	[1]
5	$\mathrm{M} + \mathrm{O_2^-} \rightarrow e + \mathrm{O_2} + \mathrm{M}$	$k_5\,(E/N) = 1.24 \times 10^{-17} \exp\left(-\left(\frac{179}{8.8+E/N}\right)^2\right)\ \mathrm{m^3\ s^{-1}}$	[107]
6	$\mathrm{N_2} + \mathrm{O^-} \rightarrow e + \mathrm{N_2O}$	$k_6\,(E/N) = 1.16 \times 10^{-18} \exp\left(-\left(\frac{48.9}{11+E/N}\right)^2\right)\ \mathrm{m^3\ s^{-1}}$	[107]
7	$\mathrm{O_2} + \mathrm{O^-} \rightarrow \mathrm{O_2^-} + \mathrm{O}$	$k_7\,(E/N) = 6.96 \times 10^{-17} \exp\left(-\left(\frac{198}{5.6+E/N}\right)^2\right)\ \mathrm{m^3\ s^{-1}}$	[107]
8	$\mathrm{O_2} + \mathrm{O^-} + \mathrm{M} \rightarrow \mathrm{O_3^-} + \mathrm{M}$	$k_8\,(E/N) = 1.1 \times 10^{-42} \exp\left(-\left(\frac{E/N}{65}\right)^2\right)\ \mathrm{m^6\ s^{-1}}$	[107]
9	$\mathrm{N_2^+} + \mathrm{N_2} + \mathrm{M} \rightarrow \mathrm{N_4^+} + \mathrm{M}$	$k_9 = 5.0 \times 10^{-41}\ \mathrm{m^6\ s^{-1}}$	[4]
10	$\mathrm{N_4^+} + \mathrm{O_2} \rightarrow 2\mathrm{N_2} + \mathrm{O_2^+}$	$k_{10} = 2.5 \times 10^{-16}\ \mathrm{m^3\ s^{-1}}$	[4]
11	$\mathrm{O_2^+} + \mathrm{O_2} + \mathrm{M} \rightarrow \mathrm{O_4^+} + \mathrm{M}$	$k_{11} = 2.4 \times 10^{-42}\ \mathrm{m^6\ s^{-1}}$	[4]
12	$e + \mathrm{O_4^+} \rightarrow 2\mathrm{O_2}$	$k_{12}\,(E/N) = 1.4 \times 10^{-12}(300\ \mathrm{K}/T_e)^{1/2}\ \mathrm{m^3\ s^{-1}}$	[65]

Table 3.1: Reactions included in the model with reaction rate coefficients and references. M is any molecule, either $\mathrm{O_2}$ or $\mathrm{N_2}$. T_e in reaction number 12 depends on E/N through the mean electron energy $\langle \epsilon_e \rangle$ as $T_e = 2\langle \epsilon_e \rangle / 3k_B$ [65], and $\langle \epsilon_e \rangle$ is calculated with Bolsig+.

and electron-ion recombination (k_{12}). The temporal evolution of the electron density (n_e) is given by the continuity equation

$$\frac{\partial n_e}{\partial t} = \nabla \cdot (n_e \mu_e \mathbf{E} + D_e \nabla n_e) + S_i - S_\eta + S_{ph} + S_{ion}, \tag{3.1}$$

where $\mathbf{E}$ is the electric field, μ_e is the electron mobility, D_e is the electron diffusion coefficient, S_i is the electron impact ionization source term, S_η is the electron attachment source term, S_{ph} is the non-local photoionization source term, and S_{ion} contains all electron detachment reactions from the ions minus the electron-ion recombination reaction.

The impact ionization source term S_i, the electron attachment source term S_η, and the photoionization source term S_{ph} contain reactions of electrons with neutral molecules. These are the relevant plasma-chemical reactions in the ionization zone ahead of the streamer. They are calculated using the rate coefficients given in table 3.1:

$$S_i = k_1 n_e \left[\mathrm{N_2}\right] + k_2 n_e \left[\mathrm{O_2}\right], \tag{3.2}$$

$$S_\eta = k_3 n_e \left[\mathrm{O_2}\right]^2 + k_4 n_e \left[\mathrm{O_2}\right]. \tag{3.3}$$

Note that we do not include the three-body attachment reaction, $e + O_2 + N_2 \rightarrow O_2^- + N_2$, in our model because its reactions rates are about three orders of magnitude smaller than k_3 [65].

S_i and S_η are linear in the electron density n_e. As the degree of ionization at standard pressure and temperature and below is small within a streamer, the densities of neutral molecules $[O_2]$ and $[N_2]$ can be assumed to be constant. Therefore the impact ionization and attachment reactions can be written as the product of the electron flux $\mu_e E n_e$ and the coefficients α and η respectively [97]. The effective ionization source term can then be defined as

$$S_i - S_\eta = \big(\alpha - \eta\big)\ \mu_e E\ n_e, \quad \alpha_{\text{eff}} = \alpha - \eta. \tag{3.4}$$

The sign of α_{eff} determines whether the local electron density increases or decreases in the streamer ionization front.

The photoionization source term S_{ph} contributes only a small correction to the local reaction rates. However, it is very important due to its nonlocal nature, which allows for the liberation of electrons in the non-ionized region. It is given by

$$S_{ph}(\mathbf{r}) = \int d^3r'\ \frac{I(\mathbf{r}')f(|\mathbf{r} - \mathbf{r}'|)}{4\pi|\mathbf{r} - \mathbf{r}'|^2} \tag{3.5}$$

where $I(\mathbf{r})$ is the source of ionizing photons, $f(r)$ is the absorption function, and $4\pi|\mathbf{r} - \mathbf{r}'|^2$ is a geometric factor. We employed the commonly used Zheleznyak's model [149], where $I(\mathbf{r})$ is proportional to the electron impact ionization source term (S_i)

$$I(\mathbf{r}) = \frac{p_q}{p + p_q}\xi S_i(\mathbf{r}). \tag{3.6}$$

Here p is the actual gas pressure, $p_q = 40$ mbar is a gas-specific quenching pressure, and ξ is a proportionality factor that was set to $\xi = 0.075$. We approximated the integral in equation (3.5) using a set of Helmholtz differential equations [19, 84] with Bourdon's three-term parameters [19]. In addition to the original papers [19, 84], the reader is also referred to the appendix of [16] for more details.

In the ionized region inside the streamer, reactions involving ions are also significant. The relevant terms affecting the electron density are

$$S_{ion} = k_5 [\text{M}] \left[O_2^-\right] + k_6 [N_2] \left[O^-\right] - k_{12} n_e \left[O_4^+\right], \tag{3.7}$$

where [M] is the density of all neutral molecules: $[M] = [N_2] + [O_2]$.

Other species Z_i in our model are ionized or non-ionized molecules or atoms. According to table 3.1, these are N_2^+, N_4^+, O_2^+, O_4^+, O^-, O_2^-, O_3^-, and the neutrals O and N_2O. Their densities are also calculated from a continuity equation

$$\frac{\partial [Z_i]}{\partial t} = -s_i \nabla \cdot ([Z_i] \mu_i \mathbf{E}) + S_{Z_i}, \tag{3.8}$$

where $s_i = \pm 1$ is the sign of the electric charge of species i and μ_i is the ion mobility. The neutral species are treated as immobile. The drift of ions is neglected in most of the paper as their mobility is much smaller than that of electrons, but in section 3.3.5, we include the ion drift and discuss its effect on the previous results. All ion mobilities are assumed to be 2.2 $\times 10^{-4}$ m^2/V s [138] in that set of simulations. As O_3^-, O, and N_2O do not drive further reactions in our model, their densities do not need to be calculated in practice, except to account for the contribution of the O_3^- ion to the space charge density.

The electric potential and the electric field are calculated as

$$\nabla^2 \phi = -\frac{\rho}{\epsilon_0}, \quad \mathbf{E} = -\nabla \phi, \tag{3.9}$$

where ϵ_0 is the vacuum permittivity, $\rho = e(n_i - n_e)$ is the space charge density, e is the elementary charge, and n_i is the density of all positive ions minus the density of all negative ions.

Most reaction rate coefficients in table 3.1 are a function of the reduced electric field E/N. Electron-neutral scattering cross sections for nitrogen and oxygen are taken from the Phelps database [1]. Bolsig+ [54] (version 03/2016 for Linux), an electron Boltzmann equation solver, was used to calculate the mean electron energy, transport coefficients μ_e and D_e, and the reaction rates for electron impact ionization and electron attachment (i.e. k_1, k_2, k_3, and k_4). Bolsig+ solved the Boltzmann equation the spatial growth model.

3.2.2 Modification of effective ionization coefficient

To identify the effect of strong attachment in regions below the breakdown field, the effective ionization coefficient was modified in such a way that the attachment rate in high electric field regions is unchanged and it is only enhanced in regions below the electric breakdown value. The photoionization rate is made unaffected by the changes in the coefficients.

This is accomplished in two steps. First, the effective ionization coefficient was multiplied by a factor m below the electric breakdown field E_c, which is about 28 kV/cm in our case.

$$\alpha_m(E) = \begin{cases} \alpha_{\text{eff}}\left(|\mathbf{E}|\right) & \text{when } |\mathbf{E}| \geq E_c, \\ m \cdot \alpha_{\text{eff}}\left(|\mathbf{E}|\right) & \text{when } |\mathbf{E}| < E_c, \end{cases} \tag{3.10}$$

This translates to multiplying reaction rate coefficients k_1, k_2, k_3, and k_4 with the factor m when used in regions below the breakdown field. Above the breakdown field, the effective ionization coefficient is unchanged. Figure 3.1 shows the reduced effective ionization coefficient α_m/N as a function of the reduced electric field strength E/N for different values of m. These so-called reduced quantities are scaled with the gas density N. The reduced effective ionization coefficient for air at 26 bar is included for comparison, and we see that its values match the $m = 26$ case for reduced electric fields below 30 Td, where three body attachment is dominating. As we describe later in section 3.3, the reduced electric fields inside streamer channels are found to be below 30 Td. Furthermore, the attachment rate in the $m = 37$ case, which has the highest attachment rate in this study, is still about one order of magnitude smaller than the respective rate in SF_6 at standard temperature and pressure [1].

Second, the photoionization source term (3.6) was set to continue to use the unmodified ionization coefficient α.

3.2.3 Computational domain, electric field, and boundary conditions

The model is implemented in afivo-streamer [136, 137], which employs geometric multigrid techniques to solve Poisson's equation and OpenMP parallelism. We simulate cylindrically symmetric positive streamers in a volume spanned by radius r and axis z. The domain has a length of 50 mm and a radius of 50 mm. Adaptive mesh refinement is employed with the grid set to have a minimum size of 2 μm. The refinement and derefinement criteria are based on the local electric field value as in [136] with an additional

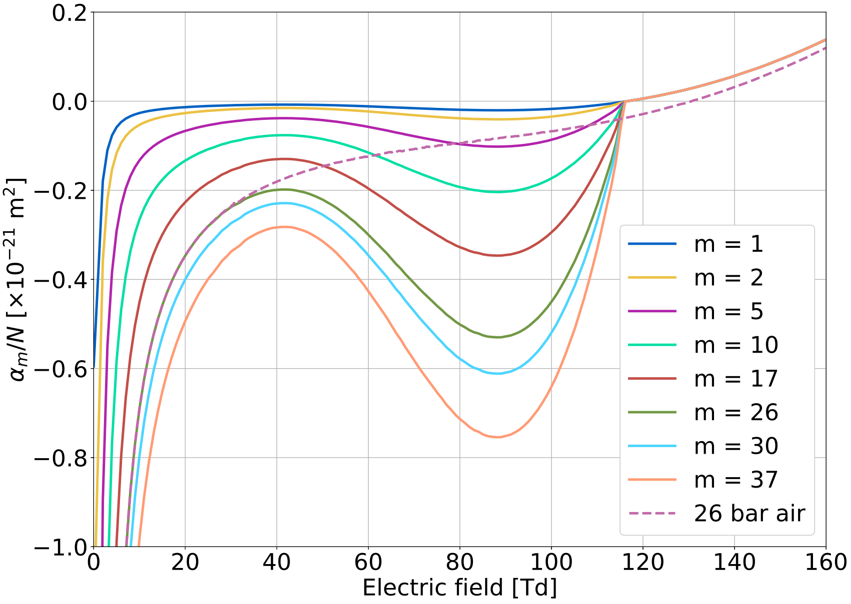

Figure 3.1: Reduced effective ionization coefficients α_m/N from equation (3.10) as a function of the reduced electric field E/N for the indicated values of m and the reduced effective ionization coefficient for air at 26 bar.

criterion based on the charge density: refine if $\alpha(1.2 \times E)\Delta x > 0.5$ and derefine if $\frac{\alpha(1.2\times E)}{1.2}\Delta x < 6.25 \times 10^{-2}$ and $|\frac{\epsilon_0 \cdot 4.5\times 10^{10}}{\rho}| > 0.5$, where $\alpha(E)$ is the field-dependent ionization coefficient, E is the electric field strength, and Δx is the grid spacing. We apply a homogeneous background electric field by fixing the electric potential at $z = 0$ mm and $z = 50$ mm. Neumann zero boundary conditions are applied to the electric potential at $r = 0$ mm and $r = 50$ mm, and to the electron density at all boundaries. The electric field points in $-\hat{z}$ direction with a magnitude of 15 kV/cm, which is about half of the breakdown field. No background ionization is incorporated in the domain.

3.2.4 Initial conditions

To initiate a positive streamer, we placed two neutrally charged cylindrical seeds on the axis of symmetry. The first seed serves as the initiation point of the streamer. It is 1 mm long with $2.25 \times 10^{20}/\mathrm{m}^3$ electrons and positive ions and has a width of 0.25 mm. It extends from $z = 50$ mm to 49 mm. The second seed supplies additional electrons during initiation until photoionization provides sufficient electrons for continued streamer propagation. This seed is 2 mm long with $1.0 \times 10^{17}/\mathrm{m}^3$ electrons and positive ions and has a width of 0.2 mm. It extends from $z = 49$ mm to 47 mm. The seeds decay with a Gaussian profile along the r-axis throughout their length and radially decay with a Gaussian profile in all directions at the caps.

For air, which is the case of $m = 1$ in equation (3.10), a streamer initiates in such setup. However, for strongly enhanced attachment conditions with large values of m, a streamer does not successfully initiate. Therefore, we first ran our simulation with the normal attachment rate $m = 1$ for 20 ns to get a streamer and then take this stage, that is illustrated in figure 3.2, as the initial condition for all runs with values of m from 1 up to 37. At this stage, a streamer has clearly formed and grown to a length of about 3.53 mm and a radius of 153 μm.

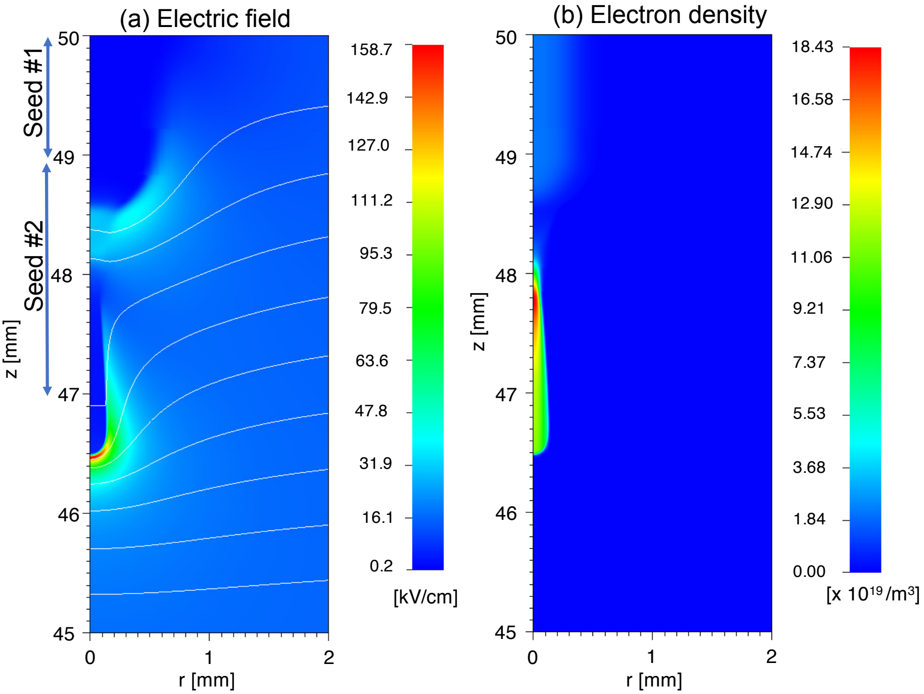

Figure 3.2: The initial condition at $t = 0$ ns for all streamer simulations presented in this paper, in radial coordinates (r, z): (a) electric field strength $|\mathbf{E}|$ (color-coded) with white equipotential lines, (b) electron number density. The streamer has initiated from the seeds at time $t = -20$ ns, and it has propagated to a length of about 3.53 mm at time $t = 0$ ns with $m = 1$. Note that the computation domain extends from 0 to 50 mm both in r and in z directions; however, in this figure only a part of the domain is shown.

3.3 Streamer evolution for different values of m

3.3.1 Two examples: $m = 1$ and $m = 26$

Figures 3.3 and 3.4 show the evolution of the streamer with $m = 1$ on the left-hand side and the streamer with $m = 26$ on the right-hand side. For $m = 26$, electron attachment is strongly enhanced when the electric field is below the breakdown value, while it is the same as in air when the field is above breakdown. The background field is 15 kV/cm, which is about half of the breakdown field. The evolution of the $m = 1$ streamer is shown in time steps of 15 ns, and the evolution of the $m = 26$ streamer is shown in time steps of 30 ns. The $m = 1$ streamer propagates over a length of 30.4 mm within 45 ns, and the $m = 26$ streamer propagates over a length of 22.8 mm within 90 ns.

The panels in figures 3.3 and 3.4 show the electron number density n_e, the number density of all negative ions $[\mathrm{O}^-]+[\mathrm{O}_2^-]+[\mathrm{O}_3^-]$, the space charge density ρ/e, and the electric field strength $E = |\mathbf{E}|$ with white equipotential lines ϕ. Within each row, the same color coding is used for the respective densities and the field strength. The figures zoom into the region $r \leq$3 mm and 15 mm $\leq z \leq$ 50 mm. The overall simulation volume extends to 50 mm in the r direction and 50 mm in the z direction.

$m = 1$

The streamer with the normal attachment rate, shown on the left-hand side of figures 3.3 and 3.4, presents the familiar phenomenology: it forms an elongated ionized channel that largely suppresses the electric field in the channel interior and enhances it ahead of the streamer tip. The electric conductivity of the streamer body is due to the density n_e of free electrons that drift in the local electric field. At the edge of the ionized region, the electric field changes strongly across the thin space charge layer; it is formed by the surplus or lack of free electrons relative to the density of positive ions. Within the strong external electric field of more than half of the breakdown value, the streamer radius grows in time and so does its velocity. Because the streamer head gets wider, more positive electric charge is required at its head. As charge is conserved, the negative charge moves backward, as can be seen in both the equipotential lines and the space charge density ρ/e.

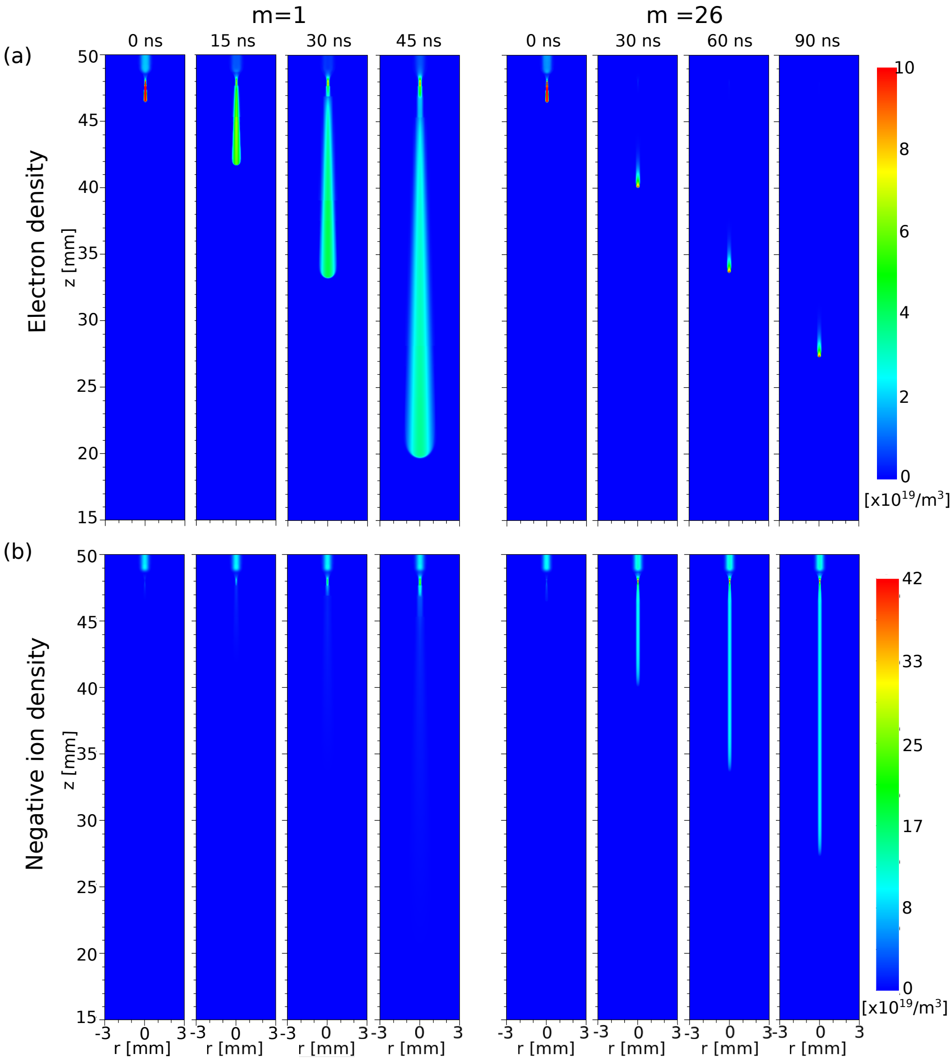

Figure 3.3: Streamer evolution in air with different electron attachment rates: normal attachment ($m = 1$) at times 0, 15, 30, and 45 ns on the left, and strong attachment rates ($m = 26$) at times 0, 30, 60, and 90 ns on the right. The background electric field is 15 kV/cm. Shown are the electron density and the number density of negative ions (i.e. $[O^-] + [O_2^-] + [O_3^-]$). Figure 3.4 contains the space charge densities and the electric fields for the same cases.

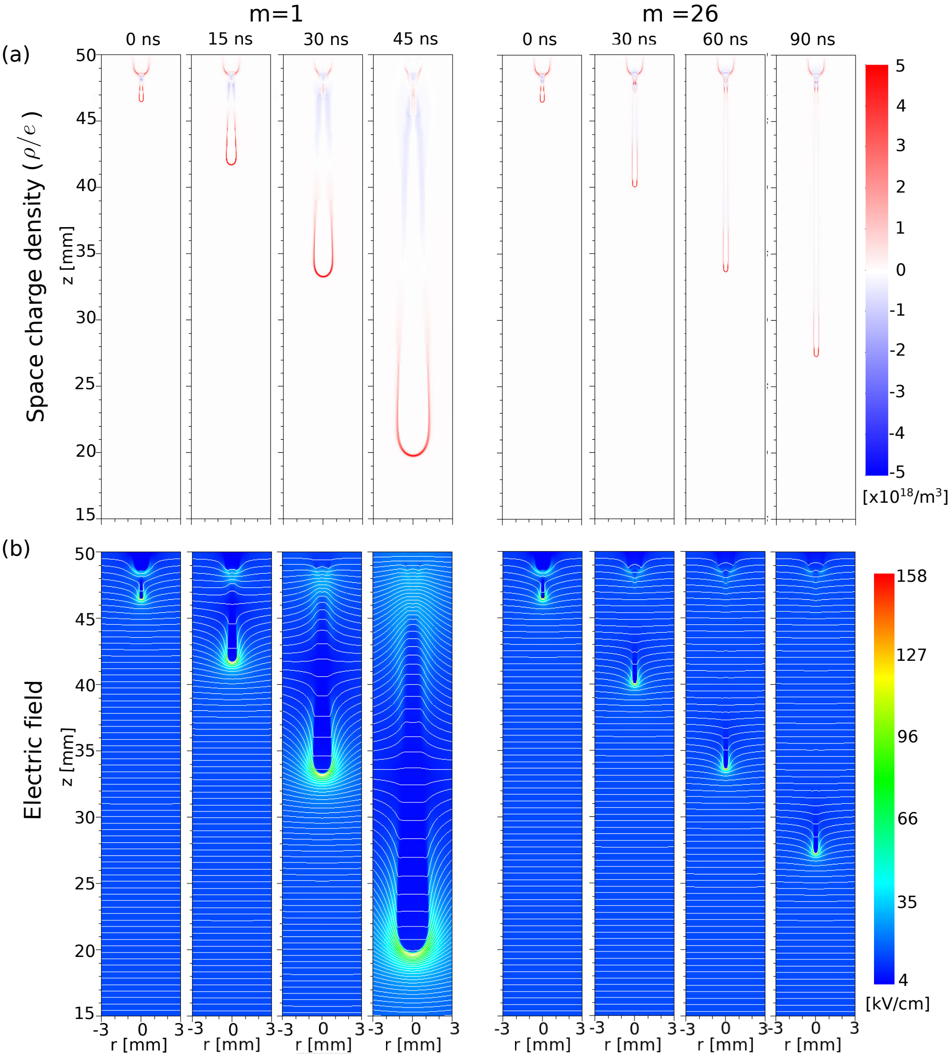

Figure 3.4: The same simulations as shown in figure 3.3, but here the space charge density ρ/e is plotted in the upper row with the electric field (color-coded) with equipotential lines (white) in the lower row.

No considerable density of negative ions is formed in the streamer interior.

$m = 26$

The streamer with strongly enhanced attachment rate, shown on the right hand-side of figures 3.3 and 3.4, has a very different behaviour even though the external field is the same and the plasma reactions are only changed in the region below the breakdown field. The streamer head propagates with a small and nearly constant radius and velocity. The density n_e of free electrons that is created in the ionization front rapidly disappears behind the streamer head due to fast attachment, and it leaves a density of negative ions behind. A thin layer of positive charge surrounds the streamer head, but as the streamer propagates, only a faint negative charge appears at its back end, and that does not change the electric field in a significant manner. The streamer tip rather propagates in a solitary manner, and the electric field behind it returns to the background value, as can be read particularly clearly from the straight and parallel equipotential lines at some distance behind the streamer head.

Surprisingly, this electrically-isolated streamer head keeps propagating essentially without changing its shape and without destabilizing. Thus, it behaves as a coherent structure, i.e. as a nonlinearly stabilized structure like a soliton.

3.3.2 Temporal evolution of maximum field, velocity, and radius

In figure 3.5, the maximum electric field $E_{\max}$, streamer velocity v, and streamer radius R for different values of m are plotted as a function of streamer length L. The plot finishes at a length of 40 mm, while the electrode is at $z = 50$ mm. Hence, effects of electrode proximity are not shown. The streamer length is defined as 50 mm$-z_{max}$, where $z_{\max}$ is the location of the maximum electric field. As earlier in [16], the radius is measured as the location where the radial component E_r of the electric field is maximum.

Three different cases of streamer growth can be distinguished in figure 3.5:

- *Accelerating streamers.* For the case of artificial air ($m = 1$) as shown in figures 3.3 and 3.4, the streamer radius R increases with streamer length L from 0.146 to 1.00 mm and the streamer velocity v from 2.20×10^5 m/s to 1.12×10^6 m/s, while the maximum electric field $E_{\max}$ at the streamer head decreases slightly from 158 kV/cm to 116 kV/cm. The same tendency of increasing velocity and radius and decreasing maximum field as a function of streamer length is seen for all values of the attachment parameter m up to 26, though the rates of increase or decrease diminish with growing m.
- *Uniformly translating streamers.* The case of $m = 26$, that is also displayed in figures 3.3 and 3.4, is a limiting case: radius, velocity, and the maximum field stay approximately constant while the streamer propagates. It is remarkable that this streamer head is dynamically stable, and that the motion is really a uniform translation where the background field is restored after the streamer head has passed and the nonconducting state is re-established.
- *Decelerating and stagnating streamers.* For $m > 26$, streamer radius and velocity decrease with growing streamer length while the maximum electric field at the streamer tip grows very rapidly. In fact, the simulation stops, because the increasing electric field requires a too small numerical time step to proceed. Due to the CFL condition [137], the numerical time step has gone down to less than 10^{-14} s from 10^{-12} s with the maximum electric field suddenly reaching to values greater than 300 kV/cm in a limited region ahead of the streamer. From an investigation on negative streamers in [73], the local field approximation was found to no longer be valid at electric field values above 200 kV/cm at 1 bar, and this limit is greatly exceeded by our stagnating streamers before the simulations stop.

The way how the positive streamers with $m > 26$ decelerate, and eventually stop, is reminiscent of earlier observations of stagnating and “dying” positive streamers [106, 135].

3.3.3 The front structure of streamers at 30 mm length

Streamers of 30 mm length for different values of m are now analyzed in more detail; more precisely, we look at streamers that have propagated from $z = 46.5$ mm up to $z = 20$ mm. This occurs after a time of 44.75 ns for $m = 1$, after 87.25 ns for $m = 17$, and after 125 ns for $m = 26$. The cases of $m = 30$ and 37 are excluded, as these streamers do not reach this length.

Figure 3.6 zooms into the region 18 mm $\leq$ z $\leq$ 24 mm, which is around the streamer head. It shows the electric field and electron density on the streamer axis for different values of m.

The electric field in the streamer front shows the familiar structure: the thin and weakly curved space charge layer at $z = 20$ mm (see figure 3.4) causes the field to jump from a highly enhanced value to a quite low one. Behind the space charge layer in the streamer interior (i.e. for larger z), the electric field is largely screened. The decay length of the electric field ahead of the space charge layer (i.e. for smaller z) is determined by the radius of curvature of the space charge layer. The maximum of the field is determined dynamically. It occurs to be higher for the slower and thinner streamers with higher m values.

The electron density is shown in the lower panel of figure 3.6 on a linear scale in the streamer head region. Where the electric field is maximum, the electron density is growing rapidly, almost discontinuously, in particular for large m. The second panel of figure 3.7 shows the electron density on a logarithmic scale over a wider spatial range for $m = 1$, 17, and 26. Ahead of the front in the range of $z < 17$ mm, the electron density grows exponentially in space towards the front region, like $\exp[z/\ell]$, with the same length scale $\ell = 1.1$ mm according to a fit in the range of $z = 4$ to 15 mm for all three values of m. An analytical estimate shows that this length scale ℓ should be set by the largest photon absorption length in the photoionization model. This length is indeed 1.2 mm [16, 19]. In the high field region at $z \approx 20$ mm, the electron density increases steeply as in the linear plot of Figure 3.6.

Behind the ionization region, the electron density is nearly constant for m close to 1, but it decreases for larger m with growing distance behind the front. For $m = 17$ and $m = 26$, it saturates to about 10^{17} /m^3 at $z > 33$ mm and $z > 25$ mm respectively, which is the result of attachment and detachment reactions compensating each other. By inspecting the density of the ionic species in the streamer channel for the cases shown in the third, fourth, and fifth panels of figure 3.7, we observe that the densities of O_2^+, N_2^+, and N_4^+ differ significantly in $m = 1$, 17, and 26, whereas the densities of the other ion species are quite similar. For $m = 17$ and $m = 26$, the density of ion species also approach an identical constant value for both cases.

Surprisingly, the maximum value of the electron density generated in the ionization front is highest for the largest m - when the electron attachment rate in the region below breakdown is highest. Common estimates relate the maximum electron density behind the front to the maximum electric field at the front [10, 36, 73] though this relation somewhat deviates from numerical observations for positive streamers with photoionization [78], as discussed in section 3.4 of [97]. The present observation confirms that a higher maximum field creates a higher electron density behind the ionization front.

3.3.4 Charged species in 30 mm long streamer channels

Figure 3.7 shows the electric field, electron density, and ion species on the streamer axis throughout the whole ionized region. Here, the streamer heads have arrived at $z = 20$ mm as before.

The upper plot shows the electric field on axis, and three constant values are inserted for reference: the breakdown field of 28 kV/cm (where $\alpha_{\text{eff}} = 0$), the applied background field of 15 kV/cm, and the field of 5 kV/cm that is frequently observed in the interior of single positive streamers in air and interpreted as the so-called stability field. Far ahead of the streamers at $z \to 0$, the electric field essentially has the background value, and then it increases strongly towards the streamer head, as described above. Behind the ionization front in the streamer interior, the electric field approaches 5 kV/cm for $m = 1$, while it approaches the background field of 15 kV/cm in the cases of $m = 17$ and 26. The axis range of 45 mm $< z <$ 50 mm shows remainders of the initiation process and is not discussed further.

The different interior fields of 5 or 15 kV/cm are related to the different interior conductivities of the streamers. While for $m = 1$, there is a sufficient electron density to screen the electric field from the streamer channel, this is not the case for the middle and back regions of the streamers with $m = 17$ or 26 as we will discuss now.

The simulation results for electron attachment and ion conversion are shown in the lower three panels of figure 3.7. The reactions listed in table 3.1 involve electrons, neutrals, the positive ions N_2^+, O_2^+, N_4^+, O_4^+, and the negative ions O^-, O_2^-, O_3^-. As described in [4], all positive ions in air rapidly convert to O_4^+. This statement is confirmed by the present simulations, where the densities of the other positive ions quickly decrease behind the ionization front.

For $m = 1$, the electrons created in the ionization front attach to oxygen mainly through three-body attachment, hence the O_2^- density increases behind the moving front in about the same manner as the electron density decreases. Dissociative attachment creating O^- has no substantial contribution at standard temperature and pressure. As O_3^- is produced in collisions of O_2 with O^-, its concentration stays low as well. It is a quite stable ion in air. There is a rapid trail of positive ion conversion within the streamer head, from N_2^+ to N_4^+ to O_2^+. This is followed by the fast conversion of O_2^+ into O_4^+ in the streamer channel.

For $m = 17$ and 26, the ionization and attachment reaction rates k_1 to k_4 are enhanced by a factor m in the region below the breakdown field. This concerns the complete streamer channel. Accordingly, the electron density decreases rapidly behind the ionization front, while the O_2^- density increases in about the same manner as the electron density decreases. For both values of m, an electrically neutral streamer channel is formed, consisting mainly of O_4^+ and O_2^- ions while all other ion densities are at least an order of magnitude smaller. Note that in Figure 3.7, the yellow line that represents O_2^- mostly coincides with the green line that represents O_4^+ for $m = 17$ and 26. As ion mobility is much smaller than electron mobility and neglected in the present model, this streamer channel cannot screen the electric field anymore and the field returns to the background value.

3.3.5 Electronic and ionic currents

Since electrons are quickly attaching and disappearing behind the streamer head for large values of m, the electric current due to the electrons is significantly decreasing along the streamer channel. Thus, ionic conductivity could possibly become relevant, and we investigate that here. We performed streamer simulations which included ion motion through the drift term in equation (3.8) with the finite ion mobility given in Section 3.2.1.

The electronic conductivity was calculated with $\sigma_e = e n_e \mu_e$ and $\sigma_i = \sum_i e\,[Z_i]\,\mu_i$ was used for calculations of the ionic conductivity. From the conductivities, the current densities j_e and j_i, for the electrons and the ions respectively, were calculated using $j_e = \sigma_e E$ and $j_i = \sigma_i E$. Figure 3.8

presents the electronic and ionic current densities on the streamer axis for cases $m = 1$, 17, and 26 when the heads have arrived at $z = 20$ mm as in the previous section.

For $m = 1$, the electronic current density is nearly 3 orders of magnitude higher than the ionic current density, rendering the effect of the ions to the total current negligible. For $m = 17$ and $m = 26$, at about $z = 34$ mm and 26 mm behind the ionization front respectively, the ionic current density starts to get larger than the electronic current density. This ionic current density is of the order of 1 kA/m^2 for all values of m considered. Here, the densities of O_2^- and O_4^+ are dominating in the increased attachment cases. Due to approximate charge neutrality in the streamer channel, the electric currents of positive and negative ions contribute about equally. The ionic current densities do not have a significant effect on the streamer behavior.

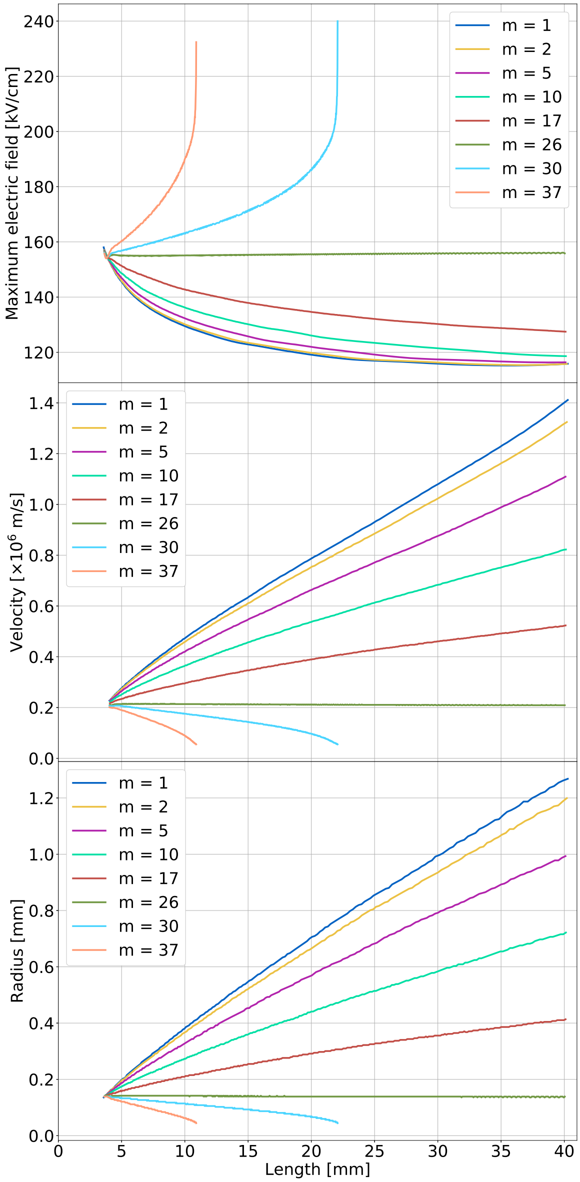

Figure 3.5: Maximum electric field (upper panel), streamer velocity (middle panel), and streamer radius (lower panel) as a function of streamer length L for different attachment rates m.

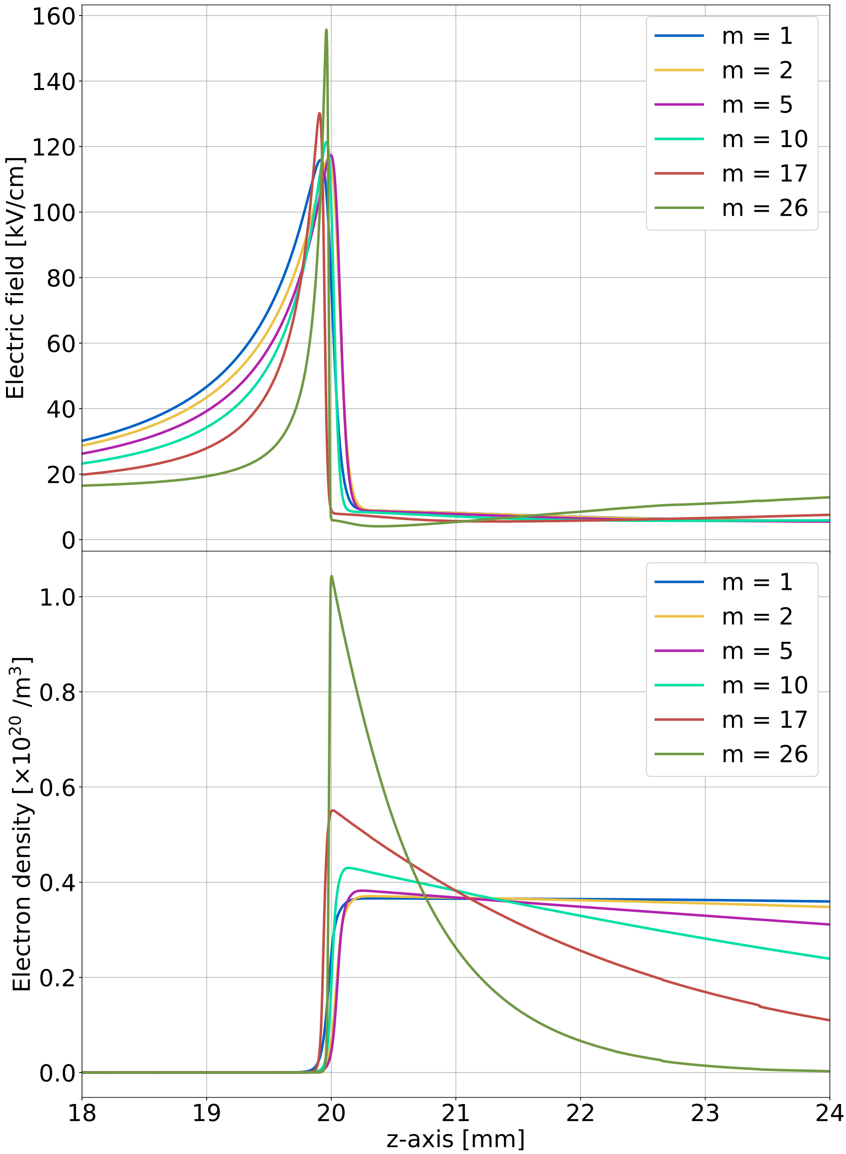

Figure 3.6: Zoom into the region around the streamer head when the streamers have reached a length of 30 mm. Shown are electric field (upper panel) and electron density (lower panel) on the streamer for different m values.

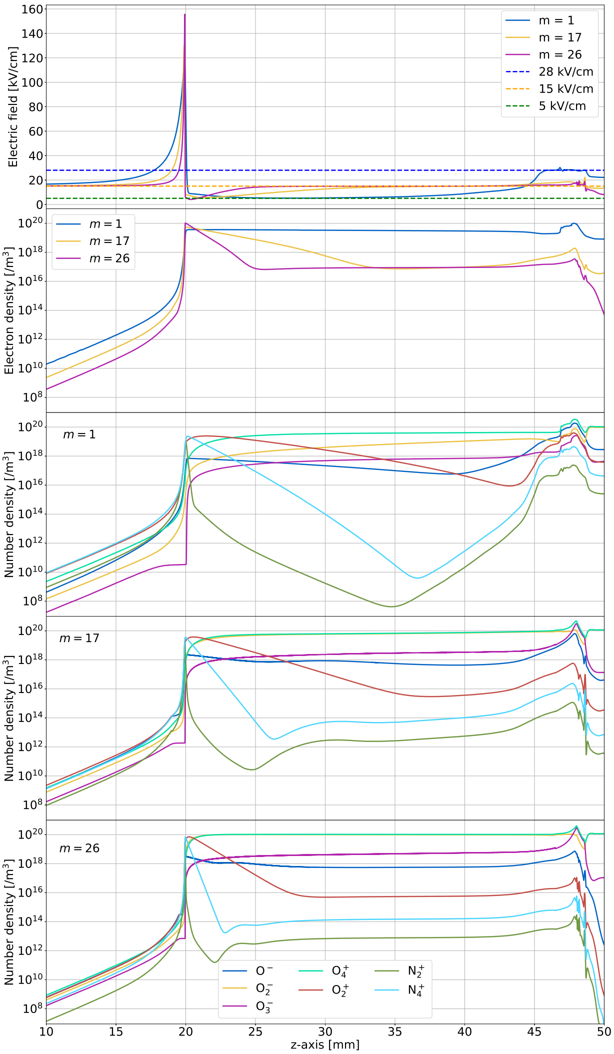

Figure 3.7: Electric field profile E (first panel), number densities of electron n_e (second panel) and all ion species for different attachment rates ($m = 1$ on third panel, $m = 17$ on fourth panel, and $m = 26$ on fifth panel) on the streamer axis. Streamers of the same length are shown. The first panel also contains dashed lines for the breakdown field 28 kV/cm, the background field 15 kV/cm, and the field 5 kV/cm for reference. Legend on the fifth panel applies for the third and fourth panels as well.

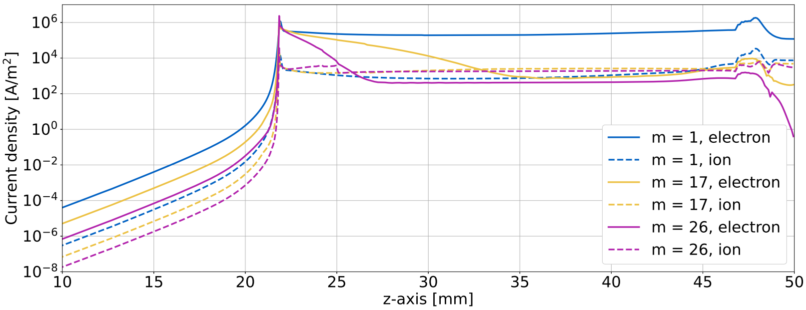

Figure 3.8: Current density profiles for different attachment rates ($m = 1$, $m = 17$, and $m = 26$) on the streamer axis. Electronic current densities are shown with solid lines and ionic current densities with broken lines. Streamers of the same length are featured.

3.4 Conclusions

3.4.1 Summary

We have simulated and analyzed single positive streamers with photoionization in a constant electric field below the breakdown value. To study systematically the effect of electron attachment and of the subsequent loss of channel conductivity on the streamer dynamics, we performed simulations in artificial air ($N_2 : O_2 = 80 : 20$) at standard temperature and pressure, and then we modified the effective ionization coefficient such that electron attachment is increased in the region below breakdown, and we kept all other parameters the same. Our main conclusions are:

1. A streamer head can keep propagating even if the ionized channel behind it loses its conductivity due to rapid electron attachment.

2. Depending on parameters, the streamer can be accelerating or decelerating. Between these parameter regimes, the streamer can propagate uniformly - with unchanged velocity and spatial structure. In this case, the electrically isolated streamer head carries a fixed amount of positive electric charge, and the electric field behind it returns to its background value.

3. It is remarkable that this uniform translation is dynamically stable, at least for the duration of our simulations. This illustrates that the streamer head is a coherent structure like a solitary wave, created by the nonlinear interaction between ionization reaction, electron motion, and local electric fields.

4. If attachment is too strong in a given electric field, the streamer radius and velocity decrease while the electric field and the charge carrier density increase rapidly. This dynamics is reminiscent of the stagnation dynamics described in [106], but in that reference the streamer channel stayed conductive.

3.4.2 Related concepts and outlook

We remark that the electrically-isolated streamer heads found here should not be confused with the glowing heads of propagating streamers as the glow only indicates the regions with a strong ionization reaction and not the conducting regions in a streamer. These should not be confused either with the isolated head model [67, 127], which ignores the existence of the streamer channel.

The behavior of the streamer in the $m = 26$ case could be related to an older definition of the streamer stability field. Before the stability field was used in relation to the minimal voltage needed for a streamer to travel a certain distance, it was defined as the homogeneous electric field where a streamer propagates without any changes in velocity and shape [44, 50, 114]. In the $m = 26$ case, the streamer can apparently propagate indefinitely in a field of 15 kV/cm in a stable manner. It could be claimed that 15 kV/cm is the stability field of the $m = 26$ streamer following its original definition. For larger m, the streamer length is limited.

Finally, the relation between radius, velocity, and maximum electric field at the streamer head, and of electron density and electric field behind the streamer ionization front should be analyzed further. The charge balance between different parts of the streamer requires further analysis as well. In this context, model reductions for uniformly-translating streamers given in [92, 110] and reviewed in [97] should be checked carefully, both on the underlying assumptions and calculations, and in comparison with simulations. These questions will be addressed in future papers, in particular, in view of deriving reduced models for streamer trees [83].

Chapter 4

Simulations of positive streamers in air in different electric fields: steady motion of solitary streamer heads and the stability field

We simulate and characterize positive streamers in ambient air in homogeneous background electric fields from 4.5 to 26 kV/cm in a 4 cm gap. They can accelerate or decelerate depending on the background electric field. Many experiments have shown that a streamer keeps propagating in a stable manner in the so-called stability field of 4.5 to 5 kV/cm. Our fluid streamer simulations in STP air show that: (1) In a homogeneous field larger than 4.675 kV/cm, a single streamer accelerates, and in a lower field, it decelerates and eventually stagnates with a small radius and very high field enhancement. (2) In a field of 4.675 kV/cm, the streamer head propagates with an approximately constant velocity of 6.7×10^4 m/s and an optical radius of 55 μm over distances of several centimeters as a stable coherent structure. These values for the radius and velocity agree well with measurements of so-called minimal streamers. (3) Behind the uniformly-translating streamer head, the channel conductivity decreases due to electron attachment and recombination, and the electric field returns to its background value about 1 cm behind the head.

The propagation behavior of the solitary streamer agrees with the original definition of the stability field, which is the homogeneous field in which a streamer can propagate with a constant speed and shape.

This chapter is published as:
Hani Francisco, Jannis Teunissen, Behnaz Bagheri, and Ute Ebert. Simulations of positive streamers in air in different electric fields: steady motion of solitary streamer heads and the stability field. *Plasma Sources Science and Technology*, 30(11):115007, November 2021

In this paper, we found that accelerating, steadily-propagating, and decelerating streamers can also be found in air when varying the background electric field. However, we implicitly assumed that uniform or steady propagation would only occur at one particular background field. This expectation was driven by the textbook concept of a unique so-called stability field. Later, in [75], it was shown that the stability field and the corresponding shape of the steadily-propagating streamer are not unique.

4.1 Introduction

Streamer discharges are transient discharges that serve as precursors to other gas discharges such as sparks and lightning leaders. They are rapidly growing ionized channels that are characterized by a curved space charge layer around their plasma body, which screens the electric field in their interior and enhances it ahead of them [11, 38, 67, 97, 103]. The enhanced field in the active zone at the streamer head exceeds the electric breakdown value, and the multiplication of electrons in this region drives the propagation of the streamer. Streamers have multiple applications in various fields including, but not limited to, medicine [70], combustion [128], and surface treatments [17].

Streamers can form even if the background electric field is below breakdown as long as there is an area where the field is enhanced above the breakdown threshold. This allows for the observation of streamers in a wide range of electric fields in the laboratory [6, 22, 114]. Numerically, it has been a challenge to study streamers in low background electric fields due to issues related to streamer initiation and streamer branching [79]. In [106], a streamer simulation was performed with a low background electric field, and that led to the first study of streamer stagnation dynamics. This was studied more recently in [131] where decelerating streamers were obtained by having inhomogenous gas density.

In this paper, we employ an approach that allows us to look at streamers propagating in low background fields: we initiate the streamer in a higher field, let it propagate for some time, and then reduce the background electric field to a much lower value. This scheme allows us to do a parameter sweep of background electric fields farther below electric breakdown, going as low as 4.5 kV/cm.

In a recent paper [39], we have studied single positive streamers in dry air in a homogeneous background electric field of 15 kV/cm, about half the breakdown field, at standard temperature and pressure. The radius and the velocity of the streamers increased with the streamer length, as observed by many authors before. When the electron attachment rate was artificially increased in regions below electric breakdown, we found that with increasing attachment rate, streamer velocities and radii could grow less, not at all, or even decrease. Additionally, streamer heads could keep propagating even if the conductivity of the streamer channels was already negligible a short distance behind the streamer head. We did not specify gases where such dynamics could actually be observed.

In the current work, we show that the same variation of streamer dynamics can occur in ambient air by simply decreasing the homogeneous background electric field. We find that for a background field of about 4.675 kV/cm, the streamer head propagates with a constant radius and velocity. The current that flows through the streamer channel is already negligible close behind the head - the electric field returns to the background field value at the back of an electrically isolated streamer head. If the background electric field is even smaller, the streamer velocity and radius decrease while the maximal electric field at the head rapidly increases, and this could go on until the streamer stops. Finding uniform streamer propagation in STP air confirms the old concept of the stability field [44, 50, 114] that is frequently used in high voltage engineering but had little support up to now from fundamental physical modeling.

The paper is structured as follows. Details about the numerical modeling are presented in section 4.2, where the computational domain is described along with the initial conditions of the simulations in section 4.2.3. Section 4.3 features and discusses the results of our simulations. In section 4.3.1, we present the case of a uniformly translating streamer in ambient air together with the more familiar case of an accelerating streamer, and in section 4.3.2, we show how streamer behaviour more generally depends on the background electric field. We also include decelerating streamers in that section. Section 4.4 has comparisons between our simulation results and experimental measurements, and we discuss there the original concept of the stability field and its connection to our solitary streamers. We conclude in section 4.5, where we summarize our results and communicate ideas for future studies.

4.2 Discharge model

4.2.1 Model equations and reactions

We used a plasma fluid model with local field approximation to simulate positive streamers in artificial dry air at standard temperature and pressure

1	$e + \mathrm{N_2} \rightarrow 2e + \mathrm{N_2^+}$	$k_1\,(E/N)$
2	$e + \mathrm{O_2} \rightarrow 2e + \mathrm{O_2^+}$	$k_2\,(E/N)$
3	$e + \mathrm{O_2} + \mathrm{O_2} \rightarrow \mathrm{O_2^-} + \mathrm{O_2}$	$k_3\,(E/N)$
4	$e + \mathrm{O_2} \rightarrow \mathrm{O} + \mathrm{O^-}$	$k_4\,(E/N)$
5	$\mathrm{M} + \mathrm{O_2^-} \rightarrow e + \mathrm{O_2} + \mathrm{M}$	$k_5\,(E/N)$
6	$\mathrm{N_2} + \mathrm{O^-} \rightarrow e + \mathrm{N_2O}$	$k_6\,(E/N)$
7	$\mathrm{O_2} + \mathrm{O^-} \rightarrow \mathrm{O_2^-} + \mathrm{O}$	$k_7\,(E/N)$
8	$\mathrm{O_2} + \mathrm{O^-} + \mathrm{M} \rightarrow \mathrm{O_3^-} + \mathrm{M}$	$k_8\,(E/N)$
9	$\mathrm{N_2^+} + \mathrm{N_2} + \mathrm{M} \rightarrow \mathrm{N_4^+} + \mathrm{M}$	k_9
10	$\mathrm{N_4^+} + \mathrm{O_2} \rightarrow 2\mathrm{N_2} + \mathrm{O_2^+}$	k_{10}
11	$\mathrm{O_2^+} + \mathrm{O_2} + \mathrm{M} \rightarrow \mathrm{O_4^+} + \mathrm{M}$	k_{11}
12	$e + \mathrm{O_4^+} \rightarrow 2\mathrm{O_2}$	$k_{12}\,(E/N)$

Table 4.1: List of reactions included in the model. M stands for both $\mathrm{O_2}$ and $\mathrm{N_2}$, and E/N is the reduced electric field calculated from the electric field E and the gas density N. The electron impact reactions $1 - 4$ have reaction rate coefficients calculated with Bolsig+ [54] while the reaction rate coefficients of the ion reactions $5 - 11$ were taken from [4, 107]. The reaction rate coefficient of reaction 12 is calculated [65] from the mean electron energy calculation of Bolsig+.

at different homogeneous background electric fields. The model equations, transport coefficients, and included reactions and reaction rate coefficients are the same as in our earlier paper [39].

The electron density n_e evolves in time according to the equation

$$\frac{\partial n_e}{\partial t} = \nabla \cdot (n_e \mu_e \mathbf{E} + D_e \nabla n_e) + S_i - S_\eta + S_{ph} + S_{ion}, \tag{4.1}$$

where μ_e is the electron mobility, $\mathbf{E}$ is the electric field, D_e is the electron diffusion coefficient, S_i is the impact ionization source term, S_η is the electron attachment source term, S_{ph} is the non-local photoionization source term, and S_{ion} is the source term for electron detachment reactions minus the electron-ion recombination reaction. Table 4.1 summarizes the reactions incorporated in the model.

We used the reactions given in [81] excluding the ion-ion recombination reactions and the reactions that involved water. This chemical model is based on [4, 65, 107] and focuses on the electron density evolution, in accordance with our focus on the conductivity inside the streamer channel.

Nearly all reaction rate coefficients in Table 4.1 are a function of the reduced electric field, and only reactions 9-11 have constant reaction rate coefficients. The electron Boltzmann equation solver Bolsig+ [54] was utilized under the assumption of spatially dependent electron density evolution to calculate the reaction rate coefficients for the electron impact reactions and the transport coefficients μ_e and D_e using electron-neutral scattering cross sections obtained from the Phelps database [1, 113] retrieved in March 2019.

The source terms for impact ionization, electron attachment, and electron detachment minus electron-ion recombination are computed using

$$S_i = k_1 n_e \left[\mathrm{N_2}\right] + k_2 n_e \left[\mathrm{O_2}\right], \tag{4.2}$$

$$S_\eta = k_3 n_e \left[\mathrm{O_2}\right]^2 + k_4 n_e \left[\mathrm{O_2}\right]. \tag{4.3}$$

$$S_{ion} = k_5 \left[\mathrm{M}\right] \left[\mathrm{O_2^-}\right] + k_6 \left[\mathrm{N_2}\right] \left[\mathrm{O^-}\right] - k_{12} n_e \left[\mathrm{O_4^+}\right], \tag{4.4}$$

where $[\mathrm{Z}_i]$ stands for the density of the species Z_i, and $[\mathrm{M}] = [\mathrm{N_2}] + [\mathrm{O_2}]$. $[\mathrm{N_2}]$ and $[\mathrm{O_2}]$ are assumed to be constant in our simulations as the degree of ionization within streamers at standard temperature and pressure is small.

The photoionization source term is given by

$$S_{ph}(\mathbf{r}) = \int d^3r' \, \frac{I(\mathbf{r}')f(|\mathbf{r} - \mathbf{r}'|)}{4\pi|\mathbf{r} - \mathbf{r}'|^2} \tag{4.5}$$

where $I(\mathbf{r})$ is the source of ionizing photons, $f(r)$ is the absorption function, and $4\pi|\mathbf{r} - \mathbf{r}'|^2$ is a geometric factor. Following Zheleznyak's model [149], the photon source term $I(\mathbf{r})$ is calculated using

$$I(\mathbf{r}) = \frac{p_q}{p + p_q} \xi S_i(\mathbf{r}) \tag{4.6}$$

where p is the actual gas pressure, p_q is a gas-specific quenching pressure, and ξ is a proportionality factor. In principle, this proportionality factor is field-dependent [149], but in this paper, we set it to $\xi = 0.075$. Furthermore, we use a quenching pressure of $p_q = 40\,\mathrm{mbar}$. In Zheleznyak's model, $f(r)$ is an effective function for the absorption of photons in the wave length range of 98 to 102.5 nm. It is obtained with

$$f(r) = \frac{\exp(-\chi_{\mathrm{min}} p_{O_2} r) - \exp(-\chi_{\mathrm{max}} p_{O_2} r)}{r \ln(\chi_{\mathrm{max}}/\chi_{\mathrm{min}})}, \tag{4.7}$$

where $\chi_{\mathrm{max}} \approx 1.5 \times 10^2/(\mathrm{mm\ bar})$, $\chi_{\mathrm{min}} \approx 2.6/(\mathrm{mm\ bar})$, and p_{O_2} is the partial pressure of oxygen. We used a set of Helmholtz differential equations [19, 84] with Bourdon's three-term parameters [19] to evaluate the photoionization integral.

The charged species N_2^+, N_4^+, O_2^+, O_4^+, O^-, O_2^-, and O_3^-, and the neutral species O and $\mathrm{N_2O}$ evolve in time according to the continuity equation

$$\frac{\partial [Z_i]}{\partial t} = -s_i \nabla \cdot ([Z_i]\, \mu_i \mathbf{E}) + S_{Z_i} \tag{4.8}$$

where $s_i = \pm 1$ is the sign of the electric charge of species i and μ_i is their mobility. Since ion mobilities are typically about two orders of magnitude lower than electron mobilities, we neglect ion motion for simplicity in most of this paper. However, we investigate the effect of ion motion in section 4.3.5, in which all ion mobilities are set to 2.2 $\times 10^{-4}$ $\mathrm{m}^2/\mathrm{V\ s}$ [138]. Finally, neutral species are always immobile in our simulations.

Calculations for the electric potential ϕ and the electric field use the equations

$$\nabla^2 \phi = -\frac{\rho}{\epsilon_0}, \quad \mathbf{E} = -\nabla \phi, \tag{4.9}$$

where ρ is the space charge density and ϵ_0 is the vacuum permittivity. The space charge density is calculated using $\rho = e\,(n_i - n_e)$ where e is the elementary charge and n_i is the density of all positive ions minus the density of all negative ions.

4.2.2 Computational method and domain

The simulations were run using Afivo-streamer [136, 137], a simulation tool for plasma fluid models that uses geometric multigrid techniques, an octree-based adaptive mesh refinement system, and OpenMP parallelization. The present results are for single streamers, and these assume that they are cylindrically symmetric. This allows the calculation to be performed effectively in just the two coordinates r and z.

Our computational domain in this study is cylindrically symmetric and has a length of 40 mm and a radius of 20 mm. To disregard boundary effects, the simulation is set to end once the streamer head is within 10 mm from the opposite end of the domain. The streamer head position is identified as the point where the electric field is maximum in the domain.

The electric potential was fixed at $z = 0$ mm and $z = 40$ mm to achieve a homogeneous background electric field pointing in the $-\hat{z}$ direction. At $r = 20$ mm, Neumann zero boundary conditions ($\partial_r \phi = 0$) were applied on the electric potential, and for $r = 0$ mm, the boundary condition follows from cylindrical symmetry. Neumann zero boundary conditions are applied for the electron density at all boundaries, and no background ionization was introduced into the domain.

We used the same refinement criteria as described in [39]: Adaptive mesh refinement is employed with the grid set to have a minimum size of 2.4 μm. The refinement and derefinement criteria are based on the local electric field value as in [136] with an additional criterion based on the charge density: refine if $\alpha(1.2 \times E)\Delta x > 0.5$ and derefine if both $\alpha(1.2 \times E)\Delta x < 7.5 \times 10^{-2}$ and $|\rho|/\epsilon_0 < 9.0 \times 10^{10}$ V/m^2, where $\alpha(E)$ is the field-dependent ionization coefficient, E is the electric field strength, and Δx is the grid spacing. To obtain a clearer picture of the equipotential lines in the regions behind the streamer head, we modified our derefinement criterion for the streamers with a background field of 4.65 kV/cm and below so that derefinement stops when the cell width gets to 4 μm.

4.2.3 Initial conditions

For homogeneous background electric fields of at least 14 kV/cm, streamers easily initiate and propagate from a neutral seed of equal electron and positive ion densities, which we placed on the upper boundary of the domain, along the axis of symmetry. Another neutral seed is placed below the first seed to provide an initial source of electrons. The first seed is 0.25 mm wide, 1 mm long, and has $2.25 \times 10^{20}/\mathrm{m}^3$ electrons and positive ions while the second seed is 0.2 mm wide, 2 mm long, and has $10^{17}/\mathrm{m}^3$ electrons and positive ions. Both seeds decay with a Gaussian profile. This set-up is illustrated in the left-most panel of figure 4.1.

Single streamers are more difficult to obtain in lower background electric fields because either the field enhancement proves to be insufficient for streamers to initiate or the streamer branches after propagating a short length. Branching breaks the cylindrical symmetry of a single streamer channel, and thus cylindrically symmetric simulations are not appropriate to describe such phenomena [80]. To investigate low-field streamers, a streamer is first initiated and allowed to propagate for some time in a higher background field before the background electric field is instantaneously reduced to a lower value. This approach allows us to study single continuously propagating and non-branching streamers in fields lower than 14 kV/cm.

For electric fields from 9 kV/cm to 12 kV/cm, a streamer was first initiated in a field of 14 kV/cm and allowed to grow for 20 ns before instantaneously reducing the background electric field. Thus, the low-field streamers grow from a streamer with a 53.5 μm radius and head at $z =$ 37.6 mm as shown in the middle panel of figure 4.1.

For even lower fields, this approach still encounters the same initiation and branching problems that were previously stated. Thus, for streamers in background electric fields below 9 kV/cm, we used the 9 kV/cm streamer after 40 ns of propagation as the initial condition, i.e. the field was reduced twice. First, the field was changed from 14 to 9 kV/cm after 20 ns, and then it was modified further to the final electric field after 40 ns. This gives a 155 μm wide streamer with its head at $z = 33.4$ mm as the starting state for these lower field simulations. This initial condition can be seen in the right-most panel of figure 4.1, which matches the left-most panel of figure 4.2. This last approach allowed us to simulate single streamers in

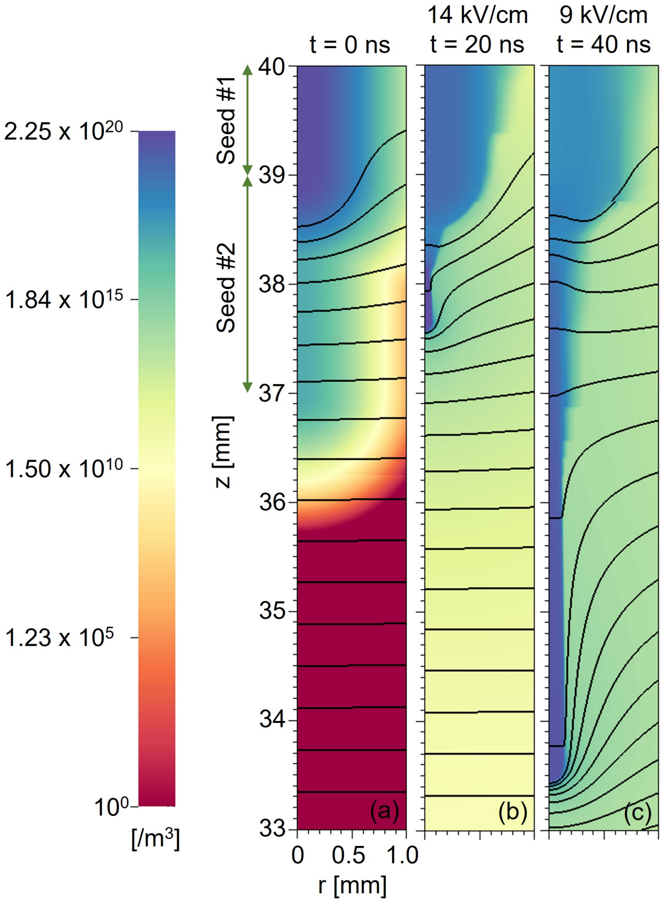

Figure 4.1: Initial conditions for the different background electric fields used in this paper. Shown are contour plots for the electron number densities together with black equipotential lines. The leftmost panel (a) is for streamers in background fields of 14 kV/cm and higher, the middle panel (b) is for streamers with background fields below 14 kV/cm to 9 kV/cm, and the rightmost panel (c) is for streamers in fields below 9 kV/cm. Note that the computational domain extends from 0 to 40 mm in the z direction and 0 to 20 mm in the r direction, and only a part of the domain is shown in this figure.

1	$e + N_2 \to e + N_2\left(C^3\Pi_u\right)$	$k_{ex}\left(E/N\right)$
2	$N_2\left(C^3\Pi_u\right) + N_2 \to 2N_2$	$k_q^{N_2}$
3	$N_2\left(C^3\Pi_u\right) + O_2 \to N_2 + O_2$	$k_q^{O_2}$
4	$N_2\left(C^3\Pi_u\right) \to N_2\left(B^3\Pi_g\right) + h\nu$	$1/\tau_0$

Table 4.2: Reactions to calculate the optical emission of streamers. Bolsig+ [54] with the Phelps database [113, 1] was used to calculate for $k_{ex}\left(E/N\right)$, while $k_q^{N_2} = 0.13 \times 10^{-10}$ cm^3/s, $k_q^{O_2} = 3.0 \times 10^{-10}$ cm^3/s, and $\tau_0 = 42$ ns are from [105]. Reaction 4 leads to the emission of optical photons with wavelength 337.1 nm [105] or energy 3.7 eV.

background electric fields as low as 4.5 kV/cm.

4.2.4 Calculation of optical radii

All radii given in the present paper are optical radii, as they would be measured experimentally. More precisely, this optical radius is half of the full width at half maximum (FWHM) of the calculated optical emission, in contrast to the definition of the streamer radius as the location of the maximum of the radial component of the electric field in previous papers [15, 39]. Four additional reactions were added to our model to incorporate the density of $N_2\left(C^3\Pi_u\right)$, the excited state of N_2 responsible for most radiation in the visible spectral region [103]. These reactions are listed in Table 4.2 with their corresponding reaction rate coefficients.

We compute the optical radius from the density of $N_2\left(C^3\Pi_u\right)$. A forward Abel transform was done on $\left[N_2\left(C^3\Pi_u\right)\right]$ in cylindrical coordinates to get its 2D projection in Cartesian coordinates. From the 2D projection we only considered the area below $z = 33$ mm to disregard the effects of the seeds used for initiation. The densities were normalized and summed along the vertical axis, producing a 1D profile along the horizontal axis from where we searched for the maximum density. From the point of maximum density, the farthest coordinates in the horizontal direction where the density was at least half of the maximum density were identified, and the distance between these two identified points was regarded as the head diameter. Half of that value is the optical radius we report.

4.3 Simulation results

First, in section 4.3.1, we will discuss the particular cases of single streamers in a background field of 4.65 kV/cm and 14 kV/cm which are examples of solitary and accelerating streamers. Then we will look at streamer behavior as a function of the background field in section 4.3.2.

4.3.1 Solitary streamers and accelerating streamers

Figure 4.2 shows the evolution of streamers in background electric fields of 4.65 and 14 kV/cm. The panels show the color-coded electron density together with equipotential lines in purple. For the lower field, the streamer is shown in time steps of 100 ns, while for the higher field, in time steps of 17.5 ns. The same streamers are presented in figure 4.3 showing the electric potential, the electric field and the electron density along the streamer axis, and the line charge density and the electric current. The last two are obtained by integrating the charge density and the current density across the streamer cross section. The integration was done up to $r = 5$ mm. Several basic differences can be noted between the two streamers as they propagate through the 40 mm gap.

The solitary streamer. The streamer in the 4.65 kV/cm field grows by about an equal length within each time step of 100 ns. The electron density is strongly reduced about 10 mm behind the streamer head, and the electric field returns to its background value in this region and further behind, as can be seen from the straight and equidistant equipotential lines. Overall, the pattern of electron density and deflected equipotential lines is transported almost uniformly, without changes in shape. The streamer transports a constant amount of positive charge within its finite length, and there is no negative charge visible in the line charge density in Fig. 4.3. We will call this streamer a solitary streamer or a uniformly translating streamer.

The accelerating streamer. The streamer in the 14 kV/cm field is shown in time steps of 17.5 ns in Fig. 4.2. It clearly accelerates, and its head radius increases. The electron density varies little along the whole channel for all time steps. There is electric current flowing in the order of 100 mA along the whole channel, and the back part charges negatively while the front part accumulates positive charge - there is electric polarization along

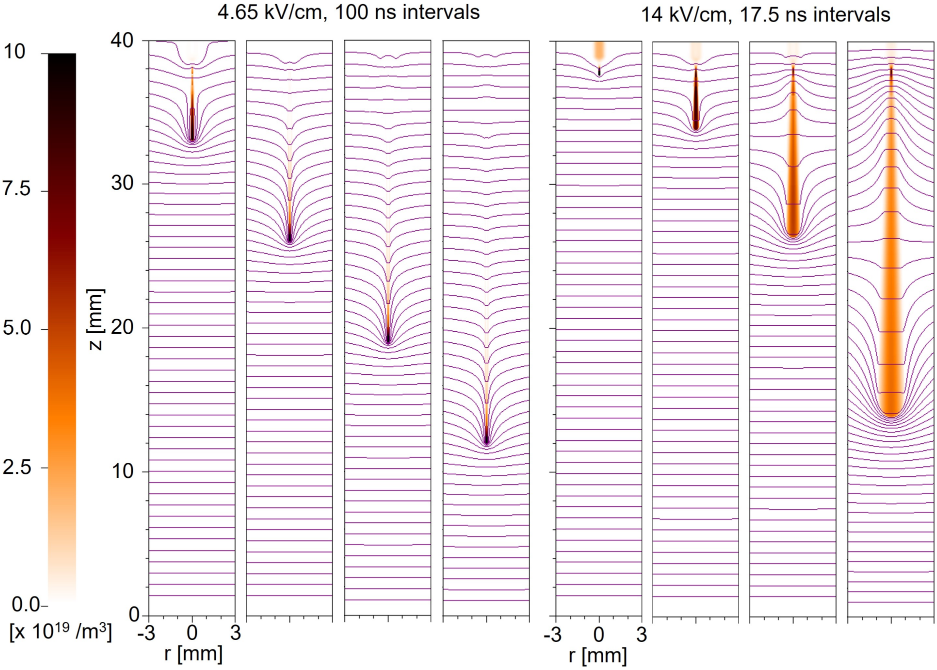

Figure 4.2: Time evolution of the electron density of streamers in air at different background electric fields. Purple equipotential lines are included. The panels of the 4.65 kV/cm streamer differ by time steps of 100 ns, while the 14 kV/cm streamer is shown in time steps of 17.5 ns. The full z axis is shown, but the figure zooms into the radial region $r \leq 3$ mm, while the full simulation domain extends up to $r = 20$ mm. Note that despite the limit in the color legend, the maximum electron density for the presented cases of the 4.65 kV/cm streamer goes above 10×10^{19} /m^3.

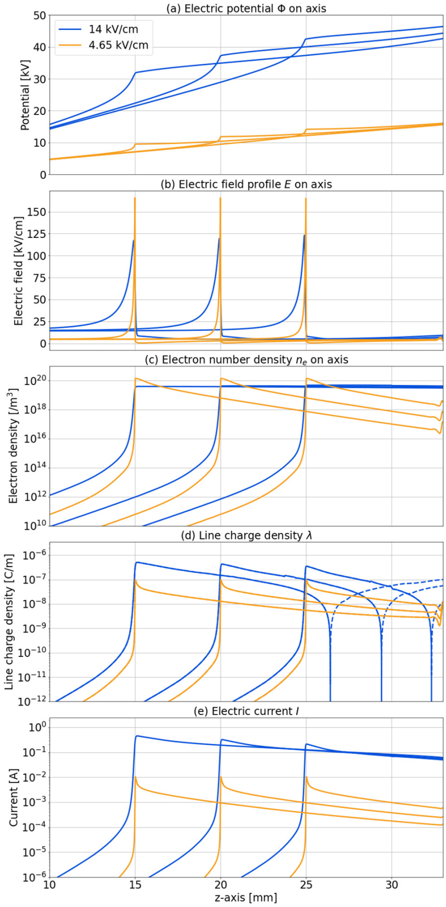

Figure 4.3: Axial profiles, line charge density, and current of the streamers in the same background fields of 14 and 4.65 kV/cm as in figure 4.2. Here they are shown when their maximal electric field is at z = 15, 20, and 25 mm. The panels show, from top to bottom, as a function of the axis coordinate z: (a) the electric potential ϕ on axis, (b) the electric field profile E on axis, (c) the electron number density n_e on axis, (d) the line charge density λ, which is the charge density integrated over the radial cross section (where the dashed lines represent negative values), (e) the electric current I, which is the current density also integrated over the radial cross section. The legend on the first panel applies to all panels.

the whole channel. This is visible in the line charge density as well as in the field distortion along the whole body of the streamer channel. We will call this streamer an accelerating streamer.

Later in section 4.3.2 we will also discuss decelerating streamers and the fact that the solitary streamers exist only on the borderline between accelerating and decelerating streamers.

Attachment and recombination. The lowest electric field inside the accelerating streamer is 4.7 kV/cm, located around the middle section of the streamer channel. For the solitary streamer in the 4.65 kV/cm background field, the electric field right behind the ionization front is as low as 0.5 kV/cm and rises to the background value behind the solitary structure.

The different interior electric fields and ion densities determine the attachment times - the average times until an electron attaches to an oxygen molecule, and the recombination times - the average times until an electron recombines with an O_4^+ ion. It should be noted here that the positive ions rapidly convert into O_4^+ ions. Together with the streamer velocity, these times determine over which length the streamer maintains its conductivity.

Figure 4.4 shows some recombination times for different O_4^+ densities and the attachment time against the electric field. The two crosses correspond to the recombination times in the interior of the 14 kV/cm streamer and of the 4.65 kV/cm streamer. The recombination times and attachment times in the solitary streamer channel are as short as about 25 ns due to the combination of low electric field and high O_4^+ density, while they are of the order of 105 ns for the accelerating streamer. The high O_4^+ density in the solitary streamer is due to the high electric field at its tip; this high field creates a high ionization density.

The slow propagation of the solitary streamer also gives electrons sufficient time to get attached to oxygen molecules and recombine with O_4^+ molecules. The accelerating streamer propagates much faster, with a higher internal field, leaving no time for electron attachment or recombination. We see in the third panel of Figure 4.3 that the electron density of the solitary streamer decays behind the ionization front by several orders of magnitude while the electron density in the channel of the accelerating streamer is essentially constant.

In Figure 4.5, several plots zooming in on the head of the solitary streamer are presented. The electric field inside the channel of the soli-

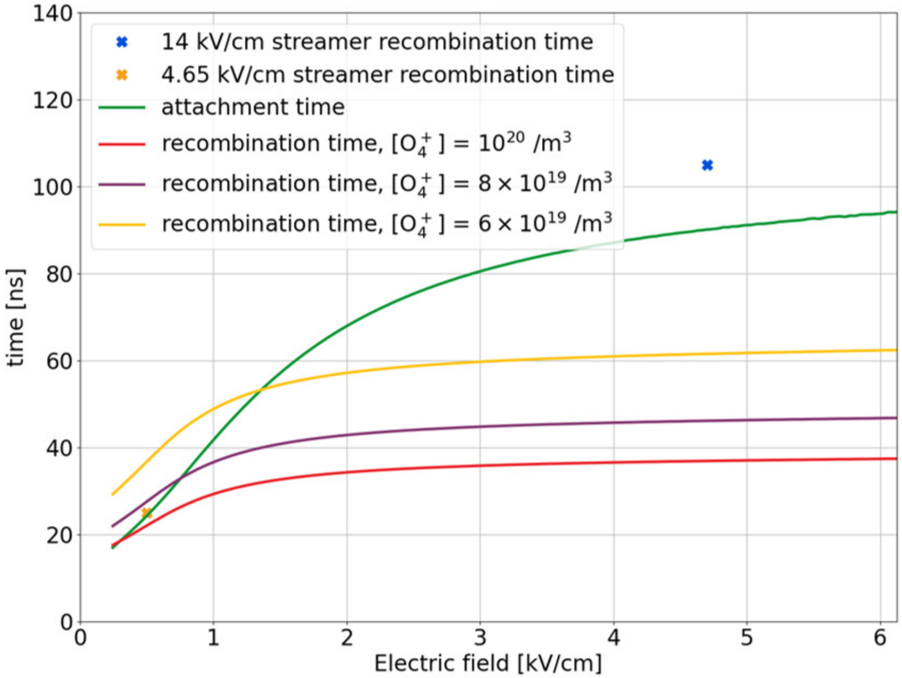

Figure 4.4: Attachment and electron-ion recombination time in STP air. The attachment time is plotted as a function of the electric field E in green. The recombination time depends on electric field E and on O_4^+ density, and lines for three different O_4^+ densities are presented. The attachment and recombination times in the channel of the 14 kV/cm and 4.65 kV/cm streamers are also included as blue and orange crosses for interior electric fields of 4.7 kV/cm and 0.5 kV/cm.

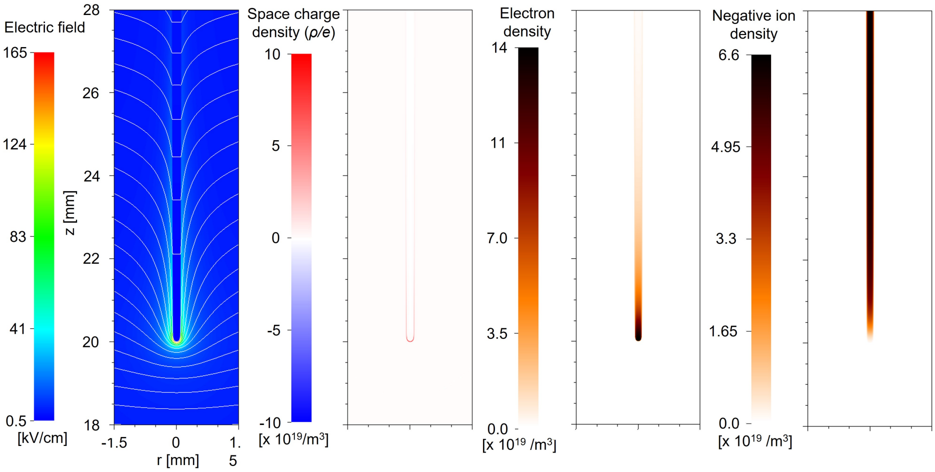

Figure 4.5: Plots of the 4.65 kV/cm streamer zoomed into the streamer head when it is at $z = 20$ mm. From left to right: (1) electric field with white equipotential lines, (2) space charge density, (3) electron density, and (4) negative ion density.

tary streamer is screened to a low value, represented by the widely separated horizontal equipotential lines. Almost all the net charge is located on the streamer surface - the positive space charge layer shown in the second panel of Fig. 4.5. The low electric field in the streamer interior leads to fast electron attachment as discussed above, and this is evident in the electron density contour plot, where the electron density reduces in magnitude behind the streamer head. Electron attachment produces negative ions, and since recombination time and attachment time are nearly equal behind the ionization front, about half of the electrons are lost due to attachment and the other half to electron-ion recombination. Thus, the density of negative ions at the back end of the channel is about half of the electron density at the streamer head.

4.3.2 Propagation modes as a function of the field

Three parameter regimes can be identified in Figure 4.6, which has the velocity, optical radius, and maximum electric field of the streamers as a function of length. First, there are the accelerating streamers that speed up as they lengthen, and their radius increases as they accelerate. This is the case for streamers in background electric fields above 4.65 kV/cm. This is also the case most frequently reported and commonly observed in streamer simulations.

Second, there are uniformly propagating streamers, in a background field of 4.65 kV/cm. They exist as a limit between accelerating and decelerating streamers, and they maintain a nearly uniform velocity. Other streamer properties such as the head radius and enhanced electric field do not change in time either. For the streamer in our simulation, the radius remained at 65 μm while it was uniformly propagating. These solitary streamers can maintain their shape because they have a finite and constant length where the electron density is relevant and the electric field is modified. They carry a fixed amount of positive charge over a finite length, and therefore act as a point charge from a sufficiently far distance. The streamer is able to propagate indefinitely in this background field. This behavior can be related to the old concept of the streamer stability field, which we discuss further in section 4.4.1.

Third and last, there are the decelerating streamers. We find them in fields below 4.65 kV/cm. Streamers in such fields slow down as they

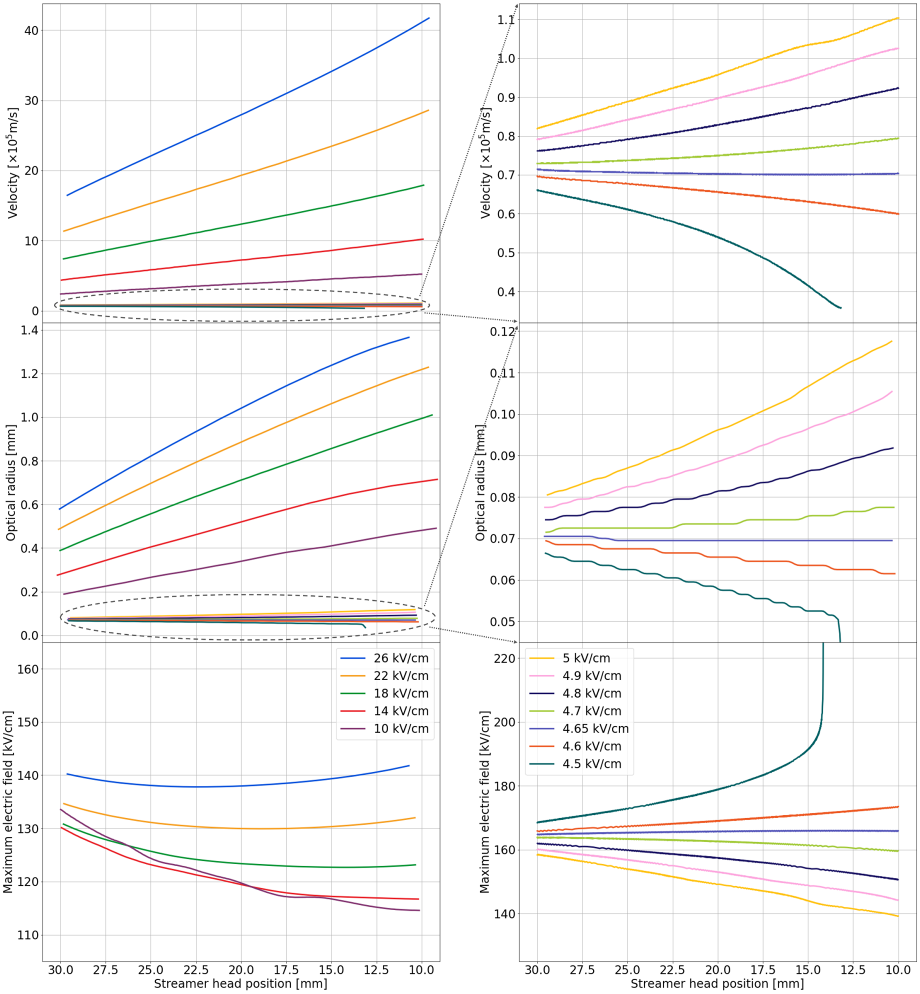

Figure 4.6: Properties of positive streamers as a function of length in different background fields, as indicated in the panels. Top panels show the streamer velocity, middle panels the optical radius, and bottom panels the maximum electric field. Plots on the right have a different range of values in the vertical axis and focus on the streamers in fields of 5 kV/cm and lower. Radii have uncertainties of ±1.2 μm due to the finite size of the numerical grid.

lengthen, and their head radius decreases in time while the maximum electric field increases. This happens because the electric screening of the streamer interior improves when the ionization front slows down. The decreasing radii of the decelerating streamers can be explained by the decreasing potential in the streamer head due to voltage lost in the streamer channel [131]. Some of our simulated decelerating streamers do not manage to cross the domain, as shown by the case of the streamer with a background field of 4.5 kV/cm. The streamer decelerated and eventually stagnated with a streamer radius of 49 μm. This stagnating behavior was described earlier in [106, 130, 131] and observed experimentally in [22, 117]. Numerically, we observe that the simulation time steps, which are usually in picoseconds, drop by two orders of magnitude because the maximum electric field values suddenly increase to magnitudes greater than 300 kV/cm in a very small region ahead of the ionization front. One reason for this numerical instability may be the artificial diffusion of electrons from the channel to the high-field region ahead of the streamer tip [135]. The physical process of streamer stagnation was always accompanied by such numerical instabilities in our simulations.

Although we used different initial conditions depending on the applied electric field, we still expect actual streamers in low background fields to grow in a similar manner as we've identified. Streamers are characterized by their velocity, radius, and maximal electric field, which determine how they propagate. As long as they share the same properties as our results, their dynamics would be the same. Additionally, in [106] it was observed that beyond 1 cm from the point of initiation, the initial condition is forgotten by the streamer.

4.3.3 Nonlinear dependence of field enhancement and plasma chemistry on the background field

The streamer dynamics nonlinearly depend on the background electric field E_{back}. In the top panel of Figure 4.7, we see the maximal field E_{max} as a function of the background field E_{back}, evaluated at the moment when the streamer heads are at $z = 20$ mm. The curve has a minimum of about $E_{\text{max}} = 120$ kV/cm for a background electric field around $E_{\text{back}} = 12$ kV/cm. For E_{back} increasing up to 26 kV/cm, the maximal

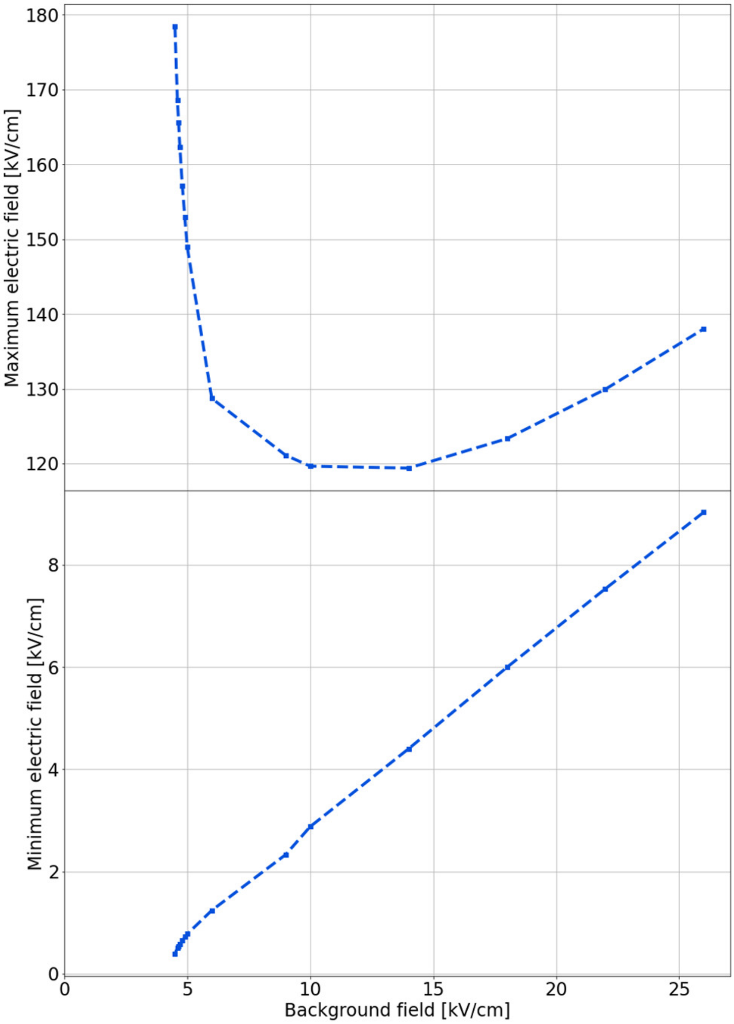

Figure 4.7: Maximal (top) and minimal (bottom) electric field in the streamer as a function of the background electric field. The maximal field is measured at the streamer head while the minimal field is from behind the streamer ionization front. The values were acquired when the streamer heads were at position $z = 20$ mm.

field increases up to 140 kV/cm, while below 10 kV/cm the maximal electric field increases rapidly, until it diverges for $E_{\text{back}} = 4.5$ kV/cm. As the electron energy distribution and the induced plasma chemistry depend on the electric field configuration, we conclude that the plasma chemistry could also depend nonlinearly on the background electric field. This observation requires further investigation in the future.

The minimum electric field behind the ionization front of the streamers as a function of the background field is presented in the bottom panel of Figure 4.7. We found that the minimum electric field inside the streamer channel depends almost linearly on the background electric field. It vanishes for the stagnating streamer, and it reaches 9 kV/cm for $E_{\text{back}} = 26$ kV/cm.

4.3.4 Heating

In [63] a streamer that propagated for a few hundred nanoseconds was found to already heat the gas significantly. As the solitary streamer also took a couple hundred nanoseconds to cross the computational domain, we evaluated the temperature increase. We used the expression $Q = \int \mathbf{j} \cdot \mathbf{E}\, dt$ [3] to calculate the deposited electric energy density Q; here $\mathbf{j}$ is the electric current density. Even if we assume that the full deposited energy is converted into heat, the temperature on the axis of the solitary streamer increases only by 6 K after 400 ns.

The difference with the result of [63] lies in the fact that the energy deposition per electron is not determined by time, but by the distance the electron travels in the electric field. In the solitary streamer the electrons attach or recombine after a short propagation distance. It should be noted though that the electron density is higher in the head of the solitary streamer than in a higher background electric field.

4.3.5 Ion motion

As electrons attach to oxygen and form negative ions in the channel, we briefly explore the effect of ion motion on streamer behavior. Incorporating ion motion in streamer simulations with 14 kV/cm and 9 kV/cm background fields did not visibly change anything in the results. For these cases, the streamer still propagates fast enough that ion motion has negligible effects. We only start to observe effects in low background electric fields, when enough time is available to deplete the electron density through attachment and recombination.

Figure 4.8 shows the total charge density of the solitary streamer with and without ion motion. We see that the channel of the streamer with ion motion is wider at the back. The space charge layer of these streamers is made up of positive ions, and without ion motion they remain fixed in space. Only reactions can change the densities of these ions in time. With the inclusion of ion motion, these ions are now moving radially outward in response to the electric field they are subjected to. The ion drift in the local field also causes the streamer head to lose some focus, leading to slower propagation. We observe similar phenomena in negative streamers, whose space charge layers are made up of the very mobile electrons.

When ion motion is included, the streamer propagates more slowly. This can be observed in the upper panel of Figure 4.9, where streamers in the same background field with and without ion motion are presented. The previously discovered uniformly translating streamer at 4.65 kV/cm decelerates when ion motion is included in the simulation. A new background electric field for uniform translation was found at 4.675 kV/cm, only slightly higher than the previous background field, with a slightly lower uniform velocity of 0.66×10^5 m/s. Thus, the effect of ion motion on streamer dynamics does not appear to be strong in this case. We will be using this new uniformly translating streamer for our comparisons in section 4.4.

The maximal electric field of the streamers in fields of 4.65 to 4.7 kV/cm with and without ion motion is plotted as a function of the streamer head position in the lower panel of Figure 4.9. When ion motion is included, the maximal electric fields at the same background electric field are higher, which is consistent with the smaller head radii.

Finally, we compare the maximal electron drift velocity with the velocity of the uniformly translating streamer with ion motion. The maximal electric field at the streamer head has a constant value of 171 kV/cm, which gives us an electron drift velocity of 5.3×10^5 m/s, while the streamer velocity is 6.6×10^4 m/s - almost an order of magnitude smaller than the drift velocity. This is possible for positive streamers, where these velocities are directed in opposite directions, but not for negative streamers.

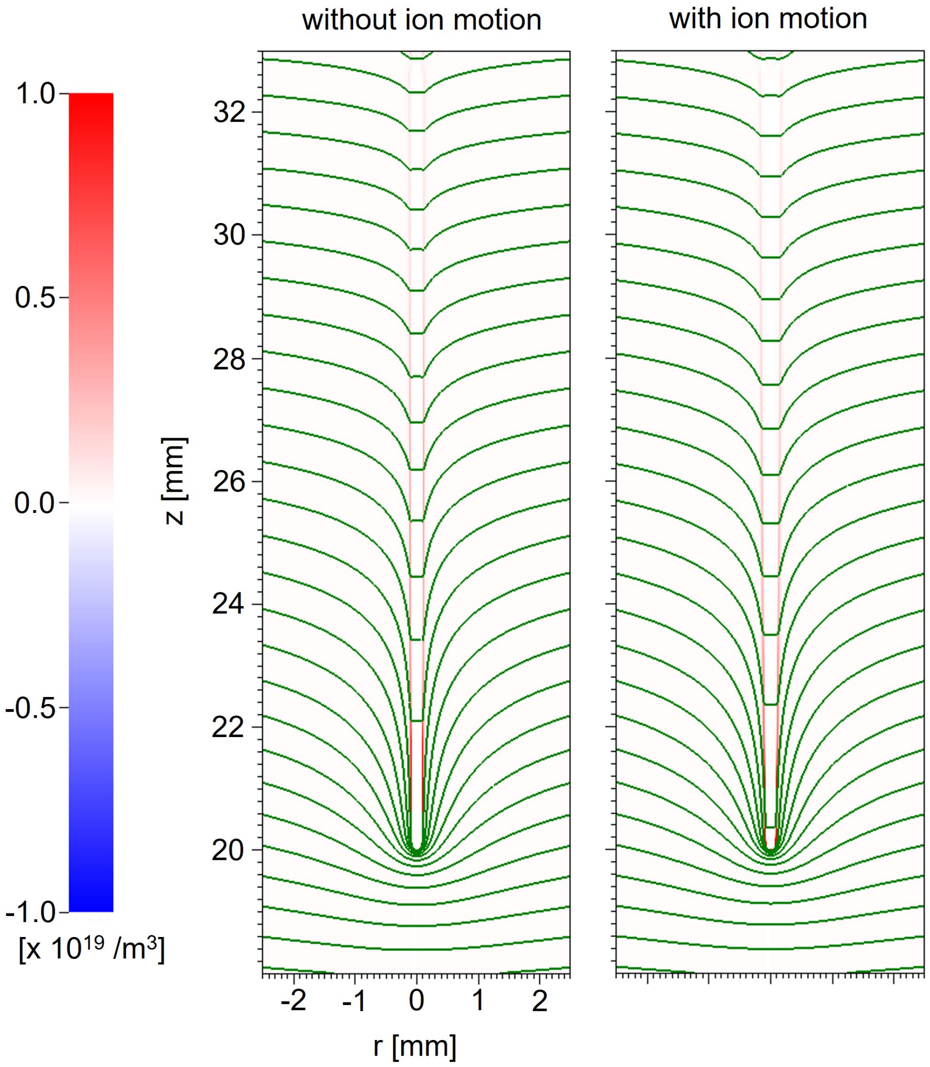

Figure 4.8: Charge density of the 4.65 kV/cm streamer without ion motion (left) and with ion motion (right), including green equipotential lines.

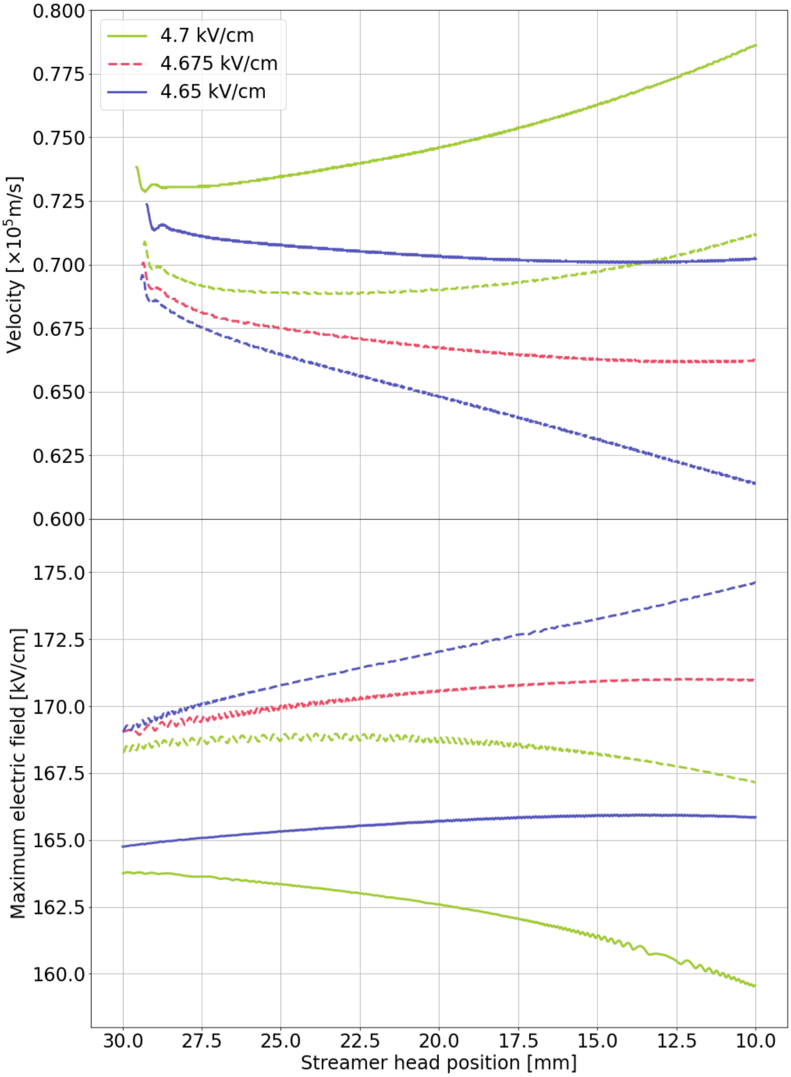

Figure 4.9: Velocity (top panel) and maximum electric field (bottom panel) of streamers against streamer head position for simulations with and without ion motion. Broken lines stand for simulations with ion motion. The legend on the top panel applies to the bottom panel as well.

4.4 Comparison with experiments

4.4.1 The stability field

Recently, the concept of the streamer stability field has been more commonly used in association with streamers propagating in inhomogeneous electric fields. It relates the maximum length a streamer could gain to the applied voltage [5, 6, 10, 126, 141]. An older definition used the term stability field to mean the homogeneous electric field in which a streamer would propagate in a stable manner - without changes in velocity and shape [44, 50, 114].

If we only consider the streamer channel length as the length behind the streamer head with substantial electron density, we observe the solitary streamer to have a constant length as it propagates. The solitary streamer has a uniform shape, and it follows, using the older definition of the stability field, that the solitary streamer is propagating in the stability field of STP dry air at 4.675 kV/cm. This value agrees with the measured stability field of 4 kV/cm in experiments [44, 50] for the original definition. With the newer definition, the stability field is reported to be between 4.5-5 kV/cm [6, 119].

4.4.2 Radius and velocity of solitary and minimal streamers.

In the pin-to-plate experiments of [21], it was found that after several branching events or in a quite weak field, streamers would approach a minimal diameter, and they were called minimal streamers. The solitary streamers are essentially the thinnest streamers that we found in our simulations as the stagnating streamers are not much thinner and hardly emit any light. Therefore we now compare their properties.

The simulated solitary streamer that includes ion motion has a radius of 55 μm, and this value is not far from the experimental findings in [96], which give 65 μm as the minimal streamer diameter in 1 bar air. The uniform velocity of our solitary streamer is 0.7×10^5 m/s, which falls in the range of the measured velocity of $(0.5 - 1) \times 10^5$ m/s of minimal streamers. Therefore we can conclude that the simulations match the experiments within 20%.

4.5 Conclusions and Outlook

We simulated single positive streamers in air at standard temperature and pressure in homogeneous background fields ranging from 4.5 kV/cm to 26 kV/cm in a 4 cm gap, and we came to the following conclusions:

1. The solitary streamer (or uniformly translating streamer) with dominant electron attachment and recombination behind the head lays a theoretical basis for the much used concept of a stability field. Streamers in higher fields increase in radius and velocity, while the solitary streamer transports a fixed amount of positive charge that is substantial only over a finite length.

2. The solitary streamer motion explains how a streamer can propagate over distances in meter length-scales though the conductivity of the back part of the channel disappearing due to attachment and recombination. The velocity of such a streamer can be an order of magnitude smaller than the electron drift velocity in its maximal electric field.

3. The value of the stability field of 4.675 kV/cm in our simulations in STP air agrees well experimentally measured values.

4. Minimal streamers are the thinnest and slowest streamers that have been experimentally observed [21]. Our values for the optical radius and velocity of solitary streamers agree well with measurements of these so-called minimal streamers. Even better agreement could possibly be found if for example humidity, repetition rate, and fluid model limitations were taken into account.

5. The solitary streamer causes negligible gas heating even after propagating for several hundreds of nanoseconds.

6. Ion motion plays a minor role for solitary streamers, but its effect increases as streamers slow down.

7. The maximal electric field at the streamer head is not a monotonic function of the background field, but it has a minimum for a background field of about 12 kV/cm. The implications of this on the electron energy distribution and on the optimization of the plasma chemistry will need to be investigated.

Future research could look into model reduction based on the solitary streamer, as it does not depend on time in a co-moving frame. How our current findings translate to other gases with different plasma-chemical reactions and photoionization rates also merits further investigation. There is an avenue for exploring the behavior of accelerating streamers on longer timescales, and the existence of the solitary positive streamer also raises the question of whether the solitary mode of propagation could also be observed in negative streamers. Finally, another open question is how and when solitary streamers form in background fields with a spatial gradient, as is common in experiments.

Chapter 5

Estimating the properties of single positive air streamers from measurable parameters

We develop an axial model for single steadily propagating positive streamers in air. It uses observable parameters to estimate quantities that are difficult to measure. More specifically, for given velocity, radius, length and applied background field, our model approximates the ionization degree, the maximal electric field, the channel electric field, and the width of the charge layer. These parameters determine the primary excitations of molecules and the internal currents. We do this by first analytically approximating the electron dynamics in different regions of a uniformly-translating streamer head, then we match the solutions between the different regions and finally we use conservation laws to determine unknown quantities. We find good agreement with numerical simulations for a range streamer lengths and background electric fields, even if they do not propagate in a steady manner. Therefore quantities that are difficult to access experimentally can be estimated from easily measurable quantities and our approximations. The theoretical approximations also form a stepping stone towards efficient axial multi-streamer models.

This chapter is available ahead of publishing as an electronic publication:
Dennis Bouwman, Hani Francisco, and Ute Ebert. Estimating the properties of single positive air streamers from measurable parameters. arXiv:2305.00842 [physics.plasm-ph], May 2023

The work featured in this chapter has been done in collaboration with Dennis Bouwman. DB was responsible for the theoretical aspects, which include the derivation of the analytical expressions, while HF worked on the numerical modeling. The chapter will also be part of the PhD thesis of DB.

5.1 Introduction

5.1.1 The challenge of model reduction

Streamer discharges occur widely in nature and technology [97]. The most commonly encountered and studied streamers appear in air and carry positive net charge at their heads. They are the topic of the present study.

The inner structure of a streamer consists of a thin moving space charge layer with strong field enhancement and steep electron density gradients at the tip. This is challenging to simulate numerically, even for a single axisymmetric streamer. On the other hand many discharge phenomena consist of numerous interacting streamers [33, 55, 62, 97, 133]. This poses a strong motivation to reduce the model while not giving up the physical basis and the model validation achieved in recent years [14, 34, 74, 146].

Streamer discharges consist of clearly distinguishable regions where different physical laws are dominating the behaviour: (i) a non-ionized outer area where the electrostatic Poisson equation has to be solved, (ii) the avalanche zone where photoionization creates many growing electron avalanches, (iii) the moving streamer heads with an active space charge layer where ionization increases rapidly and the field is highest, and (iv) ionized channels with charges and currents and dynamically changing conductivity. Different approximations are valid in different regions. We therefore analyse the regions separately. We will give analytic approximations for each of these regions. For the channel region an axial approximation has been formulated [81, 83], but for the streamer head the problem is open. Here we will analyze the different regions of the dynamics and concentrate on the heads. To allow for comparison between numerical simulations of the fluid model and analytical approximations, we constrain the analysis to single streamers in a uniform field and mostly to steady propagation.

5.1.2 Steady streamers as a test case

In sufficiently low electric fields a streamer can propagate at a constant velocity without changing shape [39, 40, 51, 75]. Such streamers leave no charge behind and their channel electric fields decay back to the applied background field. From now on we will refer to these as *steady*, because in a co-moving coordinate system such uniformly translating streamers are in a steady state. The properties of positive steady streamers can be considered extreme, with velocities as low as $3 \cdot 10^4$ m/s, electric fields enhanced to values as high as 222 kV/cm, steep gradients and a strongly curved thin charge layer [75].

The analysis presented in this work focuses heavily on steady streamers, since it is mathematically convenient to consider steady state solutions, as they have no explicit time dependence in a co-moving frame. Furthermore, we validate our approximations by comparing them to simulated results of a steady streamer. It must be noted that such a steady state approach could also be considered for accelerating streamers, since their properties typically change slowly with respect to other relevant time scales [110]. To that end we also compare our approximations to simulations of three accelerating streamers.

5.1.3 Earlier work

A classical challenge is to develop equations of motion where the head is characterized by a few numbers like radius R and velocity v. One of the first proposed analytic relations between R and v date back to 1965 [77] and an 'order-of-magnitude' model for the parameters of streamers was given in 1988 [36, 37]. A later experimental investigation proposed a data fit where the velocity depends on the radius squared, i.e. $v \sim R^2$ [22], and in [92] an approximate relation based on [77] was proposed where the velocity is also a function of the maximum electric field at the tip $E_{\max}$, i.e. $v = v(R, E_{\max})$. Other important theoretical results are: an approximation for the ionization degree [37, 73, 93], energy efficiency estimates for radical production [94], an analytic investigation of the avalanche zone dynamics [104], 1.5D models that require a prescribed radius [71, 110] and an estimate for charge layer width based on the notion of an effective ionization length [98]. An application of streamer theory is to infer difficult-to-measure properties from measurable parameters. For example, in [104] an analysis of the avalanche zone gives an approximate relation between R, $E_{\max}$ and the head potential. Another example is [12], where they estimate a parameter range for $E_{\max}$ on the basis of observed radius and velocity.

These theoretical results have improved our understanding of streamer dynamics and illustrated complex relations between different parameters. However, some ideas proposed in earlier works fail to agree with results from numerical simulations. At several instances throughout this work we will provide an in-depth evaluation of earlier work and propose improvements.

5.1.4 Content of the paper

In this work we develop semi-analytic approximations for the fluid model of single positive streamers that estimate difficult-to-measure quantities based on observable parameters. We will show how velocity v, radius of curvature R, length L and background field E_{bg} determine ionization degree $n_{i,\mathrm{ch}}$, charge layer width ℓ and the maximum and channel electric fields $E_{\max}$ and E_{ch}, respectively:

$$(v,\, R,\, L,\, E_{\mathrm{bg}}) \rightarrow (n_{i,\mathrm{ch}},\, \ell,\, E_{\max},\, E_{\mathrm{ch}}) \tag{5.1}$$

The derivation of our model starts by first defining different regions with specific physical mechanisms. Then we provide analytic approximations for each of these regions separately. Finally we perform matching of the regions and propose a self-consistent solution method. This results in a self-contained axial model which agrees well with numerical simulations. This means that our framework can complement experimental measurements when important streamer characteristics are difficult to measure precisely.

In section 5.2 we outline the classical fluid streamer model and the numerical implementation used for axisymmetric simulations. Furthermore, we discuss the results of numerical simulations in detail and introduce important definitions and conventions. In section 5.3 we integrate through the charge layer and obtain an analytic formula for the ionization degree. In section 5.4 we give an analysis of the electron avalanche dynamics in the region ahead of the streamer. In section 5.5 we explore the notion of the streamer head potential. In section 5.6 we describe our solution method and validate our approximations with numerical results of the fluid model.

5.2 Model description, definitions and conventions

In this section we will present the classical fluid model for positive streamers in air at standard temperature and pressure. We discuss the numerical implementation, used to obtain reference solutions in homogeneous background electric fields below the breakdown value. The same implementation was used in [39, 40] to study steady streamers. Furthermore, we will also give definitions of macroscopic parameters and clarify other conventions and terminology.

5.2.1 Description of the model

Basic equations.

We employ the classic fluid streamer model with local field approximation and without ion mobility. We only account for two charged species: the electron density n_e and the net ion density $n_i = n_+ - n_-$, with $n_\pm$ denoting the number density of all positive or negative ions. One can use just one ion density n_i instead of several ion species in regions where ion drift, electron detachment, and electron ion recombination can be neglected, as is the case in the streamer head. The electron density evolves according to a drift-diffusion-reaction equation while ions are considered immobile

$$\mathbf{q}t n_e = \nabla \cdot (\mu n_e \mathbf{E} + D \nabla n_e) + S_i + S_{ph}, \tag{5.2}$$

$$\mathbf{q}t n_i = S_i + S_{ph}, \tag{5.3}$$

with $\mathbf{E}$ the electric field, $\mu(E)$ the electron mobility, and $D(E)$ the electron diffusion coefficient. S_i and S_{ph} are the source terms for the effective impact ionization and photo-ionization respectively. As photo-ionization has an important nonlocal contribution in air, electron diffusion is typically negligible. Effective impact ionization is given by

$$S_i = |\mathbf{j}_e| \alpha_{\text{eff}}, \tag{5.4}$$

where $\mathbf{j}_e = -\mu n_e \mathbf{E}$ is the drift current density of electrons, $\mathbf{j} = -e\mathbf{j}_e$ is the electric current density, e is the elementary charge, and $\alpha_{\text{eff}}(E)$ is the effective ionization coefficient. The data for the transport and reaction coefficients are discussed in the next section. The photo-ionization source term in a volume V is given by

$$S_{ph}(\mathbf{r}) = \iiint_V \frac{I(\mathbf{r}')f(|\mathbf{r}-\mathbf{r}'|)}{4\pi|\mathbf{r}-\mathbf{r}'|^2} d^3r', \tag{5.5}$$

with $I(\mathbf{r}')$ the source of ionizing photons, $f(r)$ the absorption function and $4\pi|\mathbf{r}-\mathbf{r}'|^2$ is a geometric factor. Following Zheleznyak's model [102, 149], $I(\mathbf{r})$ can be expressed as

$$I(\mathbf{r}) = \frac{p_q}{p+p_q}\xi S_i(\mathbf{r}), \tag{5.6}$$

with p the actual pressure, $p_q = 40$ mbar the quenching pressure of the gas-mixture, and $\xi = 0.075$ a proportionality factor relating impact excitation to impact ionization S_i. The absorption function $f(r)$ is given by

$$f(r) = \frac{\exp(-\chi_{\text{min}} p_{O_2} r) - \exp(-\chi_{\text{max}} p_{O_2} r)}{r \ln(\chi_{\text{max}}/\chi_{\text{min}})}, \tag{5.7}$$

with $\chi_{\text{max}} = 150/$ (mm bar), $\chi_{\text{min}} = 2.6/$ (mm bar), and p_{O_2} is the partial pressure of oxygen. For air at 300 K and 1 bar, the corresponding absorption lengths are 33 μm and 1.9 mm.

The electric field follows from Poisson's equation for the electric potential ϕ

$$\epsilon_0 \nabla^2 \phi = -e n_q, \tag{5.8}$$

$$\mathbf{E} = -\nabla\phi, \tag{5.9}$$

with ϵ_0 the dielectric constant, e the elementary charge, and $n_q = n_i - n_e$ the charge number density.

Implementation of axisymmetric simulations.

In this work we compare our axial analytical approximations with the axisymmetric solutions of equations (5.3)-(5.9) obtained by numerical simulation. The numerical model uses the afivo-streamer code [136, 137]. The computational setup is the same as in earlier studies [39, 40] to which we refer for an in-depth discussion.

The transport and reaction coefficients are calculated by Bolsig+ [54] (version 12/2019) using cross sections from the Phelps database [1] under the assumption that the evolution of the electron density follows an exponential temporal growth or decay [147]. We use the same data for the analytical and the numerical models. Additionally, the numerical model for the axisymmetric simulations uses continuity equations for a number of species such as O_2^+, O_2^-, N_2^+, N_4^+, *etc.* as listed in [40]. This more extended plasma chemistry model helps stabilizing the steady streamer at the lowest background electric field, and it is consistent with the two-species model for n_e and n_i in the streamer head, as recalled above.

The photo-ionization integral in equation (5.5) is approximated by a set of Helmholtz differential equations with Bourdon's three-term approximation [19]. This approximation introduces small changes the photon absorption lengths. However, in [13, 147] it was shown this has essentially no measurable influence on streamer discharge propagation in air.

Computational domain.

The computational domain consists of a cylinder with 40 mm length and 20 mm radius, and planar electrodes on top and below. We impose cylindrical symmetry for domain and streamers; and we call the longitudinal coordinate ζ, and the radial coordinate r. An electric field is applied in the ζ-direction by fixing an electric potential difference between the electrodes. We use homogeneous Neumann boundary conditions for the potential in the r-direction, which means that the electric field is parallel to the lateral boundary. Homogeneous Neumann boundary conditions are also used for the electron density on all boundaries.

Initial conditions.

For the initiation of a streamer discharge, we placed two neutral seeds composed of electrons and positive ions at the upper boundary of the domain. The uppermost seed creates a region of field enhancement, and the seed below it supplies the initial electrons ahead of the forming streamer, before photo-ionization sets in. More details on the seeds — their densities, coordinates, and sizes — can be found in [39, 40].

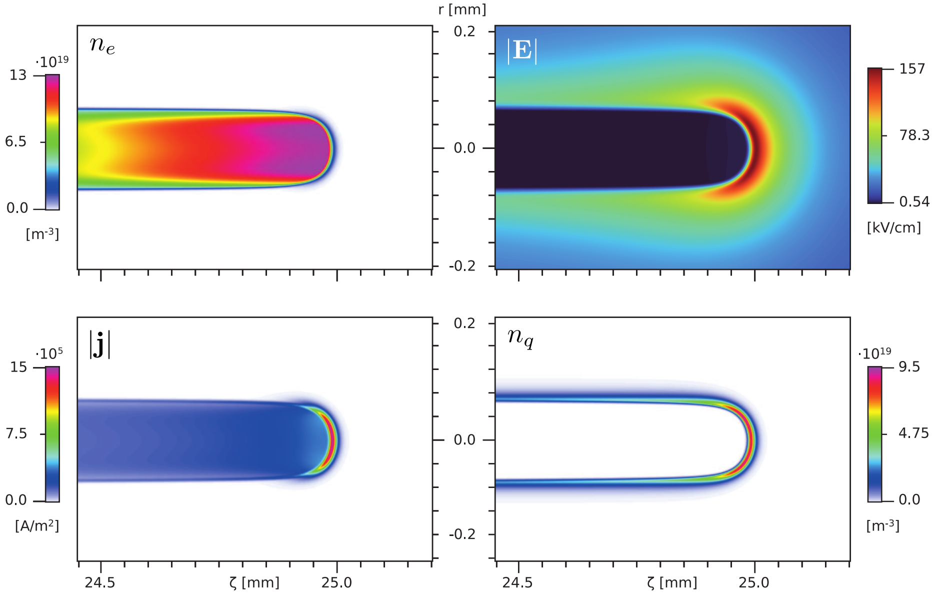

Figure 5.1: Electron density n_e, electric field strength $|\mathbf{E}|$, strength of the electric current density $|\mathbf{j}|$ and charge number density n_q of a steadily propagating streamer in a background field E_{bg} of 4.5 kV/cm. The figure zooms into the area around the streamer head.

In low electric fields, an initial transient electric field is needed to ensure the inception of a streamer discharge. In this research we will consider homogeneous background electric fields from 4.5 to 24 kV/cm, all below the breakdown value of 28 kV/cm. At 4.5 kV/cm, a streamer propagating at constant velocity and shape was obtained using the velocity control method [75]. At 10 kV/cm we adopt the same initial transient electric field as discussed in [40].

To accommodate for the relatively small size of the steady streamer during most of its propagation, we fixed the computational grid instead of employing adaptive mesh refinement in this simulation. From the axis of propagation up to 0.5 mm radially outwards, the grid cells were fixed to have a width of 1 μm. For the accelerating streamers, the mesh refinement routines are identical to those in [40].

5.2.2 Description of axisymmetric simulation results

The steady streamer in detail.

In this section we will discuss one of these simulations in detail, the steady streamer at a background electric field of 4.5 kV/cm. We recall that a steady streamer [39, 40, 51, 75] looses its conductivity at its back end due to electron attachment and electron ion recombination, that it leaves no electric charge behind, but carries a fixed amount of charge along, and that it propagates with constant velocity and shape. Figure 5.1 zooms into the front part of this streamer and shows four important quantities: the electron density n_e, the magnitude $|\mathbf{E}|$ of the electric field, the magnitude $|\mathbf{j}|$ of the electric current density and the charge number density n_q. From these quantities we can distinguish three regions with different dynamics:

1. *The channel* is the conductive interior of the streamer. We have a high electron density here and the plasma is quasi-neutral, $n_q \approx 0$. The electron density in the low axial electric field gives rise to an electric current flowing along the channel.

2. *The charge layer* is a layer of (positive) charge which surrounds and partially screens the channel. At the streamer head, the curvature of the charge layer leads to high electric field enhancement ahead of the front. In fact, we find the maximum electric field E_{max} here, with its location denoted by ζ_{tip}. As the electron density is high as well, we here have a high impact ionization rate and large currents resulting in the movement of the streamer head. The charge layer in the streamer head is also referred to as the ionization front. The width ℓ of the charge layer is much smaller than its radius R of curvature; this is required for the strong field enhancement ahead of the layer.

3. *The avalanche zone* of a positive streamer is the region ahead of the charge layer, so the electric charges in this region have a negligible effect on the electric field distribution. Without photo-ionization or some background electron density it could be neglected, but for positive streamers in air the photo-ionization creates many growing electron avalanches moving towards the charge layer. Close to the layer there is a high electric field, which means that a significant electron current is created which maintains the active ionization front.

Specifically in air without background ionization, the electron density vanishes with an asymptotic decay dictated by photon absorption [20]

$$\begin{aligned} n_e(\zeta) \propto \zeta^{-1} e^{-k\zeta} \text{ with } k = \chi_{\min} p_{\mathrm{O}_2}, \\ \text{for } \zeta \gg \zeta_{\mathrm{tip}}. \end{aligned} \tag{5.10}$$

Directions of currents and fields.

In figure 5.2 we zoom further into the ionization front and highlight important geometric features. We show the charge number density n_q and the magnitude of the electric current density $|\mathbf{j}|$ again in color-coding, but additionally we have visualized the direction of the current density by normalized arrows in the lower half of the plot, and the equipotential lines in the upper half of the plot. Note that in the avalanche zone the direction of the electron current $\mathbf{j}_e$ is radially inwards in a nearly spherical geometry, whereas in the channel the electron drift is homogeneously directed backwards parallel to the axis of propagation. Furthermore, the equipotential lines are very well aligned with the charge layer. This means that the electric current is essentially perpendicular to the layer in this region.

Streamers in different fields.

In figure 5.3 we show current densities, electric fields and electron and charge densities on the streamer axis, now not only for the steady streamer in the field of 4.5 kV/cm, but also for accelerating streamers in background fields of 14 and 24 kV/cm when the streamer heads reached $\zeta = 15$ mm. In more detail, the upper plots show the electric current density. The middle plots show the electric field (solid line) with our approximation (dashed line) of section 5.3.2, and the lower plots show n_e, n_i and n_q.

5.2.3 Definitions and conventions

In this paper we develop an axial model for the dynamics in charge layer and avalanche zone, based on analytical approximations. Here we introduce definitions and conventions for this purpose. A schematic is given in figure 5.5.

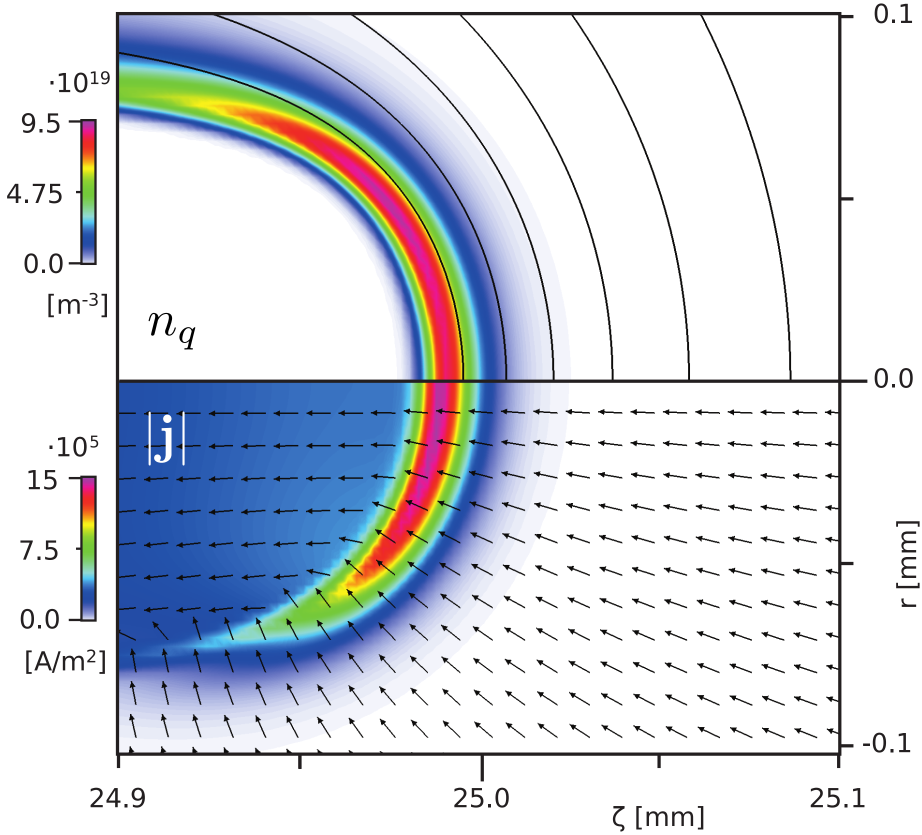

Figure 5.2: Charge number density n_q and magnitude of the electric current density $|\mathbf{j}|$ of the steady streamer in a field of 4.5 kV/cm in color-coding. In the upper half of the plot, equipotential lines are laid over the charge number density. In the lower half, the arrows show the normalized direction of the electron drift $\mathbf{j}_e = -\mathbf{j}/e$.

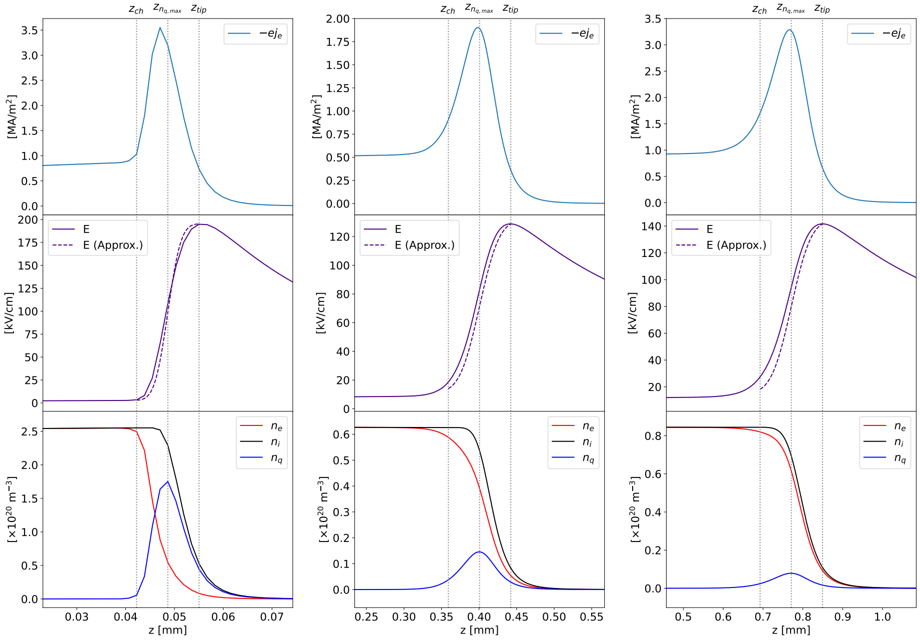

(a) 4.5 kV/cm (b) 14 kV/cm (c) 24 kV/cm

Figure 5.3: Current density, electric field and particle densities on axis for streamers in three background electric fields. All streamers are shown when the head has reached $\zeta_{\text{tip}} = 15$ mm. The origin of the coordinate system, $z = 0$, is at the centre of the hemisphere fitted through the maximum of the charge number density. The corresponding v and R are shown in figure 5.4.

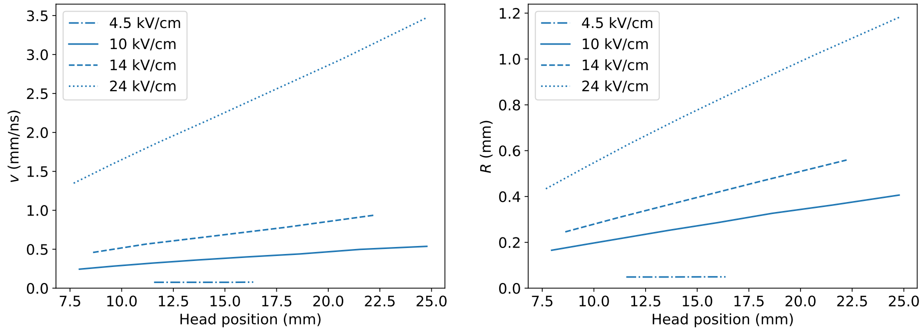

(a) Velocity (b) Radius of curvature

Figure 5.4: The velocity and radius as a function of the head position extracted from simulations at different background electric fields.

Parameterizing the charge layer.

We will characterize the charge layer by two maxima, namely the maximum of the electric field and the maximum of the charge number density. On the streamer axis we will denote them as ζ_{tip} and $\zeta_{n_{q,\max}}$, and their distance as $\tilde{\ell} = \zeta_{\text{tip}} - \zeta_{n_{q,\max}}$, or as

$$\tilde{\ell} = z_{\text{tip}} - z_{n_{q,\max}} \tag{5.11}$$

in the co-moving coordinate system (r, z) defined below. The two maxima are also illustrated in figure 5.3. There it is also shown that $z_{n_{q,\max}}$ is located roughly in the middle of the charge layer and that j is approximately symmetric in the vicinity of this maximum. Therefore we define the interior boundary z_{ch} of the charge layer as

$$z_{\text{ch}} = z_{\text{tip}} - \ell \text{ with } \ell = 2\tilde{\ell}. \tag{5.12}$$

Definition of velocity and co-moving coordinate system.

We define the streamer velocity v as the velocity of the maximal electric field at the streamer tip

$$v(t) = \frac{\mathrm{d}\zeta_{\text{tip}}(t)}{\mathrm{d}t}. \tag{5.13}$$

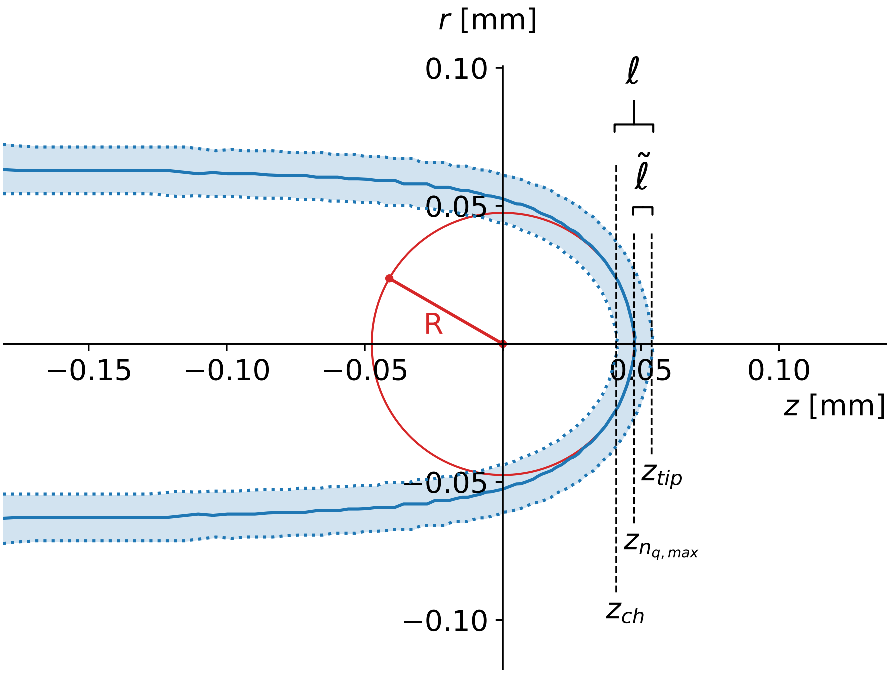

Figure 5.5: The charge layer within the co-moving coordinate system (r, z) at $E_{\mathrm{bg}} = 4.5$ kV/cm. The solid blue line represents the maximum of n_q (for each z) from numerical simulation and the shaded area is the corresponding charge layer parameterized using ℓ. Also shown are: the tangent circle with radius R, $\tilde{\ell}$ and the positions z_{ch}, z_{tip} and $z_{n_{q,\mathrm{max}}}$.

The velocity extracted from simulations is shown in figure 5.4a. We introduce a coordinate system (r, z) that moves into the ζ direction with velocity v. In particular, for a steady streamer (hence with constant velocity) the z coordinate can be written as

$$z = \zeta - vt. \tag{5.14}$$

Temporal derivatives transform to the new coordinate system as

$$\partial_t\big|_{\zeta} = \partial_t\big|_{z} - v\partial_z, \tag{5.15}$$

and for steady motion, we thus can replace

$$\partial_t\big|_{\zeta} \to -v\partial_z \tag{5.16}$$

in the co-moving frame (r, z).

Definition of radius and of origin of coordinate system.

We will characterize the streamer head by its radius of curvature R, defined as the radius of the circle which best approximates the curved charge layer at the streamer tip. This parameter is extracted from simulated data by fitting a semicircle through the maximum, for each z, of the charge layer, cf. figure 5.5. The extracted R is insensitive to fitting parameters provided the region is chosen sufficiently small. We therefore take this region to be $[z_{n_{q,\max}} - 4\tilde{\ell}, z_{n_{q,\max}}]$. The radius of curvature extracted from simulations is shown in figure 5.4b.

R is an important quantity because it determines the spatial decay of electric field and currents in the avalanche zone near the charge layer, as can be seen in figure 5.2. There the equipotential lines trace the shape of the charge layer sufficiently close to the axis of propagation. We choose the centre of the sphere as the origin of the co-moving coordinate system, $(r, z) = (0, 0)$, as shown in Fig. 5.5.

Definition of streamer length for steady streamers

The steady positive streamers reported in [39, 40, 75] are all 'detached' from their point of inception. By this we mean that due to attachment and recombination processes the channel looses its conductivity to the point that the streamer cannot be considered as connected to an electrode or initial ionized seed. For these detached streamers it is more useful to characterize streamer length with a typical length scale for the loss of conductivity L_{loss}

$$L_{\text{loss}} = v\tau, \tag{5.17}$$

with τ the electron loss time representing the collective timescale of all conductivity loss processes. The studies [40, 75] contain investigations of L_{loss} and τ. In particular, it is analyzed how these quantities depend on the gas-composition and the electric field.

5.3 The charge layer $(z_{\text{ch}} \leq z < z_{\text{tip}})$

In this section we formulate axial approximations for the total current density and for the electron and ion densities in the space charge layer, i.e., in the region between the front end z_{ch} of the channel and the maximum of the electric field z_{tip} (cf figure 5.5). The width ℓ of this region is much smaller than the radius of curvature R, therefore this layer can approximately be treated as planar.

We can neglect photo-ionization S_{ph} in the charge layer since it is much smaller than S_i. Photo-ionization only matters in the avalanche zone due to its nonlocality. We also neglect diffusion assuming there are no strong electron density gradients.

5.3.1 Current densities in the charge layer

Due to charge conservation and the Poisson equation of electrostatics, the total current density $\mathbf{j}_{\text{tot}}$ is a conserved quantity

$$\nabla \cdot \mathbf{j}_{\text{tot}} = 0, \text{ where } \mathbf{j}_{\text{tot}} = \mathbf{j} + \epsilon_0 \mathbf{q} t \mathbf{E}. \tag{5.18}$$

For steady motion in a co-moving frame z, the total current is $\mathbf{j}_{\text{tot}} = \mathbf{j} - v\epsilon_0 \mathbf{q} z \mathbf{E}$.

To solve for $\mathbf{j}_{\text{tot}}$ we approximate the charge layer at the tip as a planar surface. The validity of this approximation is governed by the dimensionless parameter ℓ/R. More specifically we require $\ell/R \ll 1$, which usually holds

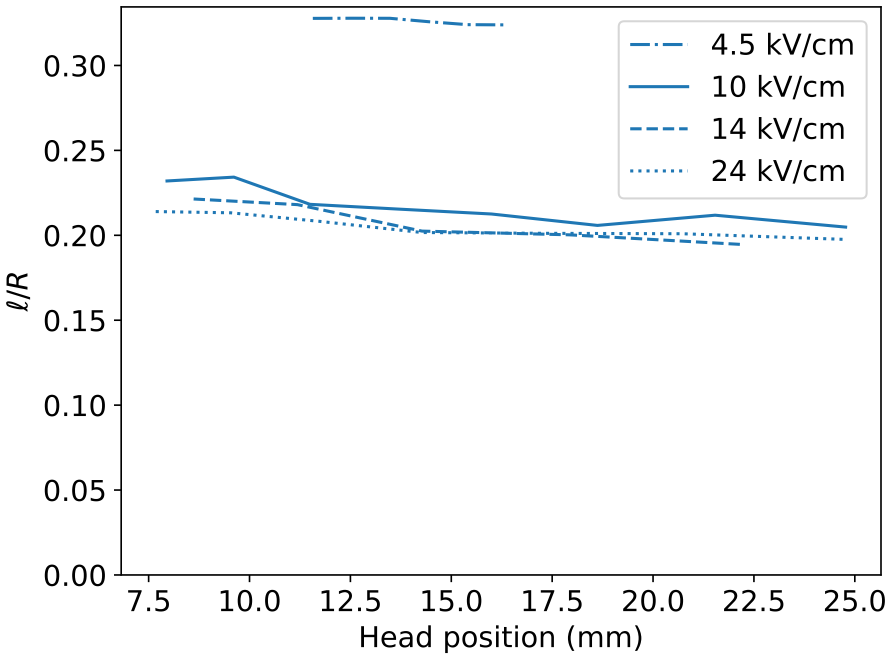

Figure 5.6: The dimensionless parameter ℓ/R as a function of the head position extracted from simulations at different background electric fields. This parameter characterizes the validity of the planar front approximation. The fluctuations observed are due to the small size of $\tilde{\ell}$ which is only a few times the smallest grid size.

for streamers as is shown in figure 5.6. In that case only the z-derivative of the divergence operator is non-vanishing. Then, equation (5.18) prescribes that $\mathbf{j}_{\text{tot}}$ is constant. With a boundary condition at z_{tip} this leads to the axial approximation

$$j_{\text{tot}}(z) = j_{\text{tot}}(z_{\text{tip}}). \tag{5.19}$$

Furthermore, the electric field is maximal at z_{tip}, hence $\mathbf{q}z\mathbf{E}|_{z_{\text{tip}}} = 0$ and the displacement current vanishes there

$$j_{\text{tot}}(z_{\text{tip}}) = -e j_{e,\text{tip}}, \tag{5.20}$$

where $j_{e,\text{tip}}$ is the electron current density on axis at z_{tip}. Similarly, the displacement current also vanishes approximately in the channel, where the electric field and electron density are nearly constant on-axis. This gives us

$$j_{e,\text{ch}} = j_{e,\text{tip}}, \tag{5.21}$$

where $j_{e,\text{ch}}$ is defined analogously as $j_{e,\text{tip}}$. Finally, combining this result with equation (5.19) determines $-j_{\text{tot}}/e = j_{e,\text{tip}} = j_{e,\text{ch}}$.

An analysis of the total current density at z_{ch} and z_{tip} was also proposed in [11]. They held that $j_{e,\text{tip}}$ vanishes which would mean that $j_{\text{tot}}(z_{\text{tip}})$ is completely determined by the displacement current $-v\epsilon_0\, \mathbf{q}z\mathbf{E}|_{z_{\text{tip}}}$. However, the numerical simulations in figure 5.3 contradict this. In fact, we observe that at z_{tip} the displacement current vanishes since the electric field is maximal and conversely that $j_{e,\text{tip}}$ does not vanish, which is in line with our reasoning.

5.3.2 Ionization and electric field in the charge layer

As ions are essentially immobile within the propagating streamer head, the degree of ionization is best determined by the ion density $n_{i,\text{ch}}$ behind the charge layer. An old approximation dating back to [37, 93] is

$$n_{i,\text{ch}}^{\text{old approx}} \approx \frac{\epsilon_0}{e} \int_0^{E_{\max}} \alpha_{\text{eff}}(E)\, dE, \tag{5.22}$$

where we use $E = |\mathbf{E}|$. In the appendix of [73] this equation is derived for planar negative streamer ionization fronts without electron diffusion

Table 5.1: The ionization degree $n_{i,\mathrm{ch}}$ ($\times 10^{19}$ m^{-3}) for streamers in different background fields. All streamers are taken at $\zeta_{\mathrm{tip}} = 15$ mm. We compare the old approximation (equation (5.22)) and our approximation (equation (5.26)) with our simulated results.

	classical eq. (5.22)	new eq. (5.26)	simulation
4.5 kV/cm	11.9	21.9	25.6
10 kV/cm	3.3	5.4	6.3
14 kV/cm	3.4	5.6	6.3
24 kV/cm	4.5	7.6	8.4

or photo-ionization. The approximation is easily derived from the two following equations: equations (5.3) and (5.4) together yield

$$\partial_t n_i = |\mathbf{j}_e| \alpha_{\mathrm{eff}}(E), \tag{5.23}$$

and equation (5.18) reads $\epsilon_0 \partial_t E = -e j_e$, if the total current ahead of the charge layer vanishes. This is the case, if the electron density ahead of the planar front vanishes, and if the electric field ahead of the front does not change in time.

According to [73], equation (5.22) is a good approximation of the numerical solutions of planar negative ionization fronts without photo-ionization in a time independent electric field; the error is only 5 to 10%. However, in simulations of positive curved streamer fronts with photo-ionization as shown in [75, 78], the ionization degree is about twice as high as given by the classical approximation (5.22) (in particular, see table B1 of [75]). In table 5.1 we make a similar comparison and confirm the discrepancy of equation (5.22) as an approximation of the ionization degree of positive streamers.

A first hypothesis was that the approximation (5.22) only covers the part of the front where the electric field decays from its maximal value $E_{\max}$ to a low value inside the channel, and that it misses the avalanche zone ahead of the charge layer where the electric field increases to its maximum [78]. This avalanche zone is essentially absent without background ionization and photo-ionization, but very present in air. However, the ionization created in the avalanche zone contributes relatively little ionization.

We discuss this later in more detail in section 5.6.2 and figure 5.8.

We will now show that the total current density $\mathbf{j}_{\mathrm{tot}}$ from the avalanche zone into the curved charge layer contributes significantly to the ionization behind the front for positive streamers in air. The derivation of the new approximation is analogous to the earlier one in [73]. We start from (5.23) and substitute j_e by the total current to get

$$\mathbf{q}t n_i = \frac{1}{e}\Big|\mathbf{j}_{\mathrm{tot}} - \epsilon_0 \mathbf{q}t\mathbf{E}\Big|\alpha_{\mathrm{eff}}. \tag{5.24}$$

This can be further simplified due for steady motion and because the vectors $\mathbf{j}_{\mathrm{tot}}$ and $\mathbf{E}$ are parallel on the axis

$$\mathbf{q}z n_i = \left(\frac{\epsilon_0}{e}\mathbf{q}zE + \frac{j_{\mathrm{tot}}}{ev}\right)\alpha_{\mathrm{eff}}. \tag{5.25}$$

Integration through the ionization front gives

$$\begin{aligned} n_i(z) = n_{i,\mathrm{tip}} + \frac{\epsilon_0}{e}\int_{E(z)}^{E_{\max}} \alpha_{\mathrm{eff}}(E)\,dE \\ + \frac{1}{ev}\int_{z}^{z_{\mathrm{tip}}} \alpha_{\mathrm{eff}}(E(z)) j_{\mathrm{tot}}\,dz. \end{aligned} \tag{5.26}$$

The first term is obtained after integration by substitution ($\partial_z E\,dz = dE$). It reproduces the old approximation (5.22) when it is evaluated at $z = z_{\mathrm{ch}}$ and when $E(z_{\mathrm{ch}})$ is approximated as vanishing. The second term requires further analysis. We approximate j_{tot} by the constant $-ej_{e,\mathrm{tip}}$ according to equation (5.19). Furthermore, we need the spatial profile of $E(z)$ to evaluate $\alpha_{\mathrm{eff}}(E(z))$ under the integral. Here we adopt a heuristic parametrization of E and leave further analysis to future work. In figure 5.3 we see that within the layer the charge number densities n_q have an approximately Gaussian profile that can be parameterized as

$$n_q(z) = \frac{N_q}{\sigma\sqrt{2\pi}}\exp\left(-\frac{1}{2}\left(\frac{z-R}{\sigma}\right)^2\right), \tag{5.27}$$

where

$$N_q = \int_{z_{\mathrm{ch}}}^{z_{\mathrm{tip}}} n_q\,dz = \frac{\epsilon_0}{e}\,(E_{\max} - E_{\mathrm{ch}}), \tag{5.28}$$

is the charge number density integrated from the channel to the maximum of the electric field.

Next, we use that over its small width the layer is only weakly curved, and we use a planar approximation $\partial_z E = en_q/\epsilon_0$ to calculate the electric field as $E(z)$ by integrating over n_q

$$E(z) = E_{\max} - \frac{e}{\epsilon_0}\int_{z}^{z_{\text{tip}}} n_q(z)dz. \tag{5.29}$$

This heuristic parametrization of the electric field is shown in the middle panels of figure 5.3 together with the results of the axisymmetric simulations. The parametrizations of E are in agreement with the simulated results when we choose $\sigma = \tilde{\ell}/3$ for the steady streamer and $\sigma = \tilde{\ell}/2$ for the accelerating ones. Furthermore, we remark explicitly that equation (5.27) is only used to motivate and evaluate the parameterization for E in equation (5.29).

Using equation (5.29) as an approximation for the electric field within the charge layer, we can calculate the ionization degree by evaluating equation (5.26) at z_{ch}. In table 5.1 we compare this approximation, when all macroscopic parameters are extracted from simulations. We observe good agreement, with relative errors between 10-15%.

5.3.3 Electron density in the charge layer

Our derivation of the electron density within the charge layer starts from the fundamental equation of charge conservation

$$e\mathbf{q}tn_q = -\nabla \cdot \mathbf{j}. \tag{5.30}$$

Since we have uniform translation and a planar front we can write

$$vn_q = j_{e,\text{ch}} - j_e, \tag{5.31}$$

where $j_{e,\text{ch}}$ has been introduced as an integration constant. As a side note, a similar relation has also been proposed in [12, 93], but there the integration constant has been explicitly neglected. However, in figure 5.3 we see that $j_{e,\text{ch}}$ and $j_{e,\text{tip}}$ are significant. Continuing our derivation, we use

$n_q = n_i - n_e$ and rearrange the terms in this equation such that we find an expression for the electron density profile in the charge layer

$$n_e(z) = \frac{v n_i(z) - j_{e,\mathrm{ch}}}{v + v_{\mathrm{dr}}}, \tag{5.32}$$

with the charge drift velocity $v_{\mathrm{dr}} = \mu E$. (Note that electrons drift with $-v_{\mathrm{dr}}$). This determines $n_e(z)$ since $n_i(z)$ is given by equation (5.26). By evaluating this expression at z_{ch} or z_{tip} and using equation (5.21) we find quasi-neutrality: $n_{e,\mathrm{ch}} = n_{i,\mathrm{ch}}$ and $n_{e,\mathrm{tip}} \approx n_{i,\mathrm{tip}}$. Note that the implied quasi-neutrality at z_{tip} only holds as an approximation, see figure 5.3.

Moreover, integration of equation (5.31) through the charge layer and using (5.28) results in

$$\int_{z_{\mathrm{ch}}}^{z_{\mathrm{tip}}} e(j_{e,\mathrm{tip}} - j_e)\, dz = v\epsilon_0(E_{\mathrm{max}} - E_{\mathrm{ch}}). \tag{5.33}$$

This can be interpreted as a physical connection between the movement of a positive charge layer (represented by a discontinuity in the electric field) and the separation of charge. The latter can be directly expressed by the electric current integrated through the charge layer.

5.4 The avalanche zone ($z \geq z_{\mathrm{tip}}$)

The avalanche zone is defined as the region ahead of the space charge layer where space charges can be neglected, and where the electric field is above the breakdown value. This means that the electric field near this layer is dominated by the electric charges in the layer, and that charges in the avalanche zone move in this externally determined field, but do not contribute to it.

In the avalanche zone, different approximations have to be made than in the charge layer:

(i) As said above, the influence of the local charges on the electric field is negligible, $\nabla \cdot \mathbf{E} = 0$, so the avalanche develops in an externally determined electric field.

(ii) The dynamics inside the charge layer were described using the planar front approximation because $\ell \ll R$, but the planar front approximation is not valid in the avalanche zone. We therefore do account for the curvature of the charge layer in the avalanche zone. We do so by approximating the charge layer at the streamer tip as a hemisphere with a radius R, see figures 5.5 and 5.7.

(iii) Electron diffusion can still be neglected, because photoionization prevents the growth of steep gradients, but photoionization now needs to be included. Although the impact ionization is much stronger than the photoionization, the non-locality of the photoionization is essential to create seed electrons in the avalanche zone.

5.4.1 Equation for electron density in the avalanche zone

The drift-diffusion-reaction equation (5.2) for the electron dynamics on the axis of the avalanche zone can be simplified as follows. First we remark that with the approximations above and with the chain-rule we can write on the axis

$$\begin{aligned} \nabla \cdot (\mu n_e \mathbf{E}) &= \mathbf{E} \cdot \nabla(\mu n_e) + \mu n_e \nabla \cdot \mathbf{E}, \\ &= E \mathbf{q}z(\mu n_e), \\ &= v_{\mathrm{dr}} \mathbf{q}z n_e + \frac{\mathbf{q}z\mu}{\mu} v_{\mathrm{dr}} n_e, \end{aligned} \tag{5.34}$$

The electron dynamics of equation (5.2) then becomes, in the comoving frame on the axis,

$$(v + v_{\mathrm{dr}})\mathbf{q}z n_e + \frac{\mathbf{q}z\mu}{\mu} v_{\mathrm{dr}} n_e + S_i + S_{ph} = 0. \tag{5.35}$$

In the next section we derive an expression for S_{ph}.

5.4.2 Coupling between avalanche zone and charge layer

The dynamics in the avalanche zone are coupled to the other discharge regions. More precisely, the charge layer together with the channel generate the enhanced electric field in the avalanche zone, and the charge layer also emits the large majority of photons that generate photoionization and initiate the ionization avalanches in the avalanche zone.

The electric field near the charge layer and near the streamer axis are approximated by a uniformly charged sphere

$$E(z) = \frac{z_{\text{tip}}^2 (E_{\text{max}} - E_{\text{bg}})}{z^2} + E_{\text{bg}}, \tag{5.36}$$

as argued above.

For photoionization in air, the photons are mainly produced in the charge layer, because the majority of high-energy collisions occurs here, as will be shown in figure 5.8. Photons originating from the avalanche zone are therefore neglected. Moreover, since typical absorption lengths ($33-1900$ μm for dry air at 1 bar and 300 K) are large compared to ℓ, cf figure 5.9, we can essentially treat the charge layer as a surface. Accordingly, we approximate equation (5.5) by a surface integral

$$S_{ph}(z) = \iint_S \frac{I(\mathbf{r}') f(|z\mathbf{e}_z - \mathbf{r}'|)}{4\pi |z\mathbf{e}_z - \mathbf{r}'|^2} d^2 r', \tag{5.37}$$

with $\mathbf{e}_z$ the unit vector in the z-direction, and the coordinates $\mathbf{r}'$ now lie on the surface S. For simplicity, we take S to be the surface of a hemisphere with radius R centered at $z = 0$. This is illustrated in figure 5.7.

The general photon source term from equation (5.6) is now written as

$$I(\mathbf{r}') = \mathcal{A}(\mathbf{r}') I^*, \tag{5.38}$$

with I^* the surface density of photon production

$$I^* = \frac{p_q}{p + p_q} \xi v n_{i,\text{ch}} \tag{5.39}$$

on the streamer axis. Here $p_q/(p+p_q)$ is the quenching factor of the photon emitting state. The excitation of the photon emitting state is approximated as impact ionization S_i times a proportionality factor ξ. Note that the impact ionization has to be integrated over the width of the charge layer $\int S_i \, dz = v(n_{i,\text{ch}} - n_{i,\text{tip}})$ which is obtained after integrating $-v\partial_z n_i = S_i$ (from equation (5.3)) across the charge layer. Finally, since $n_{i,\text{tip}} \ll n_{i,\text{ch}}$ we have omitted the dependency on $n_{i,\text{tip}}$.

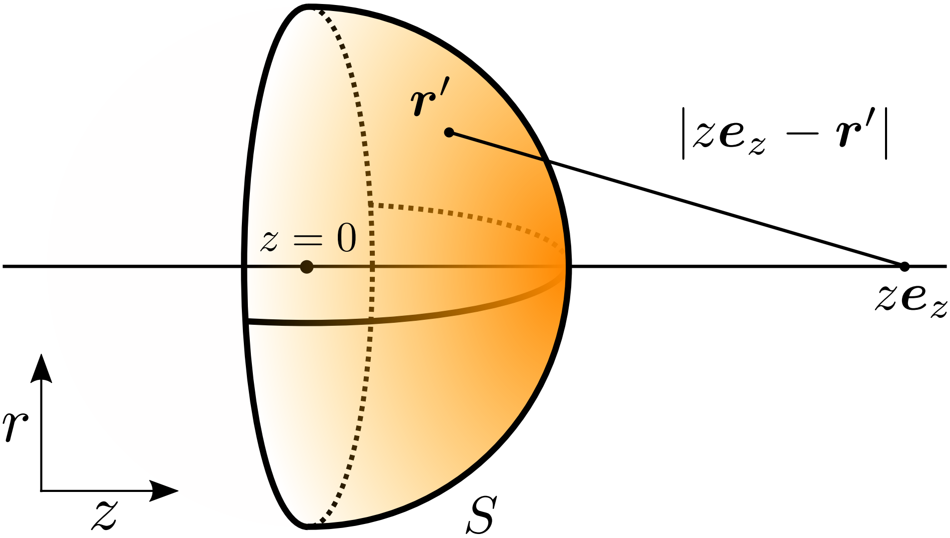

Figure 5.7: The configuration used for computing the photo-ionization source term. The charge layer is approximated by a hemisphere S with radius R centered around $z = 0$. The color indicates that in reality the front is not radiating with uniform intensity but fades at the edges (even though we do not account for this here). Also shown is the path of a photon produced at $\mathbf{r}'$ and absorbed at $z\mathbf{e}_z$. Photoionization then creates electron avalanches that develop the local electric field. We use the avalanches on the z-axis for our approximations.

$\mathcal{A}(\mathbf{r}')$ is a function that can account for the fact that the impact ionization and thus the photon radiation in the charge layer diminishes in the off-axis direction. However, for simplicity we take $\mathcal{A}(\mathbf{r}') = 1$. Naturally this will slightly overestimate photon radiation.

5.4.3 Solving the electron density in the avalanche zone

We will now solve equation (5.35). To do so we first introduce the short hand notation

$$\mathbf{q}z n_e + \lambda(z) n_e = -K(z), \tag{5.40}$$

with $\lambda(z)$ the electron avalanche growth function

$$\lambda(z) = \frac{v_{\mathrm{dr}}(E(z))}{v + v_{\mathrm{dr}}(E(z))} \left(\alpha_{\mathrm{eff}}(E(z)) + \frac{\mathbf{q}z\mu}{\mu} \right), \tag{5.41}$$

and $K(z)$ the photoelectron source term

$$K(z) = \frac{S_{ph}(z)}{v + v_{\mathrm{dr}}(E(z))}, \tag{5.42}$$

in the external electric field $E(z)$ from equation (5.36). $S_{ph}(z)$ is determined by equations (5.37) – (5.39) as a surface-integral corresponding to the parametrized charge layer. For given I^*, equation (5.40) is an ordinary differential equation for n_e that is solved as

$$n_e(z) = \int_z^\infty K(y)\, e^{\int_z^y \lambda(x)\, dx}\, dy. \tag{5.43}$$

This solution can be interpreted as a superposition of electron avalanches. The electron avalanches are continuously created by a photoelectron density K. The avalanches grow in the electric field as described by λ which contains the effects of impact ionization α_{eff} and of electron mobility $\mu(E)$.

For further evaluation, it is interesting to discuss the structure of this solution and the implications for the electron and ion densities at the front and back end of the charge layer, z_{tip} and z_{ch}. We find that equation (5.43) can be rewritten as

$$\frac{n_{e,\mathrm{tip}}}{n_{i,\mathrm{ch}}} = F(v, R, E_{\mathrm{max}}, E_{\mathrm{bg}}), \tag{5.44}$$

with an explicit equation for the function F that does not depend on any electron or ion densities. Here R, E_{max} and E_{bg} determine the electric field $E(z)$ in the avalanche zone according to (5.36). That F does not depend on the particle densities, is due to the linear nature of the avalanche zone without local space charge effects: twice as many photons emitted from the charge layer will create twice as many avalanches and twice as many electrons arriving at z_{tip} which in turn emit twice as many photons from the charge layer.

The explicit equation for the function F is

$$F = \frac{p_q}{p+p_q}\,\xi \int_{z_{\mathrm{tip}}}^{\infty} dy\,\frac{v}{v+v_{\mathrm{dr}}(y)}\; e^{\int_{z_{\mathrm{tip}}}^{y}\lambda(x)\,dx} \cdot \iint_S d^2r'\,\mathcal{A}(\mathbf{r}')\,\frac{f(|y\mathbf{e}_z-\mathbf{r}'|)}{4\pi|y\mathbf{e}_z-\mathbf{r}'|^2}, \qquad (5.45)$$

where the first line contains the field dependent electron dynamics on the streamer axis, and the second line the field independent photon dynamics between the charge layer and the axis.

An analysis of the avalanche zone along similar lines was proposed in [104], but they only account for photons produced in the avalanche zone and neglect the contribution from the charge layer. However figure 5.3 shows that ionization in the charge layer, and therefore the associated photon production, is far more important. In our approach we do take the charge layer as the dominant photon source. The same reasoning was also given in [71, 110]. In addition to this we have derived an improved photoionization balance on the basis of consistent electrodynamics in the charge layer and avalanche zone, equation (5.44). This formula replaces the photoionization balance proposed in [104]. We finally remark that the balance between the dynamics of photons and of electron avalanches resembles a self-sustained DC discharge, with the difference that the anode is replaced by a propagating streamer head with self-consistent shape.

5.5 The electrostatic field and the head potential

5.5.1 Streamer head potential

As recalled in [97], the electrostatic approximation for the electric field $\mathbf{E} = -\nabla\varphi$ is sufficient for streamer physics. Therefore the line integral between any two points is independent of the path taken between them

$$\int_{\mathcal{C}} \mathbf{E} \cdot dl = \phi(\mathbf{r}) - \phi(\mathbf{r}'), \tag{5.46}$$

with $\mathcal{C}$ any continuous curve which starts at $\mathbf{r}$ and ends at $\mathbf{r}'$. This concept will be applied to derive a relation between the electrostatic properties of the channel and the head.

We shall use equation (5.46) to solve two path-integrals, the first corresponding only to the background field and the second to the field with a streamer present. In both cases $\mathcal{C}$ equals the axis of propagation, i.e. ζ-axis, which gives $\mathbf{r} = 0$ and $\mathbf{r}'$ on the opposing electrode. For the streamers in this work ζ_{tip} is far away from the opposing electrode, which means that boundary effects are negligible and we can take $\mathbf{r}'$ at infinity. When we subtract the two integrals we find

$$\int_0^\infty \left(E(\zeta) - E_{\text{bg}}\right) d\zeta = 0, \tag{5.47}$$

since the potential at $\mathbf{r}$ and $\mathbf{r}'$ is the same and therefore the right-hand side vanishes. This fundamental property has been considered by previous authors [51, 68, 75, 104, 132]. Equation (5.47) will be split in two intervals with different dynamics, namely: the streamer channel $[0, \zeta_{\text{tip}}]$ and the avalanche zone $[\zeta_{\text{tip}}, \infty)$. We shall treat each of these intervals separately.

Potential across the channel.

The potential across the channel requires different treatment for steady and accelerating streamers.

For a steady streamer the channel electric field decays back to the background field. In general the profile of the channel electric field is determined by currents in the streamer channel [81, 83]. For now, modelling the charge distribution within the channel is not considered. Instead, we suggest a plausible channel electric field profile for steady streamers. In section 5.2.3 we have discussed how dynamics in the channel are related to an electron loss time scale τ, which in turn defines an electron loss length L_{loss}. We use these concepts to impose

$$\begin{aligned} E(\zeta) = E_{\text{bg}} + (E_{\text{ch}} - E_{\text{bg}}) \exp\left(\frac{\zeta - \zeta_{\text{ch}}}{L_{\text{loss}}}\right), \\ \text{for } \zeta < \zeta_{\text{ch}}. \end{aligned} \tag{5.48}$$

Substituting this into equation (5.47) results in

$$\int_0^{\zeta_{\text{ch}}} \left(E(\zeta) - E_{\text{bg}}\right) d\zeta = L_{\text{loss}} \left(E_{\text{bg}} - E_{\text{ch}}\right). \tag{5.49}$$

For the accelerating streamers considered in this work we have $L \ll L_{\text{loss}}$, which means it is more reasonable to work with an averaged channel electric field $\bar{E}_{\text{ch}}$. By holding that $E_{\text{ch}} = \bar{E}_{\text{ch}}$ over the length of the channel we can obtain a similar result

$$\int_0^{\zeta_{\text{ch}}} \left(E(\zeta) - E_{\text{bg}}\right) d\zeta = L \left(E_{\text{bg}} - \bar{E}_{\text{ch}}\right). \tag{5.50}$$

Potential across the avalanche zone.

In the avalanche zone the electric field was approximated by that of a uniformly charged sphere, equation (5.36). Using this the potential across the avalanche zone simplifies approximately to

$$\int_{\zeta_{\text{tip}}}^{\infty} \left(E(\zeta) - E_{\text{bg}}\right) d\zeta = R(E_{\text{max}} - E_{\text{bg}}). \tag{5.51}$$

This gives the final result

$$R(E_{\text{max}} - E_{\text{bg}}) = L \left(E_{\text{bg}} - E_{\text{ch}}\right). \tag{5.52}$$

To keep notation simple we have no longer discerned between L_{loss} or $\bar{E}_{\text{ch}}$ for the separate cases of steady and accelerating streamers.

5.6 Solving the approximations

5.6.1 Solution method

We now assume that velocity v, radius of curvature R, length L and background electric field E_{bg} are given, for example by experimental measurements, and we estimate four unknowns that are much more difficult to measure: ionization degree $n_{i,\mathrm{ch}}$, maximal electric field $E_{\max}$, channel field E_{ch}, and charge layer width ℓ. To that end we shall formulate a system of four relations from which these unknowns will be determined.

In the previous sections we have derived equations (5.21) and (5.33) by analyzing the dynamics of the charge layer $z_{\mathrm{ch}} \leq z < z_{\mathrm{tip}}$, where $z_{\mathrm{tip,ch}} = R \pm \ell/2$. These are the first and second relations. On the basis of electrostatics we have related the head potential to the streamer length in equation (5.52), which is the third relation. Finally, we require that charge layer and avalanche zone electron dynamics are consistent (cf. section 5.4.3). This introduces the last relation, namely equation (5.44). For convenience, we repeat our relations here

$$
\begin{aligned}
j_{e,\mathrm{ch}} &= j_{e,\mathrm{tip}}, && (5.53)\\
v\epsilon_0(E_{\max} - E_{\mathrm{ch}}) &= \int_{z_{\mathrm{ch}}}^{z_{\mathrm{tip}}} e(j_{e,\mathrm{tip}} - j_e)\,dz, && (5.54)\\
R(E_{\max} - E_{\mathrm{bg}}) &= L\left(E_{\mathrm{bg}} - E_{\mathrm{ch}}\right), && (5.55)\\
\frac{n_{e,\mathrm{tip}}}{n_{i,\mathrm{ch}}} &= F(v, R, E_{\max}, E_{\mathrm{bg}}). && (5.56)
\end{aligned}
$$

The function F is defined in equation (5.45) and the electron current density is defined as $j_e = -\mu n_e E$. The above system of equations has 8 independent parameters:

$$v,\ R,\ L,\ E_{\mathrm{bg}},\ n_{i,ch},\ E_{\max},\ E_{\mathrm{ch}} \text{ and } \ell. \qquad (5.57)$$

All other quantities are determined by these 8 parameters. To see this, we summarize our approximations in the two regions:

- In the avalanche zone ($z \geq z_{\mathrm{tip}}$) the electric field and the electron density are approximated by (equations (5.36) and (5.43))

$$E(z) = \frac{z_{\text{tip}}^2 (E_{\max} - E_{\text{bg}})}{z^2} + E_{\text{bg}}, \tag{5.58}$$

$$n_e(z) = \int_z^{\infty} K(y)\, e^{\int_z^y \lambda(x)\, dx}\, dy, \tag{5.59}$$

$$\text{for } z \geq z_{\text{tip}}.$$

Notably, the function $K(y)$ (equation (5.42)) accounts for the production of photoelectrons and is proportional to $n_{i,ch}$. The electron density and the electric field by definition give j_e and therefore $j_{e,\text{tip}}$. Finally, we have assumed that space charge effects are negligible in the entire avalanche zone. We therefore also assume quasi-neutrality at the tip $n_{i,\text{tip}} \approx n_{e,\text{tip}}$.

- In the charge layer ($z_{\text{ch}} \leq z < z_{\text{tip}}$) the electric field and densities are approximated by (equations (5.29), (5.26), (5.32))

$$E(z) = E_{\max} - \frac{e}{\epsilon_0} \int_z^{z_{\text{tip}}} n_q(z) dz, \tag{5.60}$$

$$n_i(z) = n_{i,\text{tip}} + \frac{\epsilon_0}{e} \int_{E(z)}^{E_{\max}} \alpha_{\text{eff}}(E)\, dE, \\ + \frac{1}{ev} \int_z^{z_{\text{tip}}} \alpha_{\text{eff}}(E(z)) j_{\text{tot}}\, dz, \tag{5.61}$$

$$n_e(z) = \frac{v n_i(z) - j_{e,\text{ch}}}{v + v_{\text{dr}}}, \tag{5.62}$$

$$\text{for } z_{\text{ch}} \leq z < z_{\text{tip}},$$

where n_q in equation (5.60) is a parametrization given in equation (5.27). The quantities $n_{i,\text{tip}}$ and $j_{e,\text{tip}}$ are determined by the avalanche zone. Quasi-neutrality in the channel gives $n_{i,\text{ch}} = n_{e,\text{ch}}$. Thus we can evaluate j_{tot} and j_e within the charge layer.

The objective is then to determine 4 parameters in (5.57), since we consider that (v, R, L, E_{bg}) are fixed by observations. The remaining four, which we call $m = (n_{i,\text{ch}}, E_{\max}, E_{\text{ch}}, \ell)$, have to satisfy our relations (5.53)-(5.56). Solving this system of equations is equivalent to finding the roots of the four-dimensional vector-function $\mathcal{S}$, which is defined as the difference between the left- and right-hand sides of equations (5.53)-(5.56). Thus m is a consistent solution if it satisfies

$$\mathcal{S}(m) = 0. \tag{5.63}$$

Due to the complexity of $\mathcal{S}$ we employ an iterative root-finding algorithm that solves equation (5.63). Such an algorithm starts from an initial guess m^0 and produces a sequence of values m^k that converges to the root. We emphasize again that the input parameters v, R, L and E_{bg} in addition to m^k are sufficient to evaluate $\mathcal{S}(m^k)$.

5.6.2 Results

Steady streamer:

In this section we will compare the approximated $n_e(z)$, $n_{i,\mathrm{ch}}$, E_{max}, E_{ch} and $\tilde{\ell}$ with numerical simulations. We shall first do this comparison for the steady streamer. To obtain these results we extracted $E_{\mathrm{bg}} = 4.5$ kV/cm, $v = 0.076$ mm/ns, $R = 49$ μm and $L_{\mathrm{loss}} = 3.8$ mm from simulation (see figure (5.4)) and used these to solve equation (5.63).

In figure 5.8 we show our approximation for the axial electron density of the steady streamer (equations (5.32) and (5.43)). The approximated electron density was overlaid onto the results from the numerical simulation such that the respective z_{tip} overlap. We observe that our analytic formulae for the electron density profile in the avalanche zone reproduces the profile obtained from simulation well. In this figure we can also observe that more than 95% of the ionization occurs in the charge layer. This underlines our earlier arguments that ionization predominantly occurs in the charge layer and that photons originating from the avalanche zone can be neglected.

The approximated parameters $n_{i,\mathrm{ch}}$, E_{max}, E_{ch} and $\tilde{\ell}$ that were derived in this evaluation are shown in figure 5.9. We observe good agreement with a maximum relative error of about 30% for the prediction of $\tilde{\ell}$. The other parameters agree within 25%.

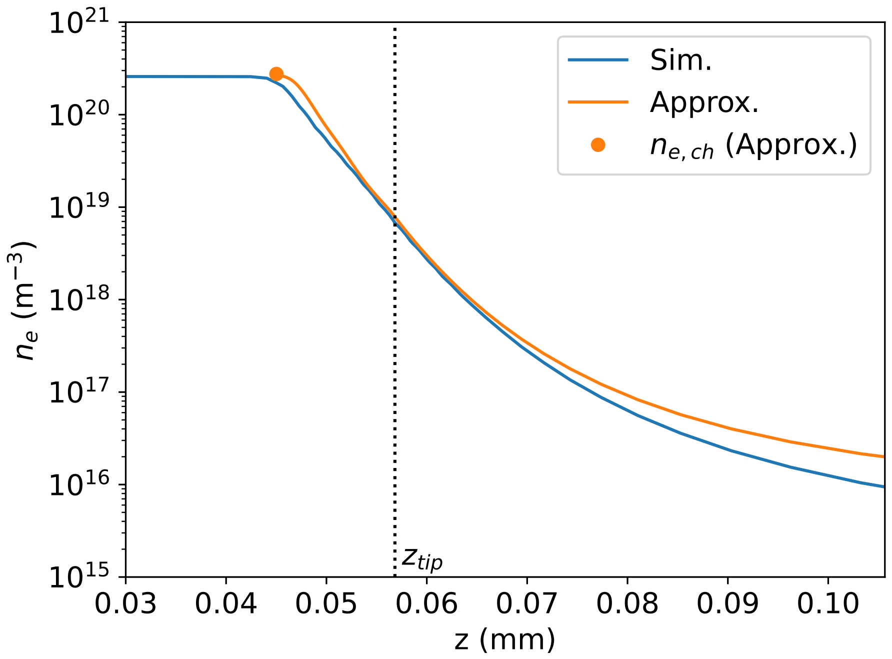

Figure 5.8: Our approximation (orange) for the electron density compared to numerical results (blue) of a steady streamer simulation. The applied background field is 4.5 kV/cm. The approximated parameters used to make this comparison are evaluated in figure (5.9)

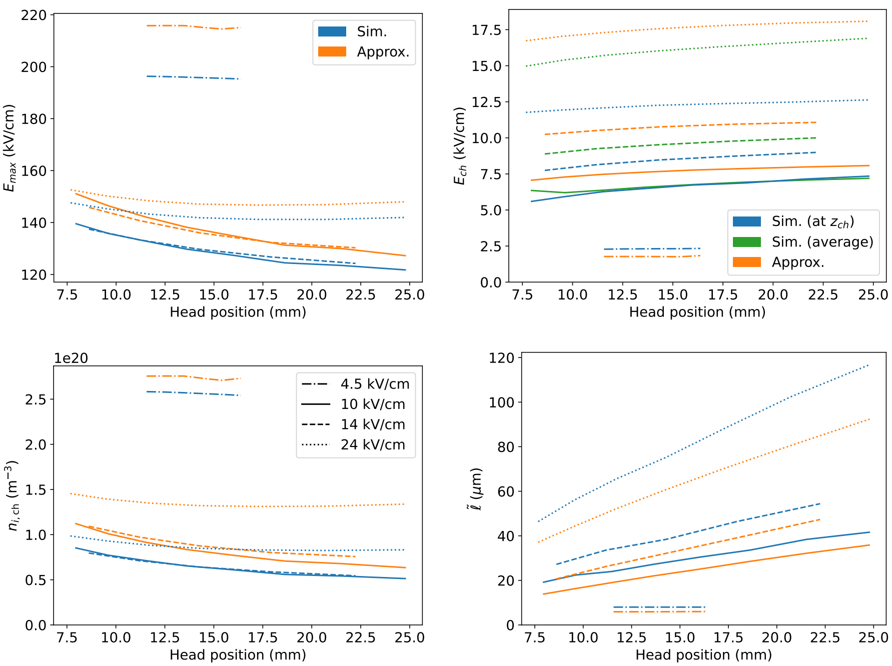

Figure 5.9: Comparison of simulations (blue, green) and our approximations (orange) for streamers with varying head positions in different background fields E_{bg}. E_{bg}, L, R and v were taken from the simulations and used to calculate the plotted approximations from (5.63). The plotted quantities are the maximum electric field $E_{\max}$, the (average) channel electric fields E_{ch}, the degree of ionization $n_{i,\mathrm{ch}}$ and the charge layer width $\tilde{\ell}$. The four background electric fields E_{bg} are plotted as $-\cdot-\cdot$ for 4.5 kV/cm (steady), —— for 10 kV/cm, $---$ for 14 kV/cm, and $\cdot\cdot\cdot$ for 24 kV/cm).

Accelerating streamers:

As discussed in the introduction, we shall now apply our analysis developed for steady streamers to accelerating streamers. We include results, calculated in the same manner, for streamers at background electric fields of 10, 14 and 24 kV/cm. The corresponding velocity and radius as a function of streamer length were already shown in figure 5.4.

The approximated parameters are included in figure 5.9. In this case we also observe good agreement with relative errors of at most several tens of percent. Only at 24 kV/cm do we have relative errors of about $50-60\%$ for the estimation of $n_{i,\mathrm{ch}}$. Furthermore, we also illustrate the error introduced by our simplistic treatment of the channel electric fields. For accelerating streamers we have included both E_{ch} and the averaged $\bar{E}_{\mathrm{ch}}$ in figure 5.9. In section 5.5 we have used $E_{\mathrm{ch}}=\bar{E}_{\mathrm{ch}}$ in order to obtain an equation for the channel electric fields without resolving the entire charge transport dynamics of the channel. However, this approximation is generally not true and the accuracy is worst for the 24 kV/cm case. This has various causes, such as a persisting neutral seed (i.e. due to shorter propagation times the influence of initial conditions still persist), actual inhomogeneities in the channel or the influence of boundary conditions.

Overall, our model is also able to estimate the properties of streamers in higher background fields. Evidently, approximating the charge layers of accelerating streamer heads as planar fronts in a steady state gives reasonable results.

5.7 Summary and outlook

5.7.1 Summary

In this work we have proposed an model that characterizes a single positive air streamer on the basis of observable parameters. Overall, our approximations exhibit good agreement with numerical simulations of a steady streamer with typical relative errors below 30%. For accelerating streamers the errors are slightly higher, with a maximum deviation up to 60% in the highest considered background field.

Our most important theoretical contributions are:

- We have constructed a self-contained axial model that can approximate macroscopic properties of steady streamer heads. This model also gives good results for accelerating streamer heads.
- We have shown how the quantities $n_{i,\mathrm{ch}}$, E_{max}, E_{ch} and ℓ can be determined from the easily observable parameters R, v, L and E_{bg}.
- We have provided a formula for the ionization degree of a streamer. Notably this formula contains the contribution due to a non-zero total current density and is about twice as high as the classical formula.
- We have given a self-consistent description of electron dynamics which includes the implicit contribution due to photoelectrons produced in the avalanche zone.

5.7.2 Outlook

For future work we recommend three possible improvements:

- We have not considered explicitely solving the dynamics of the charge layer. Instead we have accounted for these dynamics by heuristic parameterizations. However, a numerical approach that resolves densities and the electric field inside the charge layer can be expected to improve the accuracy. Moreover such an approach could replace a number of parameterizations, which would lead to a more precise representation of streamer dynamics.
- We have used two approaches for the channel electric fields. For accelerating streamers we have used an average value $\bar{E}_{\mathrm{ch}} = E_{\mathrm{ch}}$, and for steady streamers we have used an exponential decay with a prescribed length scale L_{loss}. These clearly have their limitations. In future work we aim to combine the insights obtained in this research with models that explicitly evaluate the dynamics of the streamer channel, such as [81].

- All derivations in this work assume that the dynamics of the charge layer can be approximated in a planar front setting, since the dimensionless parameter ℓ/R is typically low. A better description of the curvature will likely improve the accuracy of our model.

Finally we comment on the significance of our work regarding the development of accurate streamer tree models such as [81, 83]. The current limitation of these models is that they lack a self-consistent description of velocity and radius of a streamer. These parameters are often imposed. However, our model can be combined with a tree model in order to overcome this critical limitation.

Chapter 6

SF_6 destruction by atmospheric streamer discharges

Sulfur hexaflouride (SF_6) is an inert gases in the atmosphere that absorb infrared radiation and affect the climate. It has a predicted lifetime of up to 1278 years. The International Panel on Climate Change lists it as part of the most influential long-lived, well-mixed greenhouse gases. In this study, we investigate whether electric discharges caused by thunderstorms can contribute to decreasing the atmospheric concentrations of SF_6. We aim to estimate SF_6 decomposition by plasma reactions in streamer discharges in the atmosphere, that appear in lightning or in sprite streamers, which can occupy large volumes in the middle atmosphere. To accomplish this, we simulate positive streamers in synthetic air that contains a small concentration of SF_6. From our simulations, we also want to identify relations between the amounts of SF_6 destroyed and streamer properties, which can be used to estimate the rates of chemical processes in observed streamer events. We found that a single streamer can destroy up to 2% of the SF_6 density, and more destruction is expected in gases with higher densities. For electric fields below 20 Td, we do not observe scaling in the fraction of SF_6 destroyed.

This chapter will be extended for publication as:
SF_6 destruction by atmospheric streamer discharges by Hani Francisco, Ute Ebert, John Plane, and Martin Füllekrug.

6.1 Introduction

6.1.1 The man-made greenhouse gas SF_6

SF_6 is a widely-used insulating gas with an atmospheric concentration of 8 ppt in 2015 [139]. It has a predicted atmospheric lifetime of 1278 years and a 100-year global warming potential of 23500. This means that in a span of 100 years, the emissions of SF_6 will absorb 23800 times the energy that the emissions of the same mass of carbon dioxide will absorb in the same time span - making SF_6 the most potent greenhouse gases in the atmosphere [90]. SF_6 is not naturally occurring but is emitted at ground levels following human activity, mostly from the electrical industry. Its mixing time in the troposphere is on the order of a year [118].

6.1.2 Known mechanisms of SF_6 destruction

Climate models have evaluated that most atmospheric loss of SF_6 is due to the attachment of thermal electrons [122, 139]. Electrons attach to SF_6 to produce SF_6^-, that can then react with a hydrogen atom or an HCl molecule for permanent SF_6 removal. Otherwise, SF_6^- could undergo photodetachment or react with ozone or atomic oxygen, which recycles SF_6 back into the atmosphere [123]. The highest removal rate due to associative attachment was estimated to be on the order of 10^{-6} s^{-1} at around 70 km altitude [139], where the H density $[H]$ is 10^{13} m^{-3} [9].

The associative attachment reaction is the dominant destruction mechanism until around 115 km, above which photolysis dominates SF_6 destruction with a removal rate around 10^{-7} s^{-1} [139].

Another electron attachment reaction that could lead to SF_6 removal is the dissociative attachment reaction that yields SF_5^-. This attachment reaction becomes the dominant attachment reaction at 120 km altitude, but at that altitude, photolysis is already the dominant SF_6 destruction mechanism [139]. In this context, dissociative attachment and photolysis don't contribute much to the removal of SF_6 in the atmosphere because most SF_6 molecules don't even reach above 75 km due to diffusive separation - the molecules' slower diffusion speed compared to air molecules doesn't let them reach higher altitudes - and SF_6 molecules are already being destroyed at lower altitudes [66].

6.1.3 Lightning-induced atmospheric chemistry and the streamer mechanism

The mechanisms above account for a standard atmospheric composition, and do not consider the enhanced density of free electrons down to ground level during thunderstorms. These electrons and their possible impact on SF_6 destruction at various altitudes in the atmosphere are the topic of the present study.

We focus here on streamer discharges which are the first stages of electric breakdown in air. Streamers are directly visible as enormous sprite discharges above thunderstorms at 40 to 80 km altitude, but they also occur as streamer coronas ahead of lightning leaders in the troposphere. In general, streamers are plasma channels that propagate by strong field enhancement at their tips. The electron energy distributions in these high field zones are very far from equilibrium, with a substantial fraction of electrons reaching energies of 12 to 15 eV, sufficient for the ionization of oxygen or nitrogen molecules and hence, for a further plasma growth. For a recent review of streamer physics we refer to [97].

The exotic plasma chemistry in streamer discharges is used in numerous technical applications. In atmospheric chemistry the impact of streamers has been found as well, e.g. in the production of the greenhouse gases NO_x and O_3 [89]. NO_x production that only considers return strokes and neglects all the other lightning process was found to be unjustified, as NO_x production mainly takes place in slow discharge processes, being most influenced by the length of the lightning discharge channel [32]. Brune et al. [26] recently reported that during an airplane mission they found extreme concentrations of the oxidant HO_x in cloud regions with only subvisible discharges, as enhanced amounts of the oxidant was found in regions where no electrical activity or flashes were detected by the lightning mapping array. These findings support our case that streamer discharges have the capacity to influence SF_6 removal in the atmosphere as well.

Most air mass in the atmosphere is in the troposphere, and through thunderstorms, photons and free electrons are introduced at these altitudes instead of just in the ionosphere. We aim to discover at which altitudes streamers are best at destroying SF_6 and by which removal process.

Table 6.1: The electron reactions with SF_6 that are included in the model.

Reaction		Energy	Ref.
Associative electron attachment:			
1	$e + SF_6 \rightarrow SF_6^-$	0 eV	[28]
Dissociative electron attachment:			
2	$e + SF_6 \rightarrow SF_5^- + F$	0 eV	[28]
3	$e + SF_6 \rightarrow SF_5 + F^-$	2.0 eV	[28]
4	$e + SF_6 \rightarrow SF_4^- + F_2$	3.5 eV	[28]
5	$e + SF_6 \rightarrow SF_4 + F_2^-$	1.5 eV	[28]
6	$e + SF_6 \rightarrow SF_3^- + F_3$	8.0 eV	[28]
7	$e + SF_6 \rightarrow SF_2^- + F_4$	10.3 eV	[28]
Neutral dissociation:			
8	$e + SF_6 \rightarrow e + SF_5 + F$	9.6 eV	[28, 56]
Dissociative ionization:			
9	$e + SF_6 \rightarrow 2e + SF_5^+ + F$	18.0 eV	[124]

6.1.4 SF_6 destruction in atmospheric streamer discharges

The electron densities and their energies in the streamer discharge determine which SF_6 reactions will occur there. Table 6.1 lists the electron reactions with SF_6 included in our study, with their required energies and our cross sections references.

The first reaction in the table is dissociative electron attachment that forms SF_6^-. It requires no activation energy and is the first step towards the dissociation by H or HCl mentioned above in section 6.1.2. All the other reactions in the list remove at least one fluorine from the molecule, which is a certain path to destruction. We therefore consider all dissociative reactions (numbers 2 to 9 in the table) as destruction mechanisms for SF_6. We note that the second reaction toward SF_5^- + F is mentioned in section 6.1.2 as well. It does not require any activation energy, but is limited by the availability of free electrons. In the present paper we will analyze its importance considering the electron densities and energies found in streamer discharges. The third reaction towards SF_5 + F^- requires an electron energy of at least 2 eV, and it could play a role in the region of field enhancement at the streamer head.

Table 6.2: Altitude in the atmosphere, local number density N of air molecules according to [99] and height of our computational domain. The domain radius is half of the domain height.

Altitude [km]	Air number density N [m^{-3}]	Domain height $H_0 \cdot N_0/N$
0	$N_0 = 2.55 \times 10^{25}$	$H_0 = 40$ mm
10	8.58 x 10^{24}	119 mm
20	1.83 x 10^{24}	558 mm
40	8.02 x 10^{22}	12.7 m
60	5.99 x 10^{21}	170 m
80	3.28 x 10^{20}	3.10 km

6.1.5 Streamers at different atmospheric altitudes and scaling with density

Streamer discharges can appear in the atmosphere, at altitudes below the ionosphere. Table 6.2 lists the altitudes from 0 to 80 km investigated in the present study. The second column lists the air density, more precisely the molecule number density N, at the respective altitude according to the U.S. Standard Atmosphere (1976) [99]. This density changes by almost five orders of magnitude from 0 to 80 km altitude. The air density N_0 at ground level is introduced as a reference.

As reviewed in [97], the streamer phenomenon is nevertheless remarkably similar at different air densities. This is because the primary reaction in the fast streamer head is a two-body reaction between an electron and an air molecule which leads to elastic, inelastic, or ionizing scattering of the electron or to electron attachment on the molecule. These reactions depend on the electron energy. This energy in turn depends on the local electric field times the mean free path ℓ_{MFP} of the electron, and the mean free path is inversely proportional to air density, $\ell_{\mathrm{MFP}} \propto 1/N$. Therefore, when comparing streamers at different air densities N, all lengths and times roughly scale as $1/N$ and electric fields as N; following this, the reduced electric field E/N has been introduced in the plasma community. Furthermore, an analysis of the streamer equations reveals that the degree of ionization inside a streamers scales with N^2 [97]. However, scaling with air density is not perfect as three-body reactions and collissional quenching of excited states become important at higher air density.

In the present paper, we will scale lengths, times, electric fields, and particle densities with air density N, and we will analyze the corrections to this scaling in our results. The scaling of the lengths can already be seen in the different computational domain sizes listed in table 6.2.

6.1.6 Structure of the paper

We start by detailing our numerical modeling in section 6.2, where we present the SF_6 destruction mechanism we considered in section 6.2.2 and explain how we adapted our simulation for different altitudes at section 6.2.4. In section 6.3, we look at the different streamers at different altitudes and the charged species in their wake. We introduce an expression to analytically approximate the time evolution of SF_6 density at certain conditions in section 6.4, and we conclude our investigations in section 6.6.

6.2 Set-up of streamer model

6.2.1 Model and computational method

In all simulations, we employed the classic fluid model which uses local field approximation to compute for the evolution of the densities of electrons, ions, and neutral molecules in a cylindrically symmetric domain. The simulations were run using the Afivo-streamer code [136, 137], where Afivo stands for adaptive finite volume octree. This code uses an adaptive mesh and a drift-diffusion-reaction equation for the electron density evolution

$$\frac{\partial n_e}{\partial t} = \nabla \cdot (n_e \mu_e \mathbf{E} + D_e \nabla n_e) + S_i - S_\eta + S_{ph} + S_{ion}, \qquad (6.1)$$

where μ_e is the electron mobility, $\mathbf{E}$ is the electric field, D_e is the electron diffusion coefficient, S_i is the impact ionization source term, S_η is the electron attachment source term, S_{ph} is the non-local photoionization source term, and S_{ion} is the source term for electron detachment reactions minus the electron-ion recombination reaction. The same model has been used in [40, 51].

The photoionization source term is the same as in [40, 75]; it is given by

$$S_{ph}(\mathbf{r}) = \int d^3r' \, \frac{I(\mathbf{r}')f(|\mathbf{r}-\mathbf{r}'|)}{4\pi|\mathbf{r}-\mathbf{r}'|^2} \tag{6.2}$$

where $I(\mathbf{r})$ is the source of ionizing photons, $f(r)$ is the absorption function, and $4\pi|\mathbf{r}-\mathbf{r}'|^2$ is a geometric factor. Following Zheleznyak's model [149], the photon source term $I(\mathbf{r})$ is calculated using

$$I(\mathbf{r}) = \frac{p_q}{p+p_q}\xi S_i(\mathbf{r}) \tag{6.3}$$

where p is the actual gas pressure, p_q is a gas-specific quenching pressure, and ξ is a proportionality factor. In principle, this proportionality factor is field-dependent [149], but in this paper, we set it to $\xi = 0.075$ as in [40, 146]; this value reproduces streamer branching very well [146]. Furthermore, we use the commonly assumed quenching pressure of $p_q = 40\,\mathrm{mbar}$. In Zheleznyak's model, $f(r)$ is an effective function for the absorption of photons in the wave length range of 98 to 102.5 nm. It is obtained with

$$f(r) = \frac{\exp(-\chi_{\min}p_{O_2}r) - \exp(-\chi_{\max}p_{O_2}r)}{r\ln(\chi_{\max}/\chi_{\min})}, \tag{6.4}$$

where $\chi_{\max} \approx 1.5 \times 10^2/(\mathrm{mm\ bar})$, $\chi_{\min} \approx 2.6/(\mathrm{mm\ bar})$, and p_{O_2} is the partial pressure of oxygen. We used a set of Helmholtz differential equations [19, 84] with Bourdon's three-term parameters [19] to evaluate the photoionization integral.

The other charged and neutral species Z_i in our model evolve in time according to the continuity equation

$$\frac{\partial n_{Z_i}}{\partial t} = -s_i\nabla\cdot(n_{Z_i}\mu_i\mathbf{E}) + S_{Z_i} \tag{6.5}$$

where $s_i = \pm 1, 0$ is the sign of the electric charge of species i, μ_i is its mobility, and n_{Z_i} is the density of the species Z_i. Since ion mobilities are typically about two orders of magnitude lower than electron mobilities, we neglect ion motion in this paper for simplicity. S_{Z_i} is the source term that accounts for reactions that produce and consume Z_i. For example, the reaction source term for the continuity equation of SF_5^- is

$$S_{SF_5^-} = k_2 n_e n_{SF_6}, \tag{6.6}$$

where k_2 is the reaction rate coefficient of reaction 2 in table 6.1. There is only one term in this expression because we only have one reaction that involves SF_5^- in our model, and the term is positive because the reaction produces SF_5^-.

The simulations were done at different pressures to mimic different altitudes. The following describes the set-up for the 0 km case. The electric potential was fixed at $z = 0$ mm and $z = 40$ mm to achieve a homogeneous background electric field pointing in the $-\hat{z}$ direction. At $r = 20$ mm, Neumann zero boundary conditions ($\partial_r \phi = 0$) were applied on the electric potential, and for $r = 0$ mm, the boundary condition follows from cylindrical symmetry. Neumann zero boundary conditions are applied for the electron density at all boundaries, and no background ionization was introduced into the domain. The same boundary conditions are applied for the other altitudes, as these are standard for these simulations. All lengths were scaled with air density as described in section 6.1.5 and listed in table 6.2.

We used the same refinement criteria as described in [39]: Adaptive mesh refinement is used, with the grid set to have a minimum size of 2.4 μm for the 0 km case. This minimum grid size is also scaled with gas density for the other altitudes. The refinement and derefinement criteria are based on the local electric field value as in [136]: refine if $\alpha(1.2 \times E)\Delta x > 0.5$ and derefine if $\alpha(1.2 \times E)\Delta x < 7.5 \times 10^{-2}$, where $\alpha(E)$ is the field-dependent ionization coefficient, E is the electric field strength, and Δx is the grid spacing.

We also used the same set of reactions for nitrogen and oxygen species as in [40] with the addition of the electron-recombination reaction to N_2^+ from [65]. For these reactions, The cross-sections for the electron impact reactions are from [1, 113], and Bolsig+ [54] was used to calculate for the transport and reaction rate coefficients with the assumption of a temporal growth model[147]. It is sufficient to only consider electron reactions with nitrogen and oxygen molecules in determining the transport coefficients and reaction rates in this gas because, as previously mentioned, the SF_6 concentration in the atmosphere is very low.

6.2.2 SF_6 reactions and their reaction rates

To model SF_6 decomposition, reactions that involve electrons and SF_6 have been added to the model we use for air simulations. A list is given at table 6.1.

The reaction rate coefficients for electron attachment and impact ionization reactions involving SF_6 were calculated from measured cross-sections [28, 124] using Bolsig+ [54] with the EEDF for air, as argued in the previous subsection. Only one ionization reaction is included as the rest have threshold energies of 22.5 eV and higher [124]. Reactions that have threshold energies higher that 19 eV were not included because they have low chances of occurring.

Due to unavailability of cross sections data for separate neutral dissociation reactions, we use the total dissociation cross section to compute the rate coefficient of reaction 8. This approximation is suitable since we are only concerned with the destruction of SF_6 and not with the products of the dissociative reactions. The SF_5 molecule was chosen as the product of the neutral dissociation reaction we included as it is the dominant dissociation product [61]. Relative cross sections for neutral dissociation reactions to SF_2 and SF are available but we do not include them as they have threshold energies as high as 19.5 eV and 22.0 eV, respectively [56].

Only SF_6 reactions with electrons are included because SF_6 is extremely inert. The electric field together with collisions data determine the electron energies and velocities, and thus, the reaction rate coefficients (and transport coefficients). The electron energy distribution function in streamers in air, which can be seen in figure 3 of [35], show that most electrons in the streamer channel have energies around 1 eV only, and merely a few electrons at the streamer tip have energies above 10 eV. The highest reaction rate coefficients for SF_6 reactions and the total reaction rate coefficient incorporating all SF_6 destruction reactions are plotted as a function of the reduced electric field E/N in figure 6.1.

We plot the reaction rates as a function of the reduced electric field E/N according to the scaling arguments of section 6.1.5, using the unit Townsend, defined as $1\ \mathrm{Td} = 10^{-21}\ \mathrm{V} \cdot \mathrm{m}^2$. In air at ground level, the breakdown field (where $S_i = S_\eta$) is 29.5 kV/cm which corresponds to 115 Td.

Removing at least one fluorine atom is a sufficient criterion for SF_6

destruction in our study because the concentration of these species are too low that SF_6 won't be formed again after dissociative reactions.

Figure 6.1 shows that there are three dominating electron-SF_6 reactions: associative electron attachment to SF_6 that leads to SF_6^-, closely followed by dissociative attachment that forms $SF_5^- + F$ in the lower field range, and neutral dissociation of SF_6 to $SF_5 + F$ above 150 Td. In this study, we do not consider SF_6^- to lead to SF_6 destruction (as will be discussed in the next subsection), but all the other reactions do, therefore we define the reaction rate coefficient for SF_6 destruction as

$$k_{SF_6} = \sum_{n=2}^{9} k_n, \tag{6.7}$$

where n labels the reactions of table 6.1. The destructive reaction that dominates the low field range is the dissociative attachment reaction that produces SF_5^-.

From 300 Td, SF_6 ionization has a higher reaction rate coefficient than any SF_6 attachment reaction, and it is the second fastest SF_6 reaction following the neutral dissociation reaction. The dominant attachment reaction is associative attachment until about 680 Td, and at fields higher than this, the dissociative attachment reaction that produces F^- and SF_5 progresses faster than all other attachment reactions. At 500 Td, this dissociative attachment reaction is already faster than the dissociative attachment reaction that produces SF_5^- and F, which dominated SF_6 destruction in the lower field range.

6.2.3 SF_6^-

In figure 6.1, we included a blue region which corresponds to the electric field range we found in our streamer channels. We see that the dominant reaction there is the associative attachment reaction that produces SF_6^-. SF_6^- is a stable negative ion with lifetimes ranging from a hundred microseconds to a few seconds, depending on the energy of the SF_6 molecule before electron attachment and on the energy of the attaching electron [120]. This timescale is only relevant for our streamers above 40 km altitude. At lower altitudes, SF_6^- formation is an electron sink, but with SF_6 density being low, the effect of this to electron density is considered negligible.

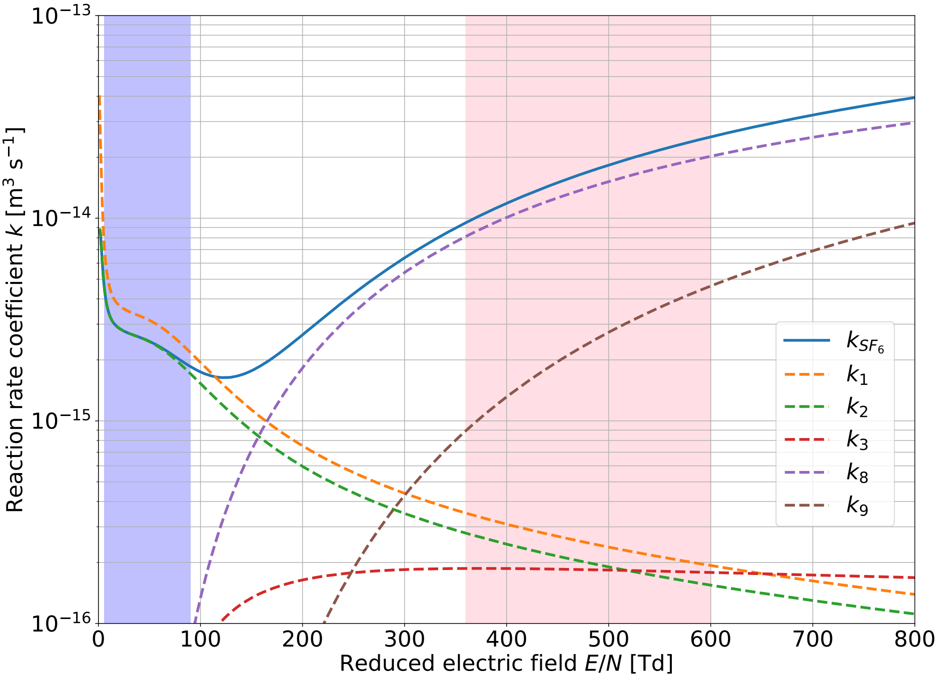

Figure 6.1: Reaction rate coefficients k_n of the dominating reactions of electrons with SF_6 as a function of the reduced electric field E/N. The broken lines correspond to individual SF_6 reactions.. The solid line is the sum of all reaction rates that destroy SF_6 (equation (6.7)). The blue region around 6 - 90 Td represents the electric field range observed inside streamer channels while the red region from 360 - 600 Td represents the range of enhanced electric fields at the streamer head.

We do not consider SF_6^- formation as an SF_6 destruction mechanism in this study. SF_6^- can react with atomic oxygen or ozone, and these reactions recycle SF_6 back to the system. SF_6 can also be recovered from SF_6^- by photodetachment, which has a rate of about 0.11 s^{-1} at 85 km [66, 139].

SF_6 destruction from SF_6^- can come about through reactions with H or HCl. Reaction with HCl is disregarded as HCl is only found in the stratosphere [144] with its rare jet discharge events) or it is already bound to droplets inside clouds. SF_6^- destruction by atomic hydrogen only dominates over photodetachment of SF_6^- above 80 km [123], and our simulations only consider up to this altitude.

Aside from electron attachment, SF_6^- may also be produced by electron transfer from O_2^-, an anion with a lower electron affinity. We do not consider this reaction as this only creates more SF_6^-, which we do not consider as an SF_6 destruction pathway.

6.2.4 Configuration of simulations

We simulate in air at different altitudes, and to do so, we vary the gas number density following the altitude dependent profile from U.S. Standard Atmosphere (1976) [99]. We employ scaling laws to describe how the discharges scale with the gas number density.

A summary of the key differences of the computational domain for the different simulations is given at table 6.2. The numbers presented there were calculated following the scaling laws. The domain lengths are just half of these values. The maximum time step, size and density of the seeds used for streamer initiation, and the grid refinement size limits have also been scaled accordingly. For the original values, we refer the reader to [40].

SF_6 is only included as a small amount, having a density that corresponds to 8 ppt. This left the gas mixture to correspond to that of dry air with 80% nitrogen and 20% oxygen, which allowed us to use the same transport coefficients calculated for dry air using Phelps data [1] and Bolsig+ [54], leading to an electron energy distribution that is derived for air. That calculation was done using the temporal growth model [147].

For each altitude, we looked at streamers at three different electric fields: (1) 21.6 Td, (2) 58.8 Td, and (3) 96.0 Td. At ground pressure, these electric fields correspond to (1) 5.5 kV/cm, (2) 15 kV/cm, and (3) 25 kV/cm. All are below the breakdown field of 29.5 kV/cm at ground pressure, or 115 Td. Streamer branching breaks cylindrical symmetry [80], which means that our simulation setup is only valid for single streamers. Initiating a streamer at low fields and having it cross the boundary without branching is not easy to achieve [40, 75]. In order to get a non-branching streamer at 21.6 Td, a streamer was first initiated at a higher background field of 98 Td before slowly decreasing the background field to 21.6 Td. The results we present for the 21.6 Td streamers in the next section only include the data when the background field has reached 21.6 Td. There were no difficulties in initiating and getting a non-branching streamer at 58.8 Td and 96.0 Td, and these cases had the background electric field constant the whole time.

6.3 Streamers at different altitudes and in different fields

6.3.1 A first overview

Streamers in three different electric fields and at the two altitudes of 0 and 80 km are shown in figure 6.2.

First, the upper row shows streamers at ground level in background electric fields of 21.6, 58.8, and 96.0 Td at the moment when they have traversed 75% of the simulation domain of 40 mm. Velocity, radius, and the created electron density depend on the background electric field as well as on the initial conditions [40].

Second, the lower row of the figure shows streamers at 80 km altitude. Overall, the spatial structures look very similar, but times and lengths are roughly five orders of magnitude larger; electric fields and air densities are five orders smaller; electron densities are ten orders smaller; and the velocities are of the same order. These are in agreement with the scaling laws with air density N that were recalled in section 6.1.5. There is a strong correspondence between the streamers at 0 or 80 km altitude, because we chose initial conditions and background fields according to gas density scaling. However, the limitations of scaling that are known to be due to three-body reactions and quenching of excited states are still noticeable. For example, in fields of 21.6 Td and 58.8 Td, the streamers at 80 km altitude still have substantial electron densities along their whole length, while their counterparts at 0 km have reduced electron densities at their back ends.

6.3.2 Streamer dynamics and corrections to scaling

In figure 6.3 we plot the electric field at the streamer tip, the streamer velocity, and the streamer radius as a function of the streamer length of all our simulated streamers. We use the reduced electric field and scaled streamer lengths and radii in the axes of the figure so we can directly compare streamers at different gas densities. Streamers at the same altitude that have different background fields follow the observations in [40], where the streamer velocity and radius increase with the background field. It was shown in that paper that the relationship between the background field and the maximum electric field is non-monotonic, with the maximum electric field having a minumum for some intermediate background field. Although not clearly evident with the results we present, we observed the same non-monotonic relationship with our new set of simulations, with the minimum being at a background field of around 23.5 Td.

When comparing streamers at different altitudes, we find from figure 6.3 that only the streamers at 40 km altitude and above coincide after scaling, while the streamers in lower altitudes show the familiar corrections to scaling. It was shown in [76] that photoionization introduces corrections to the streamer scaling properties at sprite altitudes due to the absence of the quenching of states responsible for photoionizing radiation. An increase in photoionization lowers the maximum electric field ahead of the streamer and the electron density. Photoionization has a quenching threshold that could be found at around 24 km [149], and this is consistent with the fact that streamers at 20 km and below show corrections to the scaling laws.

6.3.3 Densities of charged species on the streamer axis

To further investigate the corrections to the scaling laws, we look at the axial electron density of streamers at different altitudes in a field of 21.6 Td. This is shown in the topmost panel of figure 6.4. We see that scaling works perfectly for the electron densities at 40, 60, and 80 km altitude - so well even that the 80 km data is hidden below the 60 km data. At the lower altitudes of 0, 10, and 20 km, we see corrections of up to a factor of 2 to the

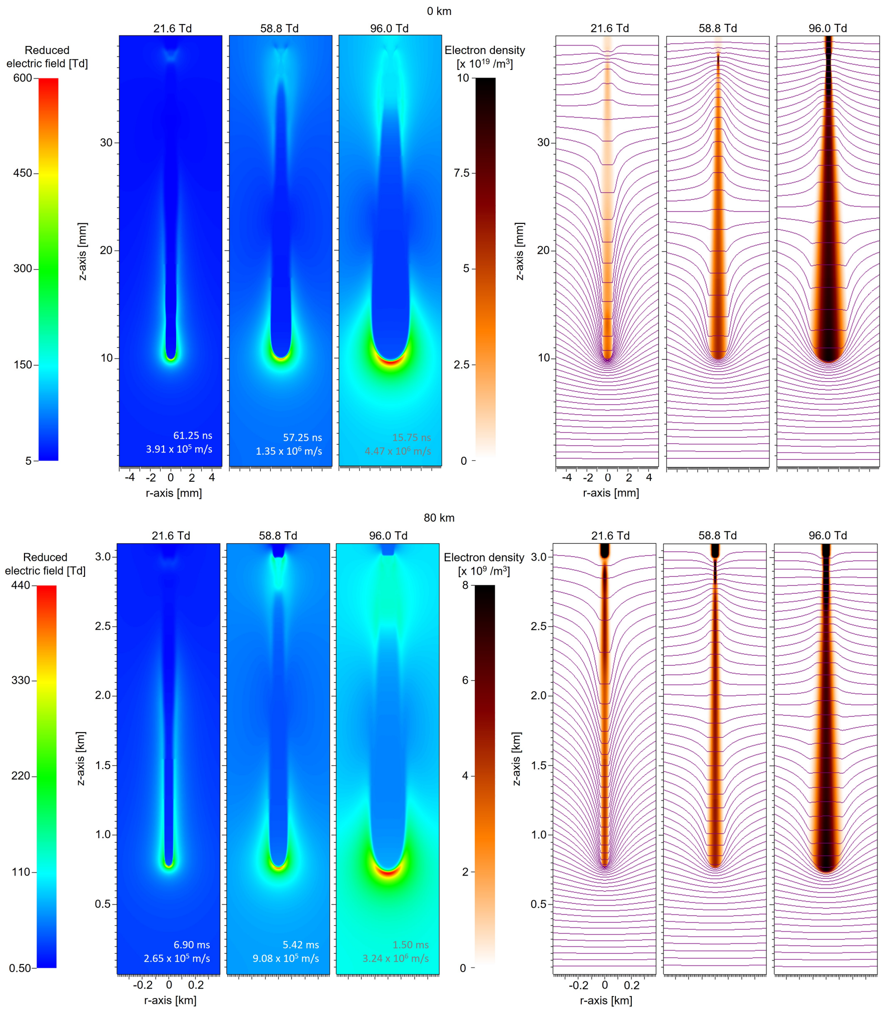

Figure 6.2: Plots of electric field (left) and electron density with purple equipotential lines (right) of different streamers at 0 km (upper panel) and 80 km (lower panel) altitudes. We note that not the whole width of the computational domain is shown. The streamers are shown when they have traversed 75% of their computational domain. The times at which these were taken and the streamer velocities at that instant are in the bottom right of plots depicting the electric field. Note that not the whole radial width of the computational domain is shown.

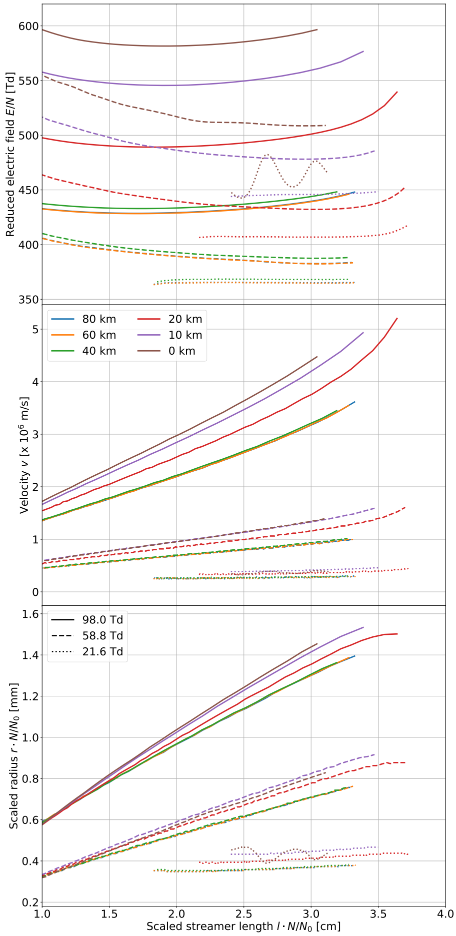

Figure 6.3: Plots of streamer properties at different background fields and altitudes. The maximum of the reduced electric field E/N (upper plot), the streamer velocity v (middle plot), and the scaled radius $R \cdot N/N_0$ (lower plot) are plotted as a function of the reduced streamer length $L \cdot N/N_0$ where N_0 is air density at ground level. The solid, dashed and dotted lines correspond to streamers in a reduced background field of 98.0 Td, 58.8 Td or 21.6 Td which corresponds to fields of 5.5, 15 and 25 kV/cm at ground level. The streamer lengths were measured as the distance from the maximum of the electric field to the top boundary of the computational domain.

scaling laws. We also observe that for all streamers shown, only the one at 0 km has an electron density profile that is decreasing from the streamer head to the back of the streamer channel.

A better understanding of what is happening inside the streamer channel can be gained by looking at the electron loss mechanisms in it at the extreme altitudes of 0 and 80 km.

In the middle and bottom panels of figure 6.4, the axial densities of charged species at 0 and 80 km altitude are shown. At 80 km altitude they are fairly constant, while at 0 km altitude, there is a conversion chain of positive ions from N_2^+ to N_4^+ to O_2^+ to O_4^+. This does not happen at the higher altitude because this chain involves three-body reactions, and the gas density at 80 km is too low for these reactions to occur on the timescales simulated. Thus, the change in the dominant positive ion species in the streamer channel, from O_4^+ at 0 km streamer to N_2^+ at 80 km.

Electron recombination to the dominant positive ion species have been found to be an important loss mechanism in the streamer channel [40], and O_4^+ easily recombines with free electrons to form two O_2 molecules, which explains the decrease of the electron density in the streamer channel at 0 km. Based on the mean energy of the electrons in the channel and the relevant ion densities, we calculated the electron recombination time to increase from 100 ns in 0 km to 5000 s in 80 km. Our slowest streamer at 80 km took 9.1 ms to cross the 1.55 km gap, leaving the electrons inside the channel with insufficient time for electron recombination.

Another important electron loss mechanism in the streamer channel is electron attachment [40], and as reported in [82], in gases with low number densities, the three-body attachment reaction is suppressed. The suppression of three-body electron attachment at higher altitudes increased the attachment times from 86 ns in 0 km to 0.11 s in 80 km. Again, there is insufficient time for electron attachment reaction to occur for the 80 km streamers in our simulations. On the other hand, the streamers at 0 km took between 15-94 ns, depending on the background electric field, to cross the 40 mm domain so the electrons in the streamer channels there had sufficient time to attach. The slowed down rates of the electron loss mechanisms in the streamer channel of 80 km streamers explain why the electrons are long-lived for their case unlike for the 0 km streamers.

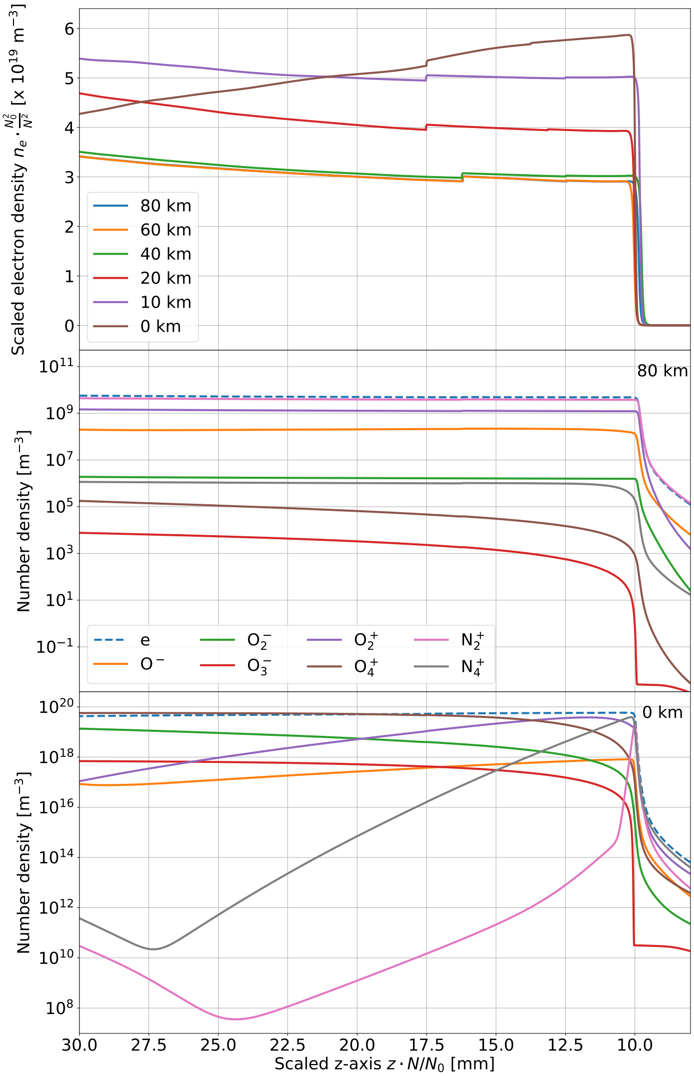

Figure 6.4: Charged species densities on the streamer axis in fields of 21.6 Td at the moment when the streamers have crossed 75% of their computational domain. This is the same situation as in the left columns of Fig. 6.2. The upper plot shows the electron density on linear scale for different altitudes, and the lower plots show 8 relevant charged species on a logarithmic scale, at 80 and 0 km altitude.

6.3.4 Electric field and electron density

Analyzing the electric field distributions and electron density profiles helps us identify where SF_6 destruction could occur inside or in the vicinity of the streamer. Possible SF_6 destruction paths due to free electrons were already summarized in section 6.2.2 and table 6.1.

SF_6 could be destroyed either via electrons in the enhanced electric field at the streamer head or via lower energy electrons in the streamer channel. The electron energies are determined by the local electric field. The electric field ranges where these happen are highlighted in figure 6.1.

Figure 6.4 features several axial electron density profiles - the topmost panel shows the scaled electron density in linear scale, and the middle and bottom panels has the electron density represented by dashed lines. For all cases, we see that the electron density increases until around $z = 10$ mm, after which it stays in the same $10^{19}/\mathrm{m}^{-3}$ order of magnitude. These cases present streamers with tips at $z = 10$ mm, so the electron-rich area is actually the length of the streamer channel. We don't observe as much electron density ahead of the streamer tip.

Although the active zone has a much higher electric field than the streamer channel, it simply does not have enough electrons for SF_6 destruction. On the other hand, the streamer channel poses favorable conditions due to the high electron density and low electric fields. In such low fields, the electrons could attach to SF_6 with a dissociative attachment reaction (reaction 6 in table 6.1) forming SF_5^-. We thus expect most SF_6 destruction to happen in the streamer channel.

Figure 6.5 shows the temporal evolution of the electron density and the electric field at fixed points in the streamer channel along the streamer axis. For the streamers at the two higher background electric fields, we used points at $z = 30$ mm, while for the lowest field, we used the z-coordinate of the streamer head when the background field has finally reached 21.6 Td (recall that we started from a higher background field for these low-field simulations, as discussed in section 6.2.4). We see how the electron density first shoots up from a low value as the streamer head passes that point, after which the electric field declines, as the point is now in the streamer channel where the electric field is screened. The same effect of the altitude could be seen with the electron density: the electron density decreases with increasing altitude until photoionization is quenched and three-body

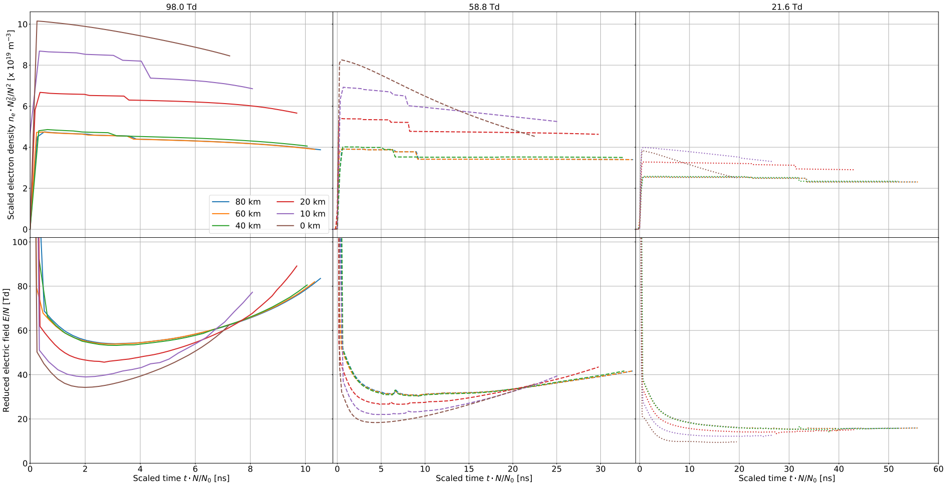

Figure 6.5: Temporal evolution of the electron density and electric field inside the streamer channel at different altitudes and background fields.

reactions are suppressed. The 21.6 Td streamer at 0 km has initial electron density values near the 21.6 Td streamer at 10 km, which is consistent with how their maximum electric fields are related, as shown in the topmost panel of figure 6.3. Both streamers start of with maximum electric fields that are near each other, which translates to having comparable electron densities as well.

The electric field inside the streamer channel decreases with altitude and, consistent with [40], decreases with decreasing background field. The 21.6 Td streamers have a channel electric field that held a constant value as time progressed, and this characteristic allows us to simulate what happens in these cases for longer timescales, which we take up in section 6.4.2.

6.4 Results on SF$_6$ destruction

6.4.1 SF$_6$ destruction in the simulated streamers

Figure 6.6 shows the fraction of SF$_6$ destroyed in streamers in different background electric fields at 0 and 80 km altitudes as a function of scaled

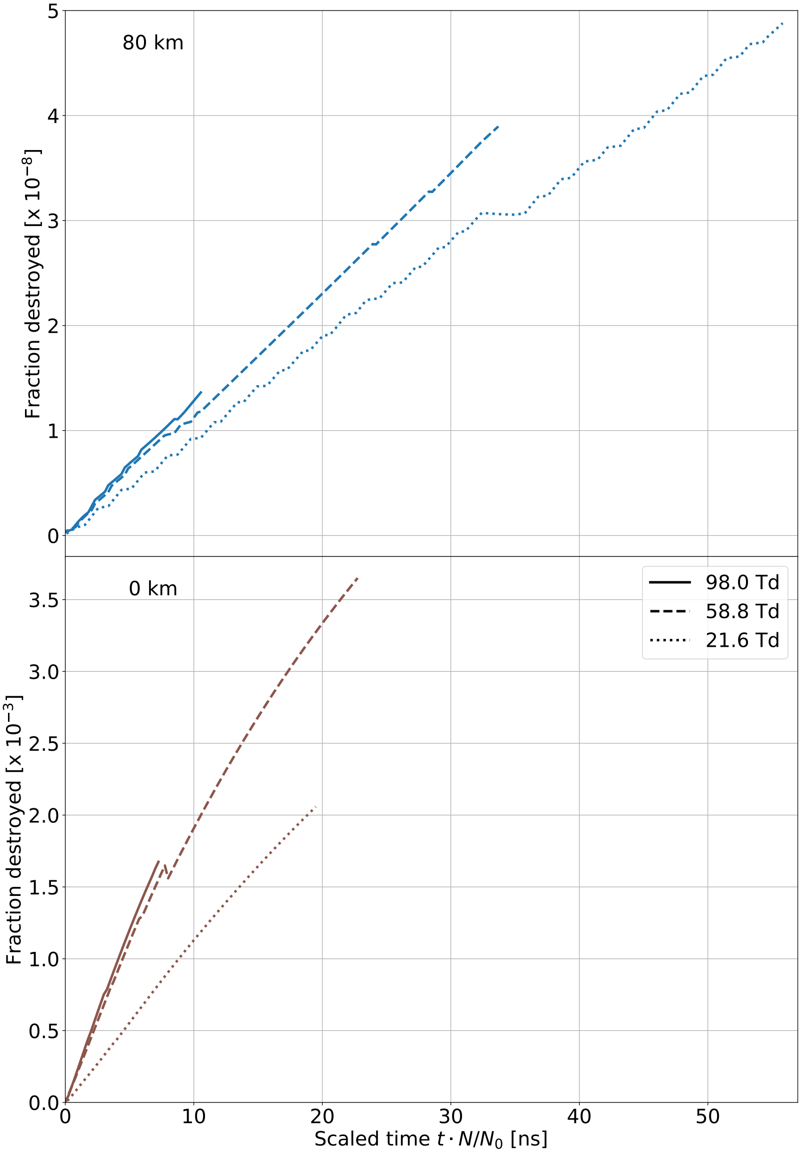

Figure 6.6: Fraction (6.8) of destroyed SF_6 as a function of scaled time $t \cdot N/N_0$ at 0 and 80 km altitude. Streamers in different background fields are indicated by solid, dashed, and dotted lines. The lines end when the streamers have crossed 75% of the gap.

time $t \cdot N/N_0$. More precisely, we measured

$$\frac{n_{SF_6}(0) - n_{SF_6}(t)}{n_{SF_6}(0)} \tag{6.8}$$

at the same fixed positions introduced in the previous section and featured in figure 6.5. Here $n_{SF_6}(t)$ is the SF_6 density at time t, and $t = 0$ is the moment when the streamer head passes the point of observation. We include the density of SF_6^- with the density of SF_6, as we assume that associative electron attachment is reversible and not a pathway to destruction, as discussed in section 6.2.3. All other reactions in table 6.1 are considered destructive, and together they determine the reaction rate coefficient $k_{SF_6}(E/N)$ of equation (6.7).

The first thing to note in figure 6.6 is that SF_6 diminishes about linearly in time, with no particular deviation at time 0 when the streamer head with its high field enhancement passes the point of observation. This means that the high energy reactions in the red region in Fig. 6.1 do not substantially diminish the SF_6 density. This is a consequence of the small size of the enhanced field zone, combined with the local electron density and the reaction rate. The decrease of SF_6 is therefore a consequence of the reactions with lower energy electrons in the blue range of Fig. 6.1.

Second, the rate of decrease of the SF_6 density depends only weakly on the background field and on the associated streamer properties, but very strongly on air density. In fact, the fraction of SF_6 destroyed varies by about a factor N/N_0 after the scaled time $t \cdot N/N_0$. This slow reaction rate at low air densities corresponds to the slow reactions along the streamer axis visible in Fig. 6.4. The higher SF_6 destruction rate of at higher air density directly follow from the higher electron density in the streamer. However, we will argue below that over sufficiently long time scales the total SF_6 destruction becomes more equal for different air densities.

Considering the weak dependence of the destruction rate on the background electric field, the 98 Td streamers have the fastest rate, evident through the higher slopes in Fig. 6.6. This is because these streamers had a higher maximum electric field, which in turn produced more electrons that could contribute to SF_6 destruction in the channel. The lower fields end up with higher fractions destroyed simply because the streamers in this fields are slower, and thus took a longer time to cross our computational domain, allowing more time for SF_6 destruction.

6.4.2 0D Model

The data shown in Fig. 6.6 end when the streamers have crossed a large part of the gap. But the linear increase of the SF_6 destruction with time indicates that longer times should be explored. To reduce the computational demand, we now use a simplified model to follow SF_6 destruction in the streamer channel. We use a 0D model that simulates the time evolution of the densities of different species disregarding the spatial structure. The equations are solved with ZDPlasKin [108].

For simplicity, the 0D model was set to use constant electric fields. Our simulation data from the channels of the 21.6 Td streamers are suitable for this application as the electric fields here are already nearly constant in time. We thus used the final state of our 21.6 Td streamers as the initial conditions for the 0D model, and the results - the electron density evolution and the fraction of SF_6 destroyed in time at different altitudes are presented in figure 6.7.

For all altitudes, the fraction of SF_6 destroyed approaches some limiting value while the density of free electrons approaches zero at about the same speed. Surprisingly, even though the electron densities vary by ten orders of magnitude and the air density by five, the fractions of SF_6 destroyed are all of the same order of magnitude, ranging between $1.2 - 1.8\%$ of the initial SF_6 density. To understand this better, we turn to an analytical approximation of what is happening.

6.4.3 Analytical approximation

Here we present an analytical solution of the 0D model that includes impact ionization and electron attachment, but not electron ion recombination and electron detachment. Ion conversion is negligible if there is no electron detachment.

The density of SF_6 in a gas as affected by a streamer discharge can be estimated as follows, if recombination and detachment are neglected, where recombination is negligible at low air densities.

The electron density inside the channel evolves according to the equation

$$\partial_t n_e = \nabla \cdot \mathbf{j}_e - k_a \, n_{O_2} \, n_e - k_{SF_6} \, n_{SF_6} \, n_e \tag{6.9}$$

where k_a is the electron attachment rate coefficient. Since $n_{SF_6} \ll n_{O_2}$,

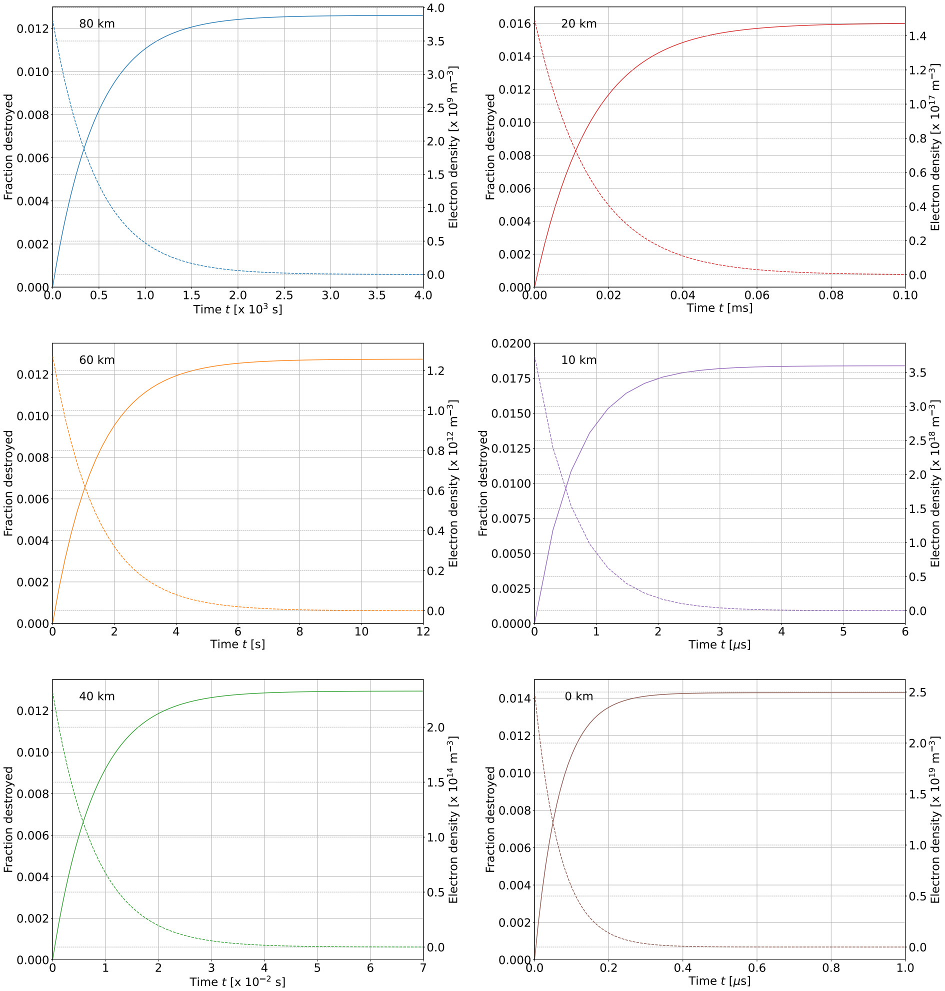

Figure 6.7: Fraction (6.8) of SF_6 destroyed (solid lines) and electron density (dashed lines) on longer times at different altitudes, according to the 0D ZDPlasKin model.

we neglect the effect of attachment of electrons to SF$_6$ to the evolution of electron density. Neglecting the spatial structure as well leaves us with

$$\partial_t n_e = -k_a \, n_{O_2} \, n_e, \tag{6.10}$$

which has the solution

$$n_e(t) = n_e(0) \, e^{-t/T_O}, \tag{6.11}$$

where $n_e\,(0)$ is the initial electron density and $T_O = 1/(k_a n_{O_2})$ is the electron attachment time to oxygen for a given electric field and oxygen number density.

The SF$_6$ density n_{SF_6} evolves in time as

$$\partial_t n_{SF_6} = -k_{SF_6} \, n_{SF_6} \, n_e. \tag{6.12}$$

By inserting (6.11), the equation can be solved as

$$n_{SF_6}(t) = n_{SF_6}(0) \exp\left[-\frac{T_O}{T_S}\left(1 - e^{-t/T_O}\right)\right], \tag{6.13}$$

where $n_{SF_6}(0)$ is the initial SF$_6$ density and $T_S = 1/(k_{SF_6} n_e(0))$ is the SF$_6$ destruction time.

The previous expression reduces to

$$n_{SF_6}(t) \longrightarrow n_{SF_6}(0) \, e^{-T_O/T_S} \qquad \text{for } t \to \infty, \tag{6.14}$$

meaning that the fraction of SF$_6$ destroyed depends on the ratio of electron attachment to oxygen to destructive electron collision with SF$_6$, or more precisely on

$$\frac{T_O}{T_S} = \frac{k_{SF_6} \, n_e(0)}{k_a \, n_{O_2}}. \tag{6.15}$$

6.4.4 Evaluation of 0D model and dependence on air density

We now return to the numerical solution of the 0D model, that includes ion electron recombination, ion conversion and electron detachment. But we will see that the analytical approximation of the last section is helpful in understanding.

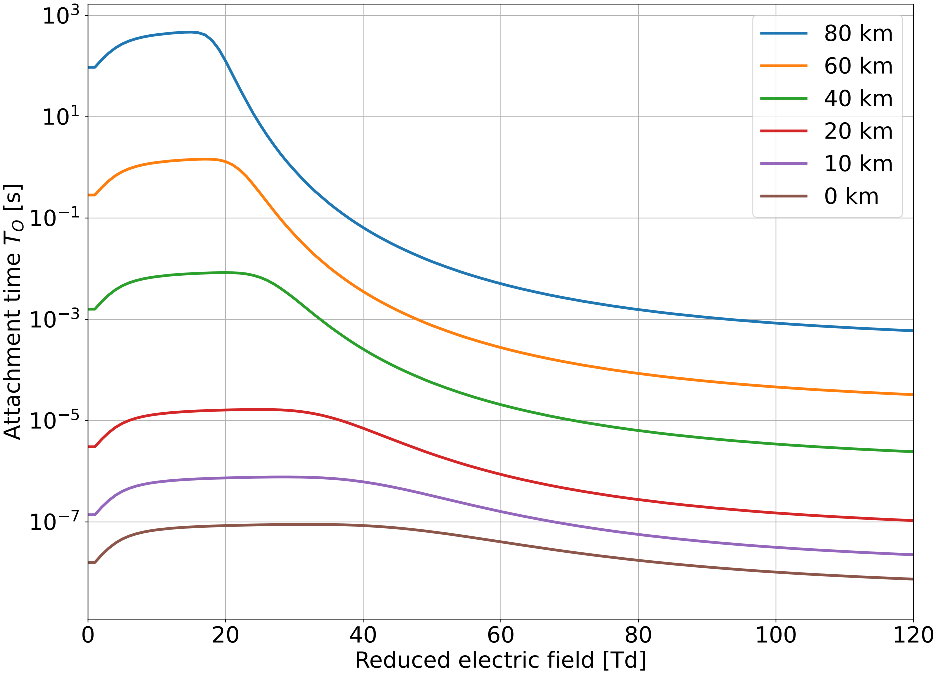

Figure 6.8: Electron attachment time to oxygen molecules at different altitudes as a function of the reduced electric field.

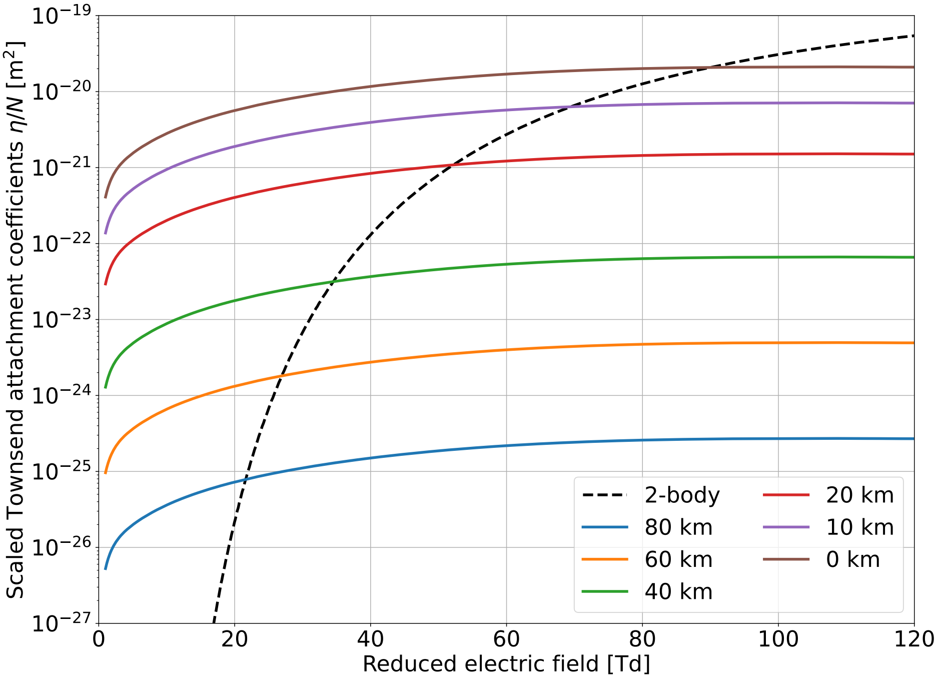

Figure 6.9: Scaled Townsend 3-body attachment coefficients at different altitudes as a function of the reduced electric field. The dashed line stands for the Townsend 2-body attachment coefficient, which is the same for all altitudes.

Table 6.3: Results of 0D simulations at different altitudes in the indicated electric fields. These fields occur in the channel of streamers propagating in background fields of 58.8 Td and 98 Td.

Altitude	Electric field [Td]	Fraction destroyed
80 km	30.26	0.964 %
60 km	30.34	0.818 %
40 km	30.48	0.835 %
20 km	45.65	1.39 %
	26.57	1.09 %
10 km	38.99	1.62 %
	21.99	1.24 %
0 km	34.27	1.99 %
	18.38	1.07 %

In figure 6.7, we see that final fractions of SF_6 destroyed are of the same order and do not scale with the gas density. This is because T_S scales as $1/N^2$, due to its electron density term, and T_O, in the electric field range that we tried, also scales by $1/N^2$; so these two dependencies cancel each other. Figure 6.8 shows us the different attachment times at different altitudes as a function of the electric field, and at less than 30 Td, the difference between 0 km and 80 km is in the order of $10^{10} \approx (N_0/N)^2$. This is because in this field region, three-body electron attachment to oxygen still dominates over two-body electron attachment. This can be seen in figure 6.9, we can see that despite the attachment three-body attachment coefficient getting lower with decreasing gas density, at low fields it still dominates over two-body attachment. It is mainly the electric field range where three-body attachment dominates that is getting shorter with decreasing gas density.

The electron attachment time T_O does not scale as $1/N^2$ in all electric fields, and thus if we use some sample electric field values given by the streamers in background fields of 98 Td and 58.8 Td, we expect a different set of results. Table 6.3 lists the fraction destroyed of SF_6 at the minimum electric field values in the streamer channels in higher background electric fields.

At higher electric fields, T_O scales as $1/N$ so the ratio T_O/T_S now scales as N. Following equation (6.14), the final SF_6 density would be smaller for larger gas densities. We can see this in the results starting for fields above 30 Td presented in table 6.3, where the largest fractions destroyed are observed in the simulations at the lower altitudes.

From 40 km and above, our 0D simulations using electric fields above 50 Td resulted to the growth of electron density. Electron attachment and detachment occur at comparable rates and cancel each other, leaving the dominant reaction to be the ionization reaction. Electron growth in streamers in low density regions have already been reported in [82]. For these cases, there will always be free electrons available for SF_6 destruction, and thus, the SF_6 fraction destroyed only depends on how long the simulation is left to run.

6.5 Results on CF_4 destruction in the simulated streamers

Another potent greenhouse gas is carbon tetrafluoride (CF_4), which has a lifetime of about 50000 years and a 100-year global warming potential of 6630. It is released during primary aluminum production and is used in semiconductor and electronics manufacture [88]. In 2016, it had a global mean concentration of 82.7 ppt [116].

We also included CF_4 in our simulations to check how streamers contribute to their destruction in the atmosphere. Destruction pathways for CF_4 that we included involve ionization, attachment, and neutral dissociation reactions. We got the cross sections for these reactions from [29]. In experiments, only products of dissociative attachment reactions to CF_4 were observed between 0-10 eV - F^- and CF_3^-. CF_4^- was not observed [53]. Since we are focused on the reactions in the streamer channel, it is safe to assume that all attachment reactions are dissociative there.

Figure 6.10 shows the fraction of CF_4 destroyed at the same fixed points used in figures 6.5 and 6.6 as a function of scaled time. We see the same effect of varying air densities to the fraction of CF_4 destroyed - there is a higher destruction rate at higher air densities. For the 21.6 Td and 58.8 Td streamers, there is a linear increase of the fraction of CF_4 destroyed in time.

Figure 6.11 shows the reaction rate coefficients of the different CF_4 reactions. The dominant destruction mechanism for CF_4 is dissociative

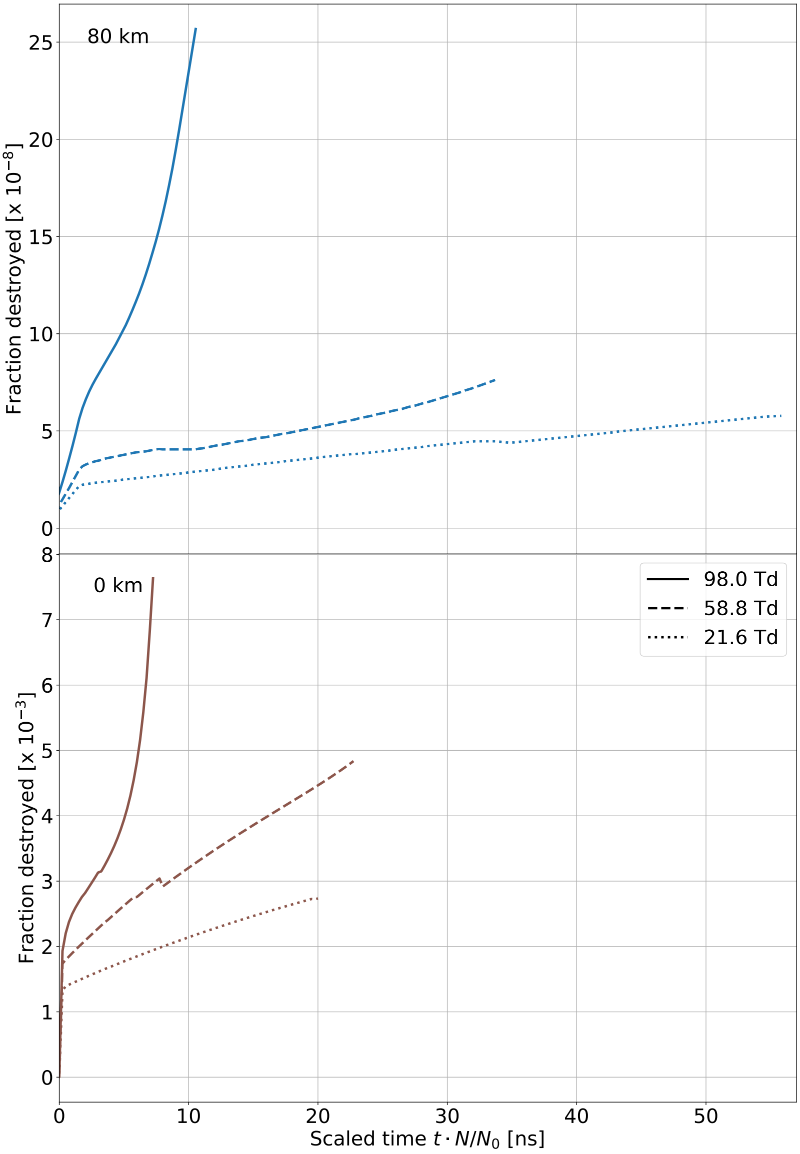

Figure 6.10: Fraction of destroyed CF_4 at a fixed point in the domain as a function of scaled time at 0 and 80 km altitudes. Streamers in different background fields are indicated by solid, dashed, and dotted lines. The lines end when the streamers have crossed 75% of the domain.

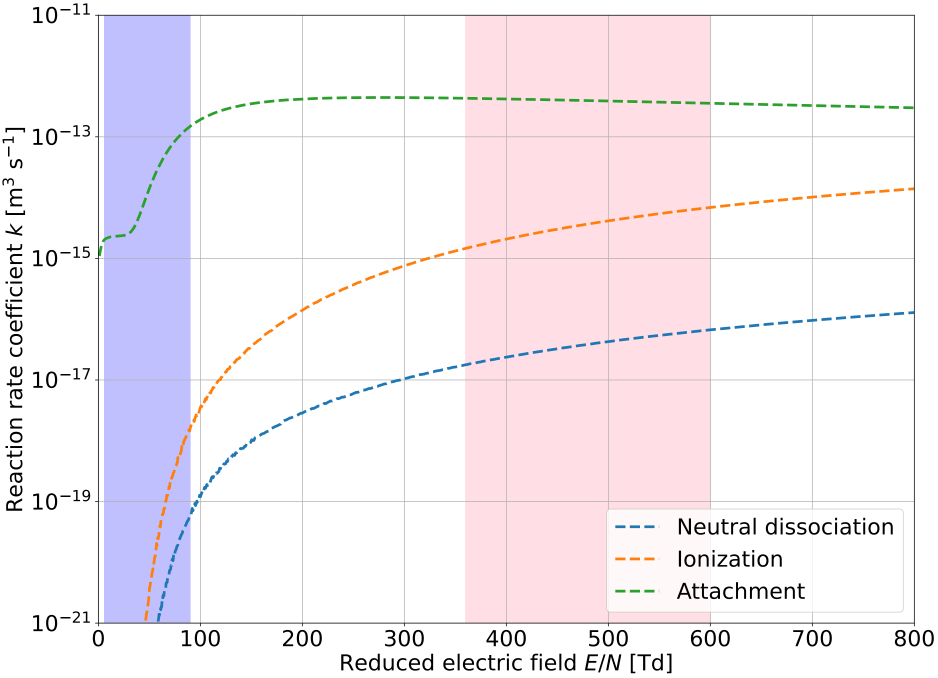

Figure 6.11: Reaction rate coefficients of included CF_4 reactions as a function of the reduced electric field E/N. The blue region around 6 - 90 Td represents the electric field range inside streamer channels while the red region from 360 - 600 Td represents the range of enhanced electric fields at the streamer head.

electron attachment for all observed electric fields in our simulations. The reaction rate coefficient for this reaction is about 1.09×10^{-15} m^3 s^{-1} at around 1 Td and increases with increasing electric field in the electric field range of streamer channels (i.e. blue region in the figure). The increase in this rate coefficient is steep from 30 Td to 90 Td, and since the electric field at the fixed points we observed for the 98 Td streamers increased within this range (bottom left panel of figure 6.5), the fraction of CF_4 destroyed also shows a steep profile for the 98 Td streamers.

For CF_4, electron attachment gets less likely if there is no electric field, while electron attachment to SF_6 proceeds even without an electric field. In the low field region, the reaction rate coefficient for electron attachment to CF_4 is increasing while k_{SF_6} is decreasing, and electron attachment to CF_4 gets a higher reaction rate than k_{SF_6}. Thus, in the same simulated timescale, the streamers destroyed more CF_4 than SF_6. Extending these simulations using a 0D model showed that CF_4 density decays to nearly zero in the channel of a single streamer within timescales that depend on the channel electric field.

6.6 Conclusions and Outlook

6.6.1 Conclusions on single streamers

We simulated positive streamers in air at different gas densities to investigate the contribution of streamers to SF_6 destruction at different altitudes. These are our conclusions:

(a) We have demonstrated how well streamers in different electric fields scale with air density, from tropospheric to mesospheric altitude (from 0 to 80 km), and we have studied the corrections to scaling. This was the starting point to analyze SF_6 destruction in atmospheric streamer discharges at different altitudes.

(b) We had expected that electrons with energies in the eV range in the enhanced electric field at the streamer head would contribute significantly to SF_6 destruction, but that is not the case. Rather the free electrons liberated in the discharge cool down and then they can attach either to oxygen or to SF_6. Attachment to SF_6 is mostly dissociative

$$e + SF_6 \rightarrow SF_5^- + F,$$

and hence SF_6 is destroyed in this reaction. This happens in the streamer channel and further behind and depends on the local electrical field.

(c) SF_6 destruction is limited due to the competition of electron attachment either to oxygen or to SF_6. Attachment to oxygen is faster, and SF_6 destruction decreases while the electrons are being depleted.

(d) Surprisingly, while air density N varies by 5 orders of magnitude and the degree of ionization in the streamer by 10 orders, the fraction of SF_6 destroyed within one streamer is always between 1 and 2 % if the local reduced electric field E/N is below 20 Td. For higher fields, the fraction destroyed increases with increasing air density.

6.6.2 Outlook on how to estimate the global impact

Here we have analyzed single streamer discharges, but streamers almost never come alone. For example, sprite discharges in the mesosphere above thunderstorms can be seen to consist of ten thousands of streamer channels. These streamers do not turn into hotter leader channels as they would at lower altitudes, because the ionization density is too low.

For electric discharges in and near thunderclouds, the attention has shifted in the past decades from the visible and rather thermalized return strokes between cloud and ground to fast and extended phenomena in the cloud that can be detected by the emitted radio waves and by multiply scattered light from within the cloud. Intracloud discharges can stretch over distances exceeding 750 km in the horizontal direction within a cloud, and radio observations with the precision of meters measure fast local processes that must be bursts of streamer coronas paving the way of hotter leader channels. A wide range of dynamic discharge phenomena within thunderstorms is currently under investigation, also optically from space as far as the discharge light scattered within the cloud can be observed from above.

The essential input for an estimate of SF_6 or CF_4 destruction is the rate of electron liberation within thunderstorms globally. According to our analysis, relevant electron numbers are generated in the high field zones at the streamer heads which occur as a rule in the early stage of any discharge, or when ever a discharge penetrates a new region in space. The electrons then later attach to oxygen, or they experience dissociative attachment to SF_6 or CF_4 in the low electric fields behind streamer heads. Here it should be noted that the streamer phase is particular efficient in transforming electric energy into ionization [97], and streamers are used in multiple technological applications for that reason. Hence to develop an estimate for electron liberation rates in thunderstorms complements the present study, and this estimate is an important goal for the future.

To apply our results to atmospheric chemistry, in the following step the number and occurrence rate of atmospheric streamer discharges has to be estimated. This can be based on observations of light emissions for sprites and intracloud discharges. The reason is that light emission is roughly proportional to the density of liberated electrons. Another estimate could be based on energy balances if we understand which fraction of the thunderstorm energy goes into streamer discharges, and which fraction of streamer energy goes into electron liberation. A view on the energy branching within streamers is given, e.g., in [52].

The analysis applies not only to streamers, but to any other electron concentrations in air, like in lightning leaders and return strokes. However, for leaders and return strokes, also more plasma chemistry and heat should be taken into account.

Our approach is not limited to SF_6 and CF_4, but it can be extended to other contaminants in the atmosphere.

Part III

Conclusions and References

Chapter 7

Conclusions and outlook

In the course of this thesis, we studied positive streamers in air in homogeneous electric fields. We investigated the effects of enhanced electron attachment and looked at how streamers behave in different background electric fields. Different streamer propagation behaviors were found, and we described how these relate with processes affecting the streamer channel conductivity.

From our observations, we were able to identify a special case of streamer propagation, and based on which, we proposed analytical approximations for some streamer properties. The use of these approximations would enormously reduce the computational load of streamer simulations.

We also looked at how different streamers affect minor chemical species in their environment - specifically, how streamers contribute to SF_6 destruction in the atmosphere. For this purpose, streamers at different gas densities were examined, and we analyzed how the different conditions lead to different SF_6 destruction outcomes.

This last chapter features our conclusions and suggests ways to forward our research.

7.1 Summary of findings

Streamer channel conductivity

Our studies led us to gain a better understanding of the role of the channel conductivity on the streamer propagation behavior.

Even after increasing the rate of electron attachment inside the streamer channel to the point that electrons are rapidly getting depleted in that region, we still observed propagating streamers. This shows us that a streamer needs not to be conducting all the way to the electrode to keep propagating. In such cases, we only observe significant electron densities in a limited length behind the streamer head. Afterwards, the electron density decreases by some orders of magnitude. We do not observe electric field screening at the non-conducting part of the streamer channel, and the electric field reverts back to the applied background field value.

The same phenomena was observed in streamers in low background electric fields. Applying a low background field resulted to a loss of channel conductivity by slowing streamer propagation down to timescales where electron-loss reactions start to have significant effects. For these streamers, it's not only electron attachment that reduced the electron density in the channel, but electron recombination to O_4^+ was consequential as well. These two electron-consuming reactions have comparable rates in the observed fields inside the channels of our low-background-field streamers, both taking about 25 ns to occur for a streamer in a 4.65 kV/cm background field at 1 bar. Even if we look at streamers in higher background electric fields, recombination only takes about 10 ns longer than attachment on average, albeit both processes are negligible in these cases due to the streamer crossing the gap faster than these reactions could occur.

Streamer propagation regimes

Our parameter studies revealed three kinds of streamer propagation behaviour. All three could be found by changing either the electron attachment rate or the background electric field. There were (1) accelerating streamers, (2) decelerating streamers, and (3) steady streamers. We saw these cases when either the attachment rate is high enough or the background electric field is sufficiently low.

Most streamer simulations presented in literature feature **accelerating streamers**. As its name implies, these streamers gain speed as they propagate. As these streamers accelerate, the streamer heads grow wider. Accelerating streamers are easy to obtain in simulations and were found in the largest range of parameters we looked at. Of the three different propagation modes, they are the easiest to initiate and least likely to branch. Accelerating streamers showed no signs of slowing down or stagnation in the timescales we've explored, and their long-time behavior could only be inferred as of the moment.

Decelerating streamers were found in cases where either the electron attachment rate in the streamer channel was too high or the background electric field was very low. Their slowing down behavior is accompanied by a decrease in the streamer radius and an increase in the field enhancement at the streamer tip. The higher electric field yields higher electron densities behind the streamer ionization front, but these electrons are only observed in a limited length behind the streamer head as they are quickly lost in the streamer channel. Some of the decelerating streamers we found slowed down to stagnation and didn't completely cross our simulation domain.

Steady streamers

The third parameter regime is that of the **steady streamer** or a uniformly-propagating streamer. Such a streamer maintains its shape as it propagates, neither growing in radius or changing in terms of the charge density it carries. Steady streamers feature a non-conductive streamer channel, same as decelerating streamers, with an electrically-decoupled streamer head from the electrode. Far behind the head of a steady streamer, the electric field is equal to the background field. This makes the streamer propagate akin to a fixed charge moving in a medium with an applied electric field. It leaves no electric charge behind and carries a fixed amount of charge along. A steady streamer is one example of a streamer that kept propagating indefinitely despite losing channel conductivity.

Observable properties such as the optical radius and the velocity of the steady streamer in our simulations agree well with measurements of the thinnest and slowest propagating streamers experimentally observed.

Since the streamers we examined were positive streamers, their velocities are not limited by the electron drift velocity. We found steady streamers that have velocities an order of magnitude smaller than the electron drift velocity in the streamers' maximum electric field.

The steady streamer provided us with a better understanding of how streamer stability fields work. As long as the streamer transports a fixed amount of charge, it would continue to propagate in a given uniform electric field.

Steady streamers are very difficult to obtain as (i) streamers fail to initiate in low background fields and even if they do, (ii) these streamers are very prone to branching. Furthermore, they are (iii) very sensitive to the initial conditions.

Analytical approximations

From the analysis of steady streamers, we developed a semi-analytical model by approximating the electron dynamics in the different regions of the streamer head and using conservation laws. The width of the charge layer, the electric field at the streamer tip and in the streamer channel, and the ionization degree can be calculated using analytical relations given the streamer radius, velocity, length, and the background electric field.

The values we get using the analytical expressions match our numerical simulations well. The approximations were tested on both steady streamers and accelerating streamers, and better agreement was found when looking at steady streamers. Steady streamer properties deviate only by 30% at most from their simulation counterparts, while accelerating streamers have deviations up to 60%.

Streamer parameter dependencies

We noted certain patterns between some streamer parameters and the background electric field.

Consistently for all simulations, the minimum electric field in the streamer channel decreases with decreasing background electric field. Low electric fields are conducive to electron attachment and electron recombination. Given that the electric fields in their channels are lower combined with their slower propagation speed (thus there is more time for electron loss at a given length), streamers at low background electric fields often have non-conducting channels.

The relationship between the maximum electric field at the streamer head and the background electric field was found to be non-monotonic. In one set of simulations in air, we observed the maximum electric field to have a minimum value at a background field of 12 kV/cm, while another set had the minimum at 6 kV/cm for the same gas. There is no reason why the same minimum would always be observed, and different transport parameters, initial conditions, and streamer lengths can account for the difference in the intermediate background fields where the minimum value was found.

SF_6 destruction

Our survey of streamers at different altitudes showed overall scaling with air density and some deviations from density scaling. In particular, corrections for photoionization quenching and three-body reactions are needed in cases of high gas densities.

Streamer contributions to SF_6 destruction are dominated by reactions that involve the electrons in the streamer channel and not by the electrons in the streamer tip. The high energy electrons produced in the active zone do not contribute much to SF_6 destruction as the electron density in this region is not large enough. Electron density only grows to a significant order once the ionization front has passed and the electrons get to the region where the electric field is largely screened.

The reaction that contributes most to SF_6 destruction is the electron attachment reaction that produces SF_5^-, which has an increasing reaction rate as the electric field decreases. The fraction of SF_6 destroyed depends on the competition between this electron attachment reaction and electron attachment to oxygen.

For electric fields below 20 Td, there is a different scaling relation observed in the fraction destroyed of SF_6 at different gas densities. This is because in low electric fields, even at low gas densities, three-body electron attachment to oxygen always dominates over two-body electron attachment to the same molecule, and the increase in attachment time to oxygen in low gas densities is equally compensated by the increase in attachment to SF_6 due to low electron densities.

At particular electric fields in high altitudes, about 40 km and higher, electron detachment reaction from O^- releases free electrons back to the domain, and SF_6 destruction simply depends on the timescale considered, as there will always be electrons available for attachment reactions.

Other conclusions

The slower streamers we observed ran for hundreds of nanoseconds, and this longer timescale opened the possibility that ion motion and streamer gas heating are no longer negligible.

Comparing cases with and without ion motion revealed that even for a streamer with velocities in the order of 10^4 m/s observed for 400 ns, ion motion is still inconsequential. Including ion motion slows down a streamer by only 10 % while increasing the maximum electric field by 5 %. Additionally, the positive charges that compose the charge layer drift following the electric field direction, causing the layer to be slightly thicker.

We estimated an upper threshold for streamer contributions to gas heating, and we calculated only a 6 K increase in gas temperature after 400 ns. This was done under the assumption that all deposited energy is converted into heat. Energy deposition by electrons is dependent on the distance the electrons travel, and in our simulations, the electrons propagate only a short distance before they attach or recombine, resulting to only a small deposited energy to the system.

7.2 Future work

In this final section we list possible avenues to continue the research presented in this book.

The behavior of accelerating streamers on longer timescales still needs to be studied. Streamer branching could be expected, and thus the inclusion of stochastic photoionization might be helpful for more realistic results [146]. The chemistry set may also need to be expanded, as reactions that were previously considered negligible may now prove to introduce effects at longer timescales [52]. Such an expansion may entail the inclusion of rotational, vibrational, and electron excitation reactions.

Since decelerating streamers featured very high electric field enhancement in a limited region, it may prove useful to investigate them using particle model. Such a step would remove the need to use the local field approximation, which might be failing us in this scenario. A particle model could provide a better picture of what is happening in these smaller streamers and shed light into the stagnation dynamics of streamers.

A study of the charge distribution behind the ionization front of a decelerating streamer could also provide additional insights into the dynamics of streamer stagnation.

Steady streamer research has already been extended to find that there is no unique electric field in air where uniformly-propagating behaviour could only be observed in. Instead, with different streamer velocities and head radii, a streamer can propagate with a constant velocity at different background fields [75]. The same discovery was found for negative streamers [51]. It should be possible to find steady streamers in other gases as well, given that these gases have electron-loss processes that run within relevant timescales.

On top of looking at steady streamers, how our other discoveries - the different propagation regimes, parameter dependencies, and analytical approximations - appear in other gases is also worth investigating.

Another open question is how and when steady streamers form in background fields with a spatial gradient, as is common in experiments. An inhomogenous background field could be implemented in computational domains by using point charges instead of fixing the electric potential on the boundaries. Inhomogenous gas densities could also be looked at.

The agreement between the steady streamer we found in air and the minimal streamer properties is still an open question.

Improvements on the agreement between the analytical approximations presented here and simulation models is to be worked on. To move forward, the effects of a curved charge layer could be incorporated, along with better estimations of the electron dynamics in the streamer channel.

Streamers do not naturally exist as just one single channel but in the form of complicated, branched trees. In such morphology, these multiple streamer channels interact and affect each other. We should extend our investigations to such structures. The analytical approximations discussed in this thesis models a single streamer channel but it should be possible to extend it to get a reduced-model applicable for streamer trees. Ultimately, we want to model multi-streamer discharges within reasonable computing times.

Scaling laws where three-body reactions dominate could be developed. We found a N^2 scaling for time for this regime, but further investigation is still necessary. The density profiles of different species inside streamer channels when following this different scaling relation could be inspected as it could lead to different insights.

The investigation on the destruction of SF_6 by atmospheric streamers could be extended by coupling simulation results with observations, and estimating how much of the SF_6 concentration is reduced by recorded atmospheric electricity events. This could possibly be done by looking at the optical emissions of these events and relating that with the expected optical emissions of single streamer channels.

Although we observed an increase in the effect of streamer gas heating and ion motion when we looked at slower streamers and longer timescales, the effect remained negligible. It would be useful to identify when precisely these effects start to be consequential, and this might aid in streamer-to-leader-transition research.

The effects of humidity to streamer behaviour are still to be explored.

Bibliography

[1] Phelps database, `www.lxcat.net`, retrieved March 2019.

[2] I Adamovich, S D Baalrud, A Bogaerts, P J Bruggeman, M Cappelli, V Colombo, U Czarnetzki, U Ebert, J G Eden, P Favia, and et al. The 2017 plasma roadmap: Low temperature plasma science and technology. *Journal of Physics D: Applied Physics*, 50(32):323001, July 2017.

[3] A Agnihotri, W Hundsdorfer, and U Ebert. Modeling heat dominated electric breakdown in air, with adaptivity to electron or ion time scales. *Plasma Sources Science and Technology*, 26(9):095003, August 2017.

[4] N L Aleksandrov and E M Bazelyan. Ionization processes in spark discharge plasmas. *Plasma Sources Science and Technology*, 8(2):285–294, January 1999.

[5] N L Allen and M Boutlendj. Study of the electric fields required for streamer propagation in humid air. *Science, Measurement and Technology, IEE Proceedings A*, 138:37 – 43, 02 1991.

[6] N L Allen and A Ghaffar. The conditions required for the propagation of a cathode-directed positive streamer in air. *Journal of Physics D: Applied Physics*, 28(2):331–337, February 1995.

[7] L L Alves. The ist-lisbon database on lxcat. *Journal of Physics: Conference Series*, 565(1):012007, December 2014.

[8] Wladimir An, Kurt Baumung, and Hansjoachim Bluhm. Underwater streamer propagation analyzed from detailed measurements of pressure release. *Journal of Applied Physics*, 101(5):053302, Mar 2007.

[9] James G Anderson and T M Donahue. The neutral composition of the stratosphere and mesosphere. *Journal of Atmospheric and Terrestrial Physics*, 37(6):865–884, 1975.

[10] N Yu Babaeva and G V Naidis. Two-dimensional modelling of positive streamer dynamics in non-uniform electric fields in air. *Journal of Physics D: Applied Physics*, 29(9):2423–2431, September 1996.

[11] N Yu Babaeva and G V Naidis. Dynamics of positive and negative streamers in air in weak uniform electric fields. *IEEE Transactions on Plasma Science*, 25(2):375–379, 1997.

[12] Natalia Yu Babaeva and George V Naidis. Universal nature and specific features of streamers in various dielectric media. *Journal of Physics D: Applied Physics*, 54(22):223002, 6 2021.

[13] Behnaz Bagheri and Jannis Teunissen. The effect of the stochasticity of photoionization on 3D streamer simulations. *Plasma Sources Science and Technology*, 28(4):045013, 4 2019.

[14] Behnaz Bagheri, Jannis Teunissen, U. Ebert, M. M. Becker, S. Chen, O. Ducasse, O. Eichwald, D. Loffhagen, Alejandro Luque, D. Mihailova, J. M. Plewa, Jan van Dijk, and M. Yousfi. Comparison of six simulation codes for positive streamers in air. *Plasma Sources Science and Technology*, 27(9):095002, 9 2018.

[15] Behnaz Bagheri, Jannis Teunissen, and Ute Ebert. Simulation of positive streamers in CO2 and in air: the role of photoionization or other electron sources. *Plasma Sources Science and Technology*, 29(12):125021, December 2020.

[16] Behnaz Bagheri, Jannis Teunissen, Ute Ebert, Markus M Becker, She Chen, Olivier Ducasse, Olivier Eichwald, Detlef Loffhagen, Alejandro Luque, Diana Mihailova, et al. Comparison of six simulation codes for positive streamers in air. *Plasma Sources Science and Technology*, 27(9):095002, 2018.

[17] Ladislav Bárdos and Hana Baránková. Cold atmospheric plasma: Sources, processes, and applications. *Thin Solid Films*, 518(23):6705–6713, 2010.

[18] K H Becker, U Kogelschatz, K H Schoenbach, and R J Barker. *Non-equilibrium air plasmas at atmospheric pressure.* CRC press, 2004.

[19] A Bourdon, V P Pasko, N Y Liu, S Célestin, P Ségur, and E Marode. Efficient models for photoionization produced by non-thermal gas discharges in air based on radiative transfer and the Helmholtz equations. *Plasma Sources Sci. Technol.*, 16(3):656–678, 2007.

[20] Dennis Bouwman, Jannis Teunissen, and Ute Ebert. 3D particle simulations of positive air–methane streamers for combustion. *Plasma Sources Science and Technology*, 31(4):045023, 4 2022.

[21] T M P Briels, J Kos, E M van Veldhuizen, and U Ebert. Circuit dependence of the diameter of pulsed positive streamers in air. *Journal of Physics D: Applied Physics*, 39(24):5201–5210, December 2006.

[22] T M P Briels, J Kos, G J J Winands, E M van Veldhuizen, and U Ebert. Positive and negative streamers in ambient air: measuring diameter, velocity and dissipated energy. *J. Phys. D: Appl. Phys.*, 41(23):234004, 2008.

[23] Will J Brigg, Jonathan Tennyson, and Martin Plummer. R-matrix calculations of low-energy electron collisions with methane. *Journal of Physics B: Atomic, Molecular and Optical Physics*, 47(18):185203, September 2014.

[24] Peter Bruggeman and Ronny Brandenburg. Atmospheric pressure discharge filaments and microplasmas: physics, chemistry and diagnostics. *Journal of Physics D: Applied Physics*, 46(46):464001, 2013.

[25] Peter J Bruggeman, Felipe Iza, and Ronny Brandenburg. Foundations of atmospheric pressure non-equilibrium plasmas. *Plasma Sources Science and Technology*, 26(12):123002, 2017.

[26] W H Brune, P J McFarland, E Bruning, S Waugh, D MacGorman, D O Miller, J M Jenkins, X Ren, J Mao, and J Peischl. Extreme

oxidant amounts produced by lightning in storm clouds. *Science*, 372(6543):711–715, 2021.

[27] M Bujotzek, M Seeger, F Schmidt, M Koch, and Christian Franck. Experimental investigation of streamer radius and length in sf6. *Journal of Physics D: Applied Physics*, 48(24):245201, 2015.

[28] L. G. Christophorou and J. K. Olthoff. Electron interactions with sf6. *Journal of Physical and Chemical Reference Data*, 29(3):267–330, 2000.

[29] L. G. Christophorou, J. K. Olthoff, and M. V. V. S. Rao. Electron interactions with cf4. *Journal of Physical and Chemical Reference Data*, 25(5):1341–1388, 1996.

[30] Loucas G Christophorou and Isidor Sauers. *Gaseous dielectrics VI*. Springer, 2013.

[31] J S Clements, A Mizuno, W C Finney, and R H Davis. Combined removal of SO, NO_x, and fly ash from simulated flue gas using pulsed streamer corona. *IEEE Trans. on Ind. Applicat.*, 25(1):62–69, 1989.

[32] Vernon Cooray, Mahbubur Rahman, and Vladimir Rakov. On the nox production by laboratory electrical discharges and lightning. *Journal of Atmospheric and Solar-Terrestrial Physics*, 71(17):1877–1889, 2009.

[33] Steven A. Cummer, Nicolas Jaugey, Jingbo Li, Walter A. Lyons, Thomas E. Nelson, and Elizabeth A. Gerken. Submillisecond imaging of sprite development and structure. *Geophysical Research Letters*, 33(4), 2006.

[34] Siebe Dijcks, Martijn van der Leegte, and Sander Nijdam. Imaging and reconstruction of positive streamer discharge tree structures. *Plasma Sources Science and Technology*, 32(4), 4 2023.

[35] G. Diniz, C. Rutjes, U. Ebert, and I. S. Ferreira. Cold electron runaway below the friction curve. *Journal of Geophysical Research: Atmospheres*, 124(1):189–198, 2019.

[36] MI Dyakonov and V Yu Kachorovskii. Theory of streamer discharge in semiconductors. *Sov. Phys. JETP*, 67(5):1049–1054, 1988.

[37] MI D'yakonov and VY Kachorovskii. Streamer discharge in a homogeneous field. *Zh. Eksp. Teor. Fiz*, 95(May):1850–1859, 1989.

[38] U. Ebert, Sander Nijdam, Chao Li, Alejandro Luque, Tanja Briels, and Eddie van Veldhuizen. Review of recent results on streamer discharges and discussion of their relevance for sprites and lightning. *Journal of Geophysical Research*, 115, 2010.

[39] Hani Francisco, Behnaz Bagheri, and Ute Ebert. Electrically isolated propagating streamer heads formed by strong electron attachment. *Plasma Sources Science and Technology*, 30(2):025006, February 2021.

[40] Hani Francisco, Jannis Teunissen, Behnaz Bagheri, and Ute Ebert. Simulations of positive streamers in air in different electric fields: steady motion of solitary streamer heads and the stability field. *Plasma Sources Science and Technology*, 30(11):115007, November 2021.

[41] A Fridman, A Chirokov, and A Gutsol. Non-thermal atmospheric pressure discharges. *Journal of Physics D: Applied Physics*, 38(2):R1–R24, Jan 2005.

[42] Gregory Fridman, Gary Friedman, Alexander Gutsol, Anatoly B. Shekhter, Victor N. Vasilets, and Alexander Fridman. Applied Plasma Medicine. *Plasma Process. Polym.*, 5(6):503–533, 2008.

[43] L S Frost and A V Phelps. Rotational excitation and momentum transfer cross sections for electrons in h_2 and n_2 from transport coefficients. *Phys. Rev.*, 127:1621–1633, September 1962.

[44] Gallimberti, I. The mechanism of the long spark formation. *J. Phys. Colloques*, 40(C7):C7–193–C7–250, 1979.

[45] Lingge Gao, Xingmin Shi, and Xili Wu. Applications and challenges of low temperature plasma in pharmaceutical field. *Journal of Pharmaceutical Analysis*, 11(1):28–36, 2021.

[46] F J Gordillo-Vázquez. Air plasma kinetics under the influence of sprites. *J. Phys. D: Appl. Phys.*, 41(23):234016, 2008.

[47] L R Grabowski, E M van Veldhuizen, A J M Pemen, and W R Rutgers. Corona Above Water Reactor for Systematic Study of Aqueous Phenol Degradation. *Plasma Chemistry and Plasma Processing*, 26(1):3–17, 2006.

[48] David B Graves. Low temperature plasma biomedicine: A tutorial review. *Physics of Plasmas*, 21(8):080901, 2014.

[49] R. F. Griffiths and J. Latham. Electrical corona from ice hydrometeors. *Quarterly Journal of the Royal Meteorological Society*, 100(424):163–180, 1974.

[50] R F Griffiths and C T Phelps. The effects of air pressure and water vapour content on the propagation of positive corona streamers, and their implications to lightning initiation. *Quarterly Journal of the Royal Meteorological Society*, 102(432):419–426, 1976.

[51] Baohong Guo, Xiaoran Li, Ute Ebert, and Jannis Teunissen. A computational study of accelerating, steady and fading negative streamers in ambient air. *Plasma Sources Science and Technology*, 31(9):095011, September 2022.

[52] Baohong Guo and Jannis Teunissen. A computational study on the energy efficiency of species production by single-pulse streamers in air. *Plasma Sources Science and Technology*, 32(2):025001, February 2023.

[53] Gennady L. Gutsev and Ludwik Adamowicz. The structure of the CF4 anion and the electron affinity of the CF4 molecule. *The Journal of Chemical Physics*, 102(23):9309–9314, 06 1995.

[54] G J M Hagelaar and L C Pitchford. Solving the Boltzmann equation to obtain electron transport coefficients and rate coefficients for fluid models. *Plasma Sources Science and Technology*, 14(4):722–733, 2005.

[55] B. M. Hare, O. Scholten, J. Dwyer, U. Ebert, S. Nijdam, A. Bonardi, S. Buitink, A. Corstanje, H. Falcke, T. Huege, J. R. Hörandel, G. K. Krampah, P. Mitra, K. Mulrey, B. Neijzen, A. Nelles, H. Pandya, J. P. Rachen, L. Rossetto, T. N.G. Trinh, S. Ter Veen, and T. Winchen. Radio Emission Reveals Inner Meter-Scale Structure of Negative Lightning Leader Steps. *Physical Review Letters*, 124(10), 3 2020.

[56] M. Iio, M. Goto, H. Toyoda, and H. Sugai. Relative cross sections for electron-impact dissociation of sf6 into sfx (x = 13) neutral radicals. *Contributions to Plasma Physics*, 35(4-5):405–413, 1995.

[57] Georg Isbary, Tetsuji Shimizu, Yang-Fang Li, Wilhelm Stolz, Hubertus M Thomas, Gregor E Morfill, and Julia L Zimmermann. Cold atmospheric plasma devices for medical issues. *Expert Review of Medical Devices*, 10(3):367–377, 2013.

[58] Yukikazu Itikawa. Cross sections for electron collisions with nitrogen molecules. *Journal of physical and chemical reference data*, 35(1):31–53, 2006.

[59] Yukikazu Itikawa. Cross sections for electron collisions with oxygen molecules. *Journal of Physical and Chemical Reference Data*, 38(1):1–20, 2009.

[60] Tobias G Klämpfl, Georg Isbary, Tetsuji Shimizu, Yang-Fang Li, Julia L Zimmermann, Wilhelm Stolz, Jürgen Schlegel, Gregor E Morfill, and Hans-Ulrich Schmidt. Cold atmospheric air plasma sterilization against spores and other microorganisms of clinical interest. *Applied and environmental microbiology*, 78(15):5077–5082, 2012.

[61] L. E. Kline. Electron and chemical kinetics in the low-pressure rf discharge etching of silicon in sf6. *IEEE Transactions on Plasma Science*, 14(2):145–155, 1986.

[62] P. O. Kochkin, C. V. Nguyen, A. P.J. Van Deursen, and U. Ebert. Experimental study of hard x-rays emitted from metre-scale positive discharges in air. *Journal of Physics D: Applied Physics*, 45(42), 10 2012.

[63] Atsushi Komuro and Ryo Ono. Two-dimensional simulation of fast gas heating in an atmospheric pressure streamer discharge and humidity effects. *Journal of Physics D: Applied Physics*, 47(15):155202, March 2014.

[64] I Korolov, M Vass, and Z Donkó. Scanning drift tube measurements of electron transport parameters in different gases: argon, synthetic air, methane and deuterium. *Journal of Physics D: Applied Physics*, 49(41):415203, September 2016.

[65] I A Kossyi, A Yu Kostinsky, A A Matveyev, and V P Silakov. Kinetic scheme of the non-equilibrium discharge in nitrogen-oxygen mixtures. *Plasma Sources Science and Technology*, 1(3):207–220, aug 1992.

[66] T. Kovács, W. Feng, A. Totterdill, J. M. C. Plane, S. Dhomse, J. C. Gómez-Martín, G. P. Stiller, F. J. Haenel, C. Smith, P. M. Forster, R. R. García, D. R. Marsh, and M. P. Chipperfield. Determination of the atmospheric lifetime and global warming potential of sulfur hexafluoride using a three-dimensional model. *Atmospheric Chemistry and Physics*, 17(2):883–898, 2017.

[67] A Kulikovsky. Positive streamer in a weak field in air: A moving avalanche-to-streamer transition. *Phys. Rev. E*, 57(6):7066–7074, 1998.

[68] A. A. Kulikovsky. Analytical Model of Positive Streamer in Weak Field in Air: Application to Plasma Chemical Calculations. *Physical Review E*, 57(6):7066–7074, 6 1998.

[69] E E Kunhardt, J Wu, and B Penetrante. Nonequilibrium macroscopic descriptions of electrons in weakly ionized gases. *Phys. Rev. A*, 37:1654–1662, March 1988.

[70] Mounir Laroussi. From killing bacteria to destroying cancer cells: 20 years of plasma medicine. *Plasma Processes and Polymers*, 11(12):1138–1141, 2014.

[71] N.G. Lehtinen. Physics and Mathematics of Electric Streamers. *Izvestiya vysshikh uchebnykh zavedenii. Radiofizika*, 64(1):12–28, 2021.

[72] Sergey B Leonov, Igor V Adamovich, and Victor R Soloviev. Dynamics of near-surface electric discharges and mechanisms of their interaction with the airflow. *Plasma Sources Science and Technology*, 25(6):063001, 2016.

[73] Chao Li, W J M Brok, Ute Ebert, and J J A M van der Mullen. Deviations from the local field approximation in negative streamer heads. *Journal of Applied Physics*, 101(12):123305, 2007.

[74] Xiaoran Li, Siebe Dijcks, Sander Nijdam, Anbang Sun, Ute Ebert, and Jannis Teunissen. Comparing simulations and experiments of positive streamers in air: steps toward model validation. *Plasma Sources Science and Technology*, 30(9):095002, 9 2021.

[75] Xiaoran Li, Baohong Guo, Anbang Sun, Ute Ebert, and Jannis Teunissen. A computational study of steady and stagnating positive streamers in n2–o2 mixtures. *Plasma Sources Science and Technology*, 31(6):065011, July 2022.

[76] Ningyu Liu and Victor P. Pasko. Effects of photoionization on propagation and branching of positive and negative streamers in sprites. *J. Geophys. Res.*, 109(A4), 2004.

[77] Leonard B Loeb. Ionizing waves of potential gradient: Luminous pulses in electrical breakdown, with velocities a third that of light, have a common basis. Technical Report 3676, 1965.

[78] A. Luque and U. Ebert. Sprites in varying air density: Charge conservation, glowing negative trails and changing velocity. *Geophys. Res. Lett.*, 37(6), 2010.

[79] A. Luque and U. Ebert. Electron density fluctuations accelerate the branching of positive streamer discharges in air. *Phys. Rev. E*, 84:046411, October 2011.

[80] A Luque and U. Ebert. Density models for streamer discharges: Beyond cylindrical symmetry and homogeneous media. *Journal of Computational Physics*, 231(3):904–918, 2012.

[81] A Luque, M González, and FJ Gordillo-Vázquez. Streamer discharges as advancing imperfect conductors: Inhomogeneities in long ionized channels. *Plasma Sources Science and Technology*, 26(12):125006, 2017.

[82] A. Luque and F. J. Gordillo-Vázquez. Mesospheric electric breakdown and delayed sprite ignition caused by electron detachment. *Nature Geoscience*, 5(1):22 – 25, 2012.

[83] Alejandro Luque and Ute Ebert. Growing discharge trees with self-consistent charge transport: the collective dynamics of streamers. *New Journal of Physics*, 16(1):013039, 2014.

[84] Alejandro Luque, Ute Ebert, Carolynne Montijn, and Willem Hundsdorfer. Photoionization in negative streamers: Fast computations and two propagation modes. *Appl. Phys. Lett.*, 90(8):081501, 2007.

[85] S Mirpour, A Martinez, J Teunissen, U Ebert, and S Nijdam. Distribution of inception times in repetitive pulsed discharges in synthetic air. *Plasma Sources Science and Technology*, 29(11):115010, November 2020.

[86] Eric Moreau. Airflow control by non-thermal plasma actuators. *Journal of physics D: applied physics*, 40(3):605, 2007.

[87] R Morrow and J J Lowke. Streamer propagation in air. *Journal of Physics D: Applied Physics*, 30(4):614–627, 1997.

[88] J. Mühle, A. L. Ganesan, B. R. Miller, P. K. Salameh, C. M. Harth, B. R. Greally, M. Rigby, L. W. Porter, L. P. Steele, C. M. Trudinger, P. B. Krummel, S. O'Doherty, P. J. Fraser, P. G. Simmonds, R. G. Prinn, and R. F. Weiss. Perfluorocarbons in the global atmosphere: tetrafluoromethane, hexafluoroethane, and octafluoropropane. *Atmospheric Chemistry and Physics*, 10(11):5145–5164, 2010.

[89] Lee T. Murray. Lightning nox and impacts on air quality. *Current Pollution Reports*, 2(2):115 – 133, 2016.

[90] D. Shindell F.-M. Bréon W. Collins J. Fuglestvedt J. Huang D. Koch J.-F. Lamarque D. Lee B. Mendoza T. Nakajima A. Robock

G. Stephens T. Takemura Myhre, G. and H. Zhang. *Anthropogenic and Natural Radiative Forcing. In: Climate Change 2013: The Physical Science Basis. Contribution of Working Group I to the Fifth Assessment Report of the Intergovernmental Panel on Climate Change.* Cambridge University Press, 2013.

[91] G V Naidis. Effects of nonlocality on the dynamics of streamers in positive corona discharges. *Technical Physics Letters*, 23(6):493–494, 1997.

[92] G V Naidis. Positive and negative streamers in air: Velocity-diameter relation. *Phys. Rev. E*, 79(5), May 2009.

[93] George V. Naidis. Modelling of plasma chemical processes in pulsed corona discharges. *Journal of Physics D: Applied Physics*, 30(8):1214–1218, 1997.

[94] George V. Naidis. Efficiency of generation of chemically active species by pulsed corona discharges. *Plasma Sources Science and Technology*, 21(4):042001, 8 2012.

[95] Tohru Nakano, Hirotaka Toyoda Hirotaka Toyoda, and Hideo Sugai Hideo Sugai. Electron-impact dissociation of methane into ch3 and ch2 radicals ii. absolute cross sections. *Japanese Journal of Applied Physics*, 30(11R):2912, November 1991.

[96] S Nijdam, F M J H van de Wetering, R Blanc, E M van Veldhuizen, and U Ebert. Probing photo-ionization: experiments on positive streamers in pure gases and mixtures. *J. Phys. D: Appl. Phys.*, 43(14):145204, 2010.

[97] Sander Nijdam, Jannis Teunissen, and Ute Ebert. The physics of streamer discharge phenomena. *Plasma Sources Sci. Technol., in press*, 2020.

[98] Mojtaba Niknezhad, Olivier Chanrion, Joachim Holbøll, and Torsten Neubert. Underlying mechanism of the stagnation of positive streamers. *Plasma Sources Science and Technology*, 30(11):115014, 11 2021.

[99] United States Committee on Extension to the Standard Atmosphere. *U.S. Standard Atmosphere, 1976*. National Oceanic and Atmospheric Administration, 1976.

[100] Ryo Ono and Atsushi Komuro. Generation of the single-filament pulsed positive streamer discharge in atmospheric-pressure air and its comparison with two-dimensional simulation. *Journal of Physics D: Applied Physics*, 53(3):035202, November 2019.

[101] S Pancheshnyi. Role of electronegative gas admixtures in streamer start, propagation and branching phenomena. *Plasma Sources Sci. Technol.*, 14(4):645–653, 2005.

[102] S. Pancheshnyi. Photoionization produced by low-current discharges in O 2 , air, N 2 and CO 2. *Plasma Sources Science and Technology*, 24(1):015023, 12 2014.

[103] S Pancheshnyi, M Nudnova, and A Starikovskii. Development of a cathode-directed streamer discharge in air at different pressures: Experiment and comparison with direct numerical simulation. *Phys. Rev. E*, 71:016407, January 2005.

[104] S. Pancheshnyi, S. M. Starikovskaia, and Andrey Starikovskiy. Role of photoionization processes in propagation of cathode-directed streamer. *Journal of Physics D: Applied Physics*, 34(1):105–115, 1 2001.

[105] S V Pancheshnyi, S M Starikovskaia, and A Yu Starikovskii. Collisional deactivation of n2(c3u, v=0, 1, 2, 3) states by n2, o2, h2 and h2o molecules. *Chemical Physics*, 262(2):349–357, 2000.

[106] S V Pancheshnyi and A Yu Starikovskii. Stagnation dynamics of a cathode-directed streamer discharge in air. *Plasma Sources Science and Technology*, 13(3):B1–B5, July 2004.

[107] Sergey Pancheshnyi. Effective ionization rate in nitrogen–oxygen mixtures. *Journal of Physics D: Applied Physics*, 46(15):155201, March 2013.

[108] Sergey Pancheshnyi, Benjamin Eismann, Gerjan Hagelaar, and Leanne Pitchford. Zdplaskin: a new tool for plasmachemical simulations. *Bulletin of the American Physical Society*, 53, 2008.

[109] Victor P Pasko, Umran S Inan, and Timothy F Bell. Spatial structure of sprites. *Geophys. Res. Lett.*, 25(12):2123–2126, 1998.

[110] C Pavan, M Martinez-Sanchez, and C Guerra-Garcia. Investigations of positive streamers as quasi-steady structures using reduced order models. *Plasma Sources Science and Technology*, 29(9):095004, September 2020.

[111] Danyal Petersen, Matthew Bailey, John Hallett, and William H. Beasley. Laboratory investigation of positive streamer discharges from simulated ice hydrometeors. *Quarterly Journal of the Royal Meteorological Society*, 132(615):263–273, 2006.

[112] Z Lj Petrović, M Šuvakov, Ž Nikitović, S Dujko, O Šašić, J Jovanović, G Malović, and V Stojanović. Kinetic phenomena in charged particle transport in gases, swarm parameters and cross section data*. *Plasma Sources Science and Technology*, 16(1):S1, January 2007.

[113] A V Phelps and L C Pitchford. Anisotropic scattering of electrons by N and its effect on electron transport. *Phys. Rev. A*, 31(5):2932–2949, 1985.

[114] C T Phelps. Field-enhanced propagation of corona streamers. *Journal of Geophysical Research (1896-1977)*, 76(24):5799–5806, 1971.

[115] N. A. Popov. Kinetics of plasma-assisted combustion: Effect of non-equilibrium excitation on the ignition and oxidation of combustible mixtures. *Plasma Sources Science and Technology*, 25(4), 2016.

[116] R. G. Prinn, R. F. Weiss, J. Arduini, T. Arnold, H. L. DeWitt, P. J. Fraser, A. L. Ganesan, J. Gasore, C. M. Harth, O. Hermansen, J. Kim, P. B. Krummel, S. Li, Z. M. Loh, C. R. Lunder, M. Maione, A. J. Manning, B. R. Miller, B. Mitrevski, J. Mühle, S. O'Doherty, S. Park, S. Reimann, M. Rigby, T. Saito, P. K. Salameh, R. Schmidt, P. G. Simmonds, L. P. Steele, M. K. Vollmer, R. H. Wang, B. Yao,

Y. Yokouchi, D. Young, and L. Zhou. History of chemically and radiatively important atmospheric gases from the advanced global atmospheric gases experiment (agage). *Earth System Science Data*, 10(2):985–1018, 2018.

[117] Jianqi Qin and Victor P Pasko. On the propagation of streamers in electrical discharges. *Journal of Physics D: Applied Physics*, 47(43):435202, October 2014.

[118] Mohamed Rabie and Christian M. Franck. Assessment of eco-friendly gases for electrical insulation to replace the most potent industrial greenhouse gas sf6. *Environmental Science & Technology*, 52(2):369–380, 2018. PMID: 29236468.

[119] Yuri P Raizer and John E Allen. *Gas discharge physics*, volume 1. Springer, 1991.

[120] Jyoti Rajput, Lutz Lammich, and Lars H. Andersen. Measured lifetime of sf_6^-. *Phys. Rev. Lett.*, 100:153001, Apr 2008.

[121] Vladimir A. Rakov and Martin A. Uman. *Lightning: Physics and Effects*. Cambridge University Press, 2003.

[122] Eric A. Ray, Fred L. Moore, James W. Elkins, Karen H. Rosenlof, Johannes C. Laube, Thomas Röckmann, Daniel R. Marsh, and Arlyn E. Andrews. Quantification of the sf6 lifetime based on mesospheric loss measured in the stratospheric polar vortex. *Journal of Geophysical Research: Atmospheres*, 122(8):4626–4638, 2017.

[123] Thomas Reddmann, Roland Ruhnke, and Wolfgang Kouker. Three-dimensional model simulations of sf6 with mesospheric chemistry. *Journal of Geophysical Research: Atmospheres*, 106(D13):14525–14537, 2001.

[124] R Rejoub, D R Sieglaff, B G Lindsay, and R F Stebbings. Absolute partial cross sections for electron-impact ionization of SFsub6/subfrom threshold to 1000 eV. *Journal of Physics B: Atomic, Molecular and Optical Physics*, 34(7):1289–1297, mar 2001.

[125] Casper Rutjes, Ute Ebert, Stijn Buitink, Olaf Scholten, and Thi Ngoc Gia Trinh. Generation of seed electrons by extensive air showers, and the lightning inception problem including narrow bipolar events. *Journal of Geophysical Research: Atmospheres*, 124(13):7255–7269, 2019.

[126] Martin Seeger, Torsten Votteler, Jonas Ekeberg, Sergey Pancheshnyi, and Luis Sánchez. Streamer and leader breakdown in air at atmospheric pressure in strongly non-uniform fields in gaps less than one metre. *IEEE Transactions on Dielectrics and Electrical Insulation*, 25(6):2147–2156, 2018.

[127] Goran B Sretenović, Ivan B Krstić, Vesna V Kovačević, Bratislav M Obradović, and Milorad M Kuraica. The isolated head model of the plasma bullet/streamer propagation: electric field-velocity relation. *Journal of Physics D: Applied Physics*, 47(35):355201, August 2014.

[128] S M Starikovskaia. Plasma-assisted ignition and combustion: nanosecond discharges and development of kinetic mechanisms. *J. Phys. D: Appl. Phys.*, 47(35):353001, 2014.

[129] Andrei Y Starikovskii, Nikolai B Anikin, Ilya N Kosarev, Eugeny I Mintoussov, Maria M Nudnova, Aleksandr E Rakitin, Dmitry V Roupassov, Svetlana M Starikovskaia, and Victor P Zhukov. Nanosecond-Pulsed Discharges for Plasma-Assisted Combustion and Aerodynamics. *Journal of Propulsion and Power*, 24(6):1182–1197, 2008.

[130] A Yu Starikovskiy and N L Aleksandrov. How pulse polarity and photoionization control streamer discharge development in long air gaps. *Plasma Sources Science and Technology*, 29(7):075004, July 2020.

[131] A Yu Starikovskiy, N L Aleksandrov, and M N Shneider. Simulation of decelerating streamers in inhomogeneous atmosphere with implications for runaway electron generation. *Journal of Applied Physics*, 129(6):063301, 2021.

[132] Andrey Starikovskiy, Edward Bazelyan, and Nick L Aleksandrov. The influence of humidity on positive streamer propagation in long air gap. *Plasma Sources Science and Technology*, 11 2022.

[133] C. Sterpka, J. Dwyer, N. Liu, B. M. Hare, O. Scholten, S. Buitink, S. ter Veen, and A. Nelles. The Spontaneous Nature of Lightning Initiation Revealed. *Geophysical Research Letters*, 48(23):2520–2533, 12 2021.

[134] H Tagashira, Y Sakai, and S Sakamoto. The development of electron avalanches in argon at high e/n values. ii. boltzmann equation analysis. *Journal of Physics D: Applied Physics*, 10(7):1051, May 1977.

[135] Jannis Teunissen. Improvements for drift-diffusion plasma fluid models with explicit time integration. *Plasma Sources Science and Technology*, 29(1):015010, Jan 2020.

[136] Jannis Teunissen and Ute Ebert. Simulating streamer discharges in 3d with the parallel adaptive Afivo framework. *Journal of Physics D: Applied Physics*, 50(47):474001, 2017.

[137] Jannis Teunissen and Ute Ebert. Afivo: A framework for quadtree/octree amr with shared-memory parallelization and geometric multigrid methods. *Computer Physics Communications*, 233:156–166, Dec 2018.

[138] Fumiyoshi Tochikubo and Hideyuki Arai. Numerical simulation of streamer propagation and radical reactions in positive corona discharge in n2/NO and n2/o2/NO. *Japanese Journal of Applied Physics*, 41(Part 1, No. 2A):844–852, February 2002.

[139] Anna Totterdill, Tamás Kovács, Juan Carlos Gómez Martín, Wuhu Feng, and John M. C. Plane. Mesospheric removal of very long-lived greenhouse gases sf6 and cfc-115 by metal reactions, lyman- photolysis, and electron attachment. *The Journal of Physical Chemistry A*, 119(10):2016–2025, 2015. PMID: 25647411.

[140] E M van Veldhuizen. *Electrical Discharges for Environmental Purposes: Fundamentals and Applications.* Nova Science Publishers, New York, 2000.

[141] E M van Veldhuizen and W R Rutgers. Pulsed positive corona streamer propagation and branching. *Journal of Physics D: Applied Physics*, 35(17):2169–2179, August 2002.

[142] E M van Veldhuizen and W R Rutgers. Inception behaviour of pulsed positive corona in several gases. *J. Phys. D: Appl. Phys.*, 36(21):2692–2696, 2003.

[143] P A Vitello, B M Penetrante, and J N Bardsley. Simulation of negative-streamer dynamics in nitrogen. *Physical Review E*, 49(6):5574–5598, 1994.

[144] T. Von Clarmann. Chlorine in the stratosphere. *Atmósfera*, 26(3):415–458, 2013.

[145] Th von Woedtke, S Reuter, K Masur, and K-D Weltmann. Plasmas for medicine. *Physics Reports*, 530(4):291–320, 2013. Plasmas for Medicine.

[146] Zhen Wang, Siebe Dijcks, Yihao Guo, Martijn van der Leegte, Anbang Sun, Ute Ebert, Sander Nijdam, and Jannis Teunissen. Quantitative prediction of streamer discharge branching in air, 2022.

[147] Zhen Wang, Anbang Sun, and Jannis Teunissen. A comparison of particle and fluid models for positive streamer discharges in air. *Plasma Sources Science and Technology*, 31(1):015012, January 2022.

[148] Won J Yi and P F Williams. Experimental study of streamers in pure n2 and n2/o2 mixtures and a 13 cm gap. *J. Phys. D: Appl. Phys.*, 35(3):205–218, 2002.

[149] M B Zheleznyak, A K Mnatsakanian, and S V Sizykh. Photoionization of nitrogen and oxygen mixtures by radiation from a gas discharge. *Teplofizika Vysokikh Temperatur*, 20:423–428, 1982.

[150] Marcin Ziółkowski, Anna Vikár, Maricris Lodriguito Mayes, Ákos Bencsura, György Lendvay, and George C. Schatz. Modeling the electron-impact dissociation of methane. *The Journal of Chemical Physics*, 137(22):22A510, 2012.

Acknowledgements

First, I thank Ute Ebert, Jannis Teunissen, and Behnaz Bagheri - who interviewed and offered me this position - for their guidance in this undertaking.

I want to acknowledge the people in the Multiscale Dynamics group: Andy Martinez, Rakesh Sarma, Mandar Chandorkar, Carl Schneider, Bastiaan Braams, Dennis Bouwman, Hemaditya Malla, Xiaoran Li, Zhen Wang, Alejandro Malagon, and Dung Nguyen. Thank you for your quips and company.

I also want to acknowledge people I've met in CWI: Nada Mitrovic, Duda Tepsic, Beatriz Salvador, Shane Gibbons, Syver Agdestein, Ruochen Guo, Francien Bossema, Nikolaj Mücke, Erik Baquedano, Vera Sarkol, Bikkie Aldeias, Martine Anholt Gunzeln, Karima El Bacha, Minnie Middelberg, Léon Ouwerkerk, Remco Westra, and Irma van Lunenburg. You have helped me in various ways and for that I thank you.

Thank you to the members of the SAINT network and people from TU/e: Matthias Heumesser, Christoph Köhn, Sander Nijdam, Ravi Patel, and Anita Peeters. I am grateful for your camaraderie and assistance.

From outside work, I thank Divya Bohra, Peter Sweers, Karin van der Zwan, Semiha Kaya, Monique Uidam, Jo Emmett, and Mark-Pieter van den Heuvel for their kindness and support.

Finally I thank my mother, Teresita Francisco, for her unrelenting concern. I am deeply indebted to old friends Angela Leron, Denz Del Villar, Jojee Dumayaca, Aaron Corpuz, Megan Matias, Alou Wy, Marinella Wy, and Louise Dulay for their encouragement and humour. Thank you.

To the people I've forgotten to include, I apologize. Thank you all regardless.

Curriculum Vitae

Hani Francisco is a scientist. He received his bachelor's degree in physics in 2014 and his bachelor's degree in materials science and engineering in 2015 from the Ateneo de Manila University in the Philippines. He worked outside academia for two years before pursuing a master's degree in the physics of complex systems at the Univesitat de les Illes Balears in Spain. In 2018, he obtained his master's degree and began a PhD project on computational models for lightning physics at the Centrum voor Wiskunde & Informatica in the Netherlands. This thesis is the culmination of that project.

List of publications

1. Hani Francisco, Behnaz Bagheri, and Ute Ebert. Electrically isolated propagating streamer heads formed by strong electron attachment. *Plasma Sources Science and Technology*, 30(2):025006, February 2021
2. Hani Francisco, Jannis Teunissen, Behnaz Bagheri, and Ute Ebert. Simulations of positive streamers in air in different electric fields: steady motion of solitary streamer heads and the stability field. *Plasma Sources Science and Technology*, 30(11):115007, November 2021
3. Dennis Bouwman, Hani Francisco, and Ute Ebert. Estimating the properties of single positive air streamers from measurable parameters. arXiv:2305.00842 [physics.plasm-ph], May 2023 [epub ahead of publishing]
4. Hani Francisco, Ute Ebert, John Plane, and Martin Füllekrug. SF_6 destruction by atmospheric streamer discharges. [in preparation]